Coexistent Oxide p-n Junctions

DFT Analysis of Interfaces Between Nickel Oxide and Zinc Oxide

Emil Herman Frøen

Master Thesis in Material Chemistry

UNIVERSITY OF OSLO

31 – 05 – 2019

Preface

This master thesis represents a part of a master's degree in material chemistry at the University of Oslo. The work was performed in the period August 2017 to May 2019.

I wish to thank my supervisors, Professor Truls E. Norby, Researcher Tor S. Bjørheim and Professor II Ole M. Løvvik for their assistance through the course of this work.

This thesis is written using the text editor Microsoft Word 2016.

University of Oslo, May 2019

Emil Herman Frøen

Summary

NiO and ZnO are a pair of p- and n-type wide band gap metal oxide semiconductors that forms a partially soluble system with each other. Due to these properties, they are considered a potential semiconductor pair for the construction of a p-n heterojunction that remains thermodynamically stable under high-temperature applications. To this end, an in-depth understanding of the properties of the available interface arrangements, as well as of the effects of the formation of the mixed phases on the properties of the semiconductors is necessary. This study seeks to investigate these aspects by a theoretical approach, utilizing DFT to model the properties of the possible interfaces, as well as the behavior of the mixed phase systems at different concentrations of solute ions.

The bulk properties of nickel substituted ZnO (Ni:ZnO) and zinc substituted NiO (Zn:NiO) were investigated utilizing a hybrid functional approach. Both systems were found to exhibit an increase in the VBM energy level relative to the pure materials, with maxima of 0.39 eV and 0.26 eV, respectively. The VBM change with solute ion concentrations has been found to reach saturation at 3.70% and 4.69%, again respectively. The VBM shifts of Ni:ZnO and Zn:NiO are found to be caused by the formation of a new valence band due to localized impurity states, and the formation of cubic ZnO bonding states, respectively. For both mixed phase materials, a reduction of the band gap width is observed: The Ni:ZnO band gap is reduced by 0.3 eV, while the Zn:NiO band gap changes linearly with concentration throughout the experimental concentration range, with a band gap reduction of 0.8 eV at 31.25% zinc concentration.

The structural, energetic and electronic properties of the NiO-ZnO interfaces formed from pairs of low-Miller index surfaces were investigated utilizing a GGA+U functional approach. The polar-polar interfaces were found to exhibit the most favorable interface formation energies, for either strain distribution considered. The natural band offsets were found to all form a type II heterojunction with valence band offset values ranging from 0.73 to 1.84 eV. The majority of the

considered interface arrangements exhibit considerable interface states: Conduction band interface states are the most prevalent, formed from nickel 3d-orbitals. The results indicate that the prevalence of these interface states, and the general NiO-ZnO heterojunction properties, may be manipulated to a considerable extent by choosing a suitable interface, and the growth conditions under which it is formed.

Contents

Preface ... i

Summary ... ii

1. Introduction ... 1

 1.1. p-n Junction ... 1

 1.2. Thermodynamically Stable p-n Junctions ... 2

 1.3. NiO – ZnO p-n Junctions ... 2

 1.4. Goals and Methodologies ... 3

2. Theory ... 4

 2.1. Crystalline Material Modelling ... 5

  2.1.1. Periodic Boundary Conditions ... 5

  2.1.2. Reciprocal Cell and the First Brillouin Zone ... 6

 2.2. Quantum Mechanical Calculations ... 6

  2.2.1. Wavefunction-Based Methods ... 6

  2.2.2. Density Functional Theory ... 8

  2.2.3. Post-DFT Methods ... 13

 2.3. Defect Chemistry ... 15

  2.3.1. Kröger-Vink Notation ... 15

  2.3.2. Intrinsic Defects in NiO and ZnO ... 16

 2.4. p-n Junctions ... 19

  2.4.1. Fermi Levels of Approximate and Practical Semiconductors ... 24

  2.4.2. Heterojunctions, and How They Differ ... 27

 2.5. Diodes and Transport Properties ... 30

 2.6. Wulff Construction ... 32

3. Methodology 34
3.1. Implementation 34
3.1.1. Planewave Basis Set 34
3.1.2. Pseudopotentials 35
3.1.3. Supercell Approach 36
3.1.4. Surfaces 37
3.2. Calculations 37
3.2.1. Surface Energy Calculation 37
3.2.2. Band Alignment 38
3.2.3. Mixed Phase Band Edge Level 41
3.2.4. Charge Carrier Transport 42
3.2.5. Interface Energy Calculation 43
3.2.6. Spatially Resolved DOS 43
3.2.7. Induced Interface Electron Density 45
3.2.8. Bader Analysis 45
3.3. Calculation Settings, Convergence and Calculation Procedures 46
3.3.1. Bulk and Interface Settings 46
4. Review of Relevant Literature 53
4.1. Nickel Oxide 53
4.2. Zinc Oxide 58
4.3. Nickel Oxide – Zinc Oxide Mixed Phase System 63
4.4. Properties of the Li:NiO-Al:ZnO p-n Junction 67
5. Results and Discussion 70
5.1. Bulk Parameters 70

5.1.1. Bulk NiO 70
5.1.2. Bulk ZnO 74
5.2. NiO-ZnO Mixed Phase 78
5.2.1. Nickel Dissolved in ZnO (Ni:ZnO) 78
5.2.2. Zinc Dissolved in NiO (Zn:NiO) 83
5.3. Surface Calculations 87
5.3.1. NiO Surfaces 87
5.3.2. ZnO Surfaces 98
5.4. NiO-ZnO Heterojunction Interfaces 107
5.4.1. Interface Optimizations 108
5.4.2. Relaxed Structure Interfaces 110
5.4.3. Static Structure Interfaces 130
6. General Discussion 136
6.1. Mixed Phase System 136
6.2. Heterojunction Interfaces 138
6.3. Practical Considerations 140
6.3.1. p-n Junctions 140
6.3.2. Nanocomposites 141
6.4. Further Work 143
7. Conclusion 144
8. References 145
9. Appendix 156

1.Introduction

1.1. p-n Junction

The formation of a p-n junction is a consequence of two different types of semiconductors, with holes and electrons as the dominant charge carriers respectively, forming a single system. The differing characteristics of the component semiconductors cause the free charge carriers of each side to flow towards the junction and combine, annihilating the charge carriers. Once equilibrium has been achieved, the charge carrier concentrations in the regions immediately adjacent the junction is greatly depleted, decreasing the electrical conductivity in this region by orders of magnitude. Upon the application of an external electrical potential, the charge carriers outside the depletion region will shift in response, resulting in the depletion region either being flooded with charge carriers, or further depleted depending on the direction of this applied potential. The selectivity of the response to the applied potential causes the electrical resistance across the junction to sharply change with the direction of the potential, only allowing electricity to flow in a single direction: The p-n junction rectifies flow of electrical current.

These properties make p-n junctions a fundamental component of all modern electronics, both as a component, as in diodes, or as a building block for more complicated semiconductor components such as transistors, which include two or more p-n junctions. Depending on the exact construction of the junction, it may have extra properties such as light emission, utilized in applications such as LEDs and laser construction, or conversely light absorption, commonly employed for electrical generation by solar panels, or several other possibilities.

1.2. Thermodynamically Stable p-n Junctions

Conventional modern p-n junctions are predominantly homojunctions constructed from doped silicon semiconductors. While these junctions have a wide range of usages and applications, they all have an inherent shortcoming to them: The p- and n-type semiconductors must be doped with acceptors and donors, respectively. This forms a low-entropy system where different ions occupy separate regions of the same system and is consequently thermodynamically unstable. Over time, the dopant ions will interdiffuse across the junction, blurring it as the different dopant species counteract each other's effect. Eventually, the interdiffusion will proceed to the extent where the junction breaks down all together and loses its intended properties. This problem has no permanent solution, apart from slowing the decay by maintaining the junction at a low temperature, kinetically hindering the diffusion process. Silicon based semiconductors are thus unsuitable for high-temperature applications such as thermoelectric generation.

A possible solution to this issue is the utilization of coexistent oxide p-n junctions. The basic idea is to utilize a pair of metal oxide semiconductors that form a partially soluble system. A p-n heterojunction formed in such a manner would exhibit an initial period of interdiffusion, until thermodynamic equilibrium concentration for the intended operational temperature is achieved. At this point the p-n junction would experience no sum interdiffusion and could theoretically remain stable and functional indefinitely.

1.3. NiO – ZnO p-n Junctions

A potential pair of semiconductors for such applications, is the NiO – ZnO pair, as p- and n-type semiconductors, respectively. Both materials are wide band gap semiconductors, with band gaps of 3.37 eV[1] for ZnO and a range of 3.6-4.3 eV[2–5] for NiO, which absorb light in the ultraviolet spectrum, and allow visible light to pass through. Consequently, there is great interest in the system for potential usages such as for the construction of transparent transistors for usage in see-through electronics.

A NiO – ZnO heterojunction system is an example of an interface where the component semiconductors naturally assume two dissimilar crystal structures. NiO crystallizes in a rock-salt structure, while ZnO will commonly adopt a wurtzite structure. The latter may also adopt a cubic structure, but this occurs only under specific growth conditions. Due to this difference, NiO and ZnO form different surface termination structures, and by extension, may form several interfaces with different surface combinations. Distinct such interfaces may exhibit considerably different properties.

1.4. Goals and Methodologies

NiO and ZnO are materials that have separately received considerable attention in recent years for their properties as transparent semiconductor materials. While the specific system of NiO – ZnO p-n junctions has been investigated to some extent,[4,6–8] no extensive investigation of the various possible surfaces and interfaces has been performed. This is important, as understanding the structural and electronic properties of the heterojunctions is necessary for the construction of functional devices.

This project aims to investigate the effects of mixing nickel ions into the ZnO structure, and vice versa, on the properties of these bulk materials. Further, the aim is to investigate the structural and electronic properties of the possible interface arrangements of the NiO – ZnO system, and to explore the individual differences between these. Specifically, the energetic favorability of each interfaces' formation, the presence of interface states, and the band offsets are explored. Finally, the implications of these properties on practical p-n junctions and nanocomposites is considered.

Density Functional Theory calculations will be utilized, primarily at the GGA+U level of theory, to simulate the NiO – ZnO interface junctions and calculate the electronic structure of these. The effect of the mixed phases on the electronic structures are investigated utilizing hybrid functional.

2.Theory

Gathering of experimental evidence has always been a core part of science, complemented by theories to explain or interpret the observed results. Certain systems and properties are, however, either difficult or impossible to explore in an experimental environment. This shortcoming is the reason why in recent years, utilizing computational methods based solely on theoretical principles, so-called *ab initio* methods, have become an increasingly big part of the scientific discipline. Computational modelling is now considered a widely accepted methodology for exploring the properties, especially structural and electronic, of various systems, and is now used in a wide range of fields, such as material sciences, catalysis, general chemistry and numerous more. They may be used in conjunction with experimental evidence to explain observations, or to make predictions on properties new materials that have yet to be made.

Computational modeling has a number of advantages over experimental methods. As previously noted, certain systems are too difficult, expensive or dangerous to perform practical experiments with. Computational methods thus offer a safe, cheap and relatively simple alternative approach to study these cases. A certain drawback of these methods is the fact that performing calculations may be a bit too easy and may very well be wielded as a complete black box methodology, with no knowledge of its actual workings. Consequently, there is a risk of committing errors, and having no idea they exist in your data. Understanding the principles of computational methods is thus just as important as for any other branch of science.

The two basic approaches for quantum chemical modelling are wavefunction based methods such as Hartree-Fock and Post-Hartree-Fock methods, and Density Functional Theory.

2.1. Crystalline Material Modelling

2.1.1. Periodic Boundary Conditions

Bulk crystalline materials, or any non-amorphous material in general, are comprised of repeating pattern(s) that are, from an atomic scale viewpoint, effectively infinitely repeating in all directions. Computers cannot handle the simulation of an effectively infinite number of atoms, however, so instead periodic boundary conditions are utilized.

The repeating atomic pattern of the material in question is defined by a single unit cell. This unit cell is infinitely replicated in three dimensions by translational images of the original unit cell, see Figure 2-1. These images interact with the unit cell by potential interaction, and particle exchange. In effect, any atom that moves out of the unit cell on one side, is reintroduced into the box from the opposite side.

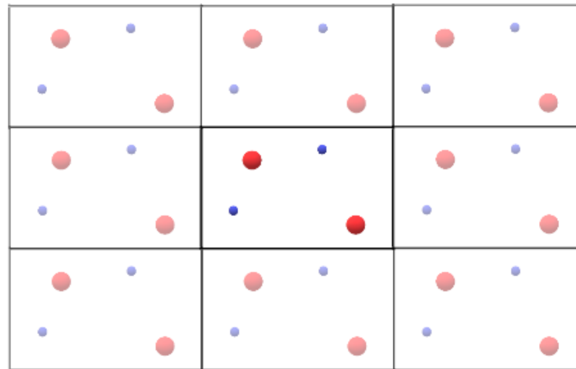

Figure 2-1 Periodic boundary conditions, represented in 2D. The opaque image in the center represents the unit cell, the transparent copies are the translational images.

The validity of this method for use within a plane wave basis calculation is tied to the Bloch theorem, with its consequences explained in section 3.1.1.

Within periodic boundary conditions, systems that are non-periodic along one or more axes, such as surfaces of a material, may still be treated. The non-periodicity is introduced in the form of including a vacuum layer within the unit cell, as demonstrated in Figure 2-2. This vacuum layer must be sufficiently wide such that the interactions between the atoms in separate images along

the non-periodic axis are negligible. This requirement causes difficulties for systems with sum electronic charge, or significant dipole moment.

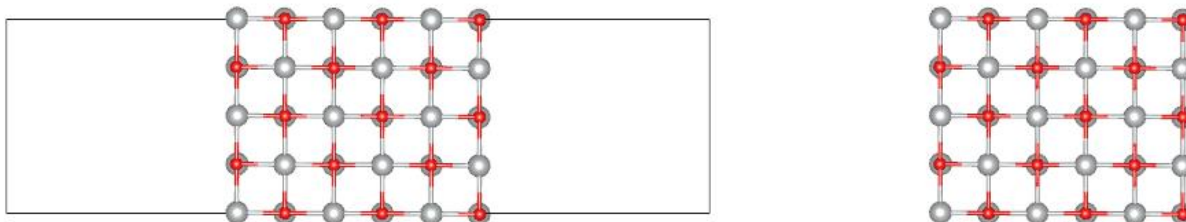

Figure 2-2 Representation of surfaces under periodic boundary conditions. The black rectangle represents the calculation cell, the structure to the right is the image.

2.1.2. Reciprocal Cell and the First Brillouin Zone

As an expansion of the unit cell, another important description of a crystalline system for computational purposes, is the reciprocal lattice. This lattice is the Fourier transform of the Bravais lattice, described by vectors b defined by the unit cell vectors a of the latter:

$$\boldsymbol{b}_1 = 2\pi\frac{\boldsymbol{a}_2 \times \boldsymbol{a}_3}{L^3} \qquad \boldsymbol{b}_2 = 2\pi\frac{\boldsymbol{a}_1 \times \boldsymbol{a}_3}{L^3} \qquad \boldsymbol{b}_3 = 2\pi\frac{\boldsymbol{a}_1 \times \boldsymbol{a}_2}{L^3} \qquad \text{2-1}$$

The equivalent of the unit cell in reciprocal space is called the first Brillouin zone. The Brillouin zone is of central importance for computational chemistry, as it is the region of an infinitely repeating system the properties of which is directly sampled. This point is elaborated further in section 3.1.1.

2.2. Quantum Mechanical Calculations

2.2.1. Wavefunction-Based Methods

The electronic and chemical properties of a given atomic system may be described by its wave function. Hence, solving the time-independent, non-relativistic Schrödinger equation for a many-body system is fruitful for understanding materials on an atomic scale:

$$\hat{H}\Psi = E\Psi \qquad 2\text{-}2$$

Here, $\hat{H}$ represents the Hamiltonian operator, E the total energy of the system, and ψ is the total wavefunction of the system. The total Hamiltonian of the system may be broken down into individual components as follows:

$$\hat{H} = T_n + T_e + V_{ne} + V_{ee} + V_{nn} \qquad 2\text{-}3$$

These terms correspond to kinetic energy of nuclei and electrons (T_n and T_e), and potential energy of nuclei-electron, electron-electron and nuclei-nuclei (V_{ne}, V_{ee}, and V_{nn}) interactions, respectively.

Once the wavefunction is known, solving the Schrödinger equation is relatively simple. The problematic part of this equation is deriving the wave function itself. The exact analytical solution is only known for the simplest systems, such as single-particle systems in static potential fields. In physical atomic and molecular systems, there are a large number of mutually interacting electrons and nuclei, so the form of the wavefunction must be derived by numerical methods, which rapidly becomes unfeasibly time- and resource demanding with growing system size. This difficulty is known as the many-body problem.

Due to the complexity of obtaining a near-exact wavefunction by numerical means, a number of approximations are commonly used in practical quantum mechanical calculation methods. Among these, the Born-Oppenheimer is practically ubiquitous in quantum mechanical calculations. The approximation assumes the wavefunction of an atomic (molecular) system may be broken into separate nuclear and electronic components.[1] Further, due to the large difference in mass between the nuclei and the electrons, the kinetic energy of the nuclei may, for a system where the atoms are stationary, be neglected as well.[2] The total energy of the system may thus be expressed in terms of the electronic Schrödinger equation

[1] The approximation also assumes that the nuclear motion is sufficiently slow relative to electronic motion that nuclei may be considered effectively fixed.

[2] The Born-Oppenheimer approximation commonly also includes certain other approximations, such as the adiabatic approximation and neglecting the diagonal correction terms. The nucleus-nucleus potential energy calculates to a constant, and cancels out on both sides of the equation.

$$\widehat{H}_e\psi(r;R) = E_e(R)\psi(r;R) \tag{2-4}$$

where $\widehat{H}_e$ is the electronic Hamiltonian:

$$\widehat{H}_e = T_e + V_{ne} + V_{ee} \tag{2-5}$$

$E_e(R)$ is the electronic energy and $\psi(r;R)$ is the electronic wavefunction. The notation means the wavefunction depends explicitly on the position r, and parametrically on the constant nuclei positions R. Intuitively, the Born-Oppenheimer approximation models an atomic (molecular) system with the nuclei as charged classical particles, that move on a potential energy surface $E_e(R)$. Consequently, apart from special cases where the wavefunction of the nuclei is also of interest, only the solution to the electronic Schrödinger equation is necessary for common quantum chemical calculations.

In recent years, an alternate approach from wavefunction-based methodologies of calculating the electronic Schrödinger equation has gained considerable popularity due to striking a good balance between accuracy of results with more favorable scaling of computational demands with system size, and is now one of the dominant methodologies for electronic structure calculations: Density Functional Theory (DFT) methods.

2.2.2. Density Functional Theory

The basic idea of DFT is that the energy of an electronic system may be written in terms of the electron probability density ρ. The electronic energy E, which represents the total energy of the electrons within the system, is considered as a functional of the electron density, henceforth denoted $E[\rho]$. The proof of the validity of the DFT methodology lies in two theorems, known as the Hohenberg-Kohn theorems[9], which apply to any system of electrons moving in an external potential (such as the potential from the nuclei of atoms). The theorems state that:

Theorem I: *The external potential, and hence the total energy, is a unique functional of the electron density.*

Corollary: *The ground-state density uniquely determines the potential, and thus all ground-state electronic properties.*

Theorem II: *For a trial ground-state electron density ρ'(**r**) and a true ground-state electron density ρ(**r**), then E[ρ'] ≥ E[ρ], equal if only if ρ'(**r**)= ρ(**r**).*

Together, these theorems serve not just to validate the methodology, but also the applicability of a variational approach to finding the electron probability density. Specifically, these theorems allow the ground state energy of a system to be written as:

$$E[\rho] = T[\rho] + V_{ee}[\rho] + \int \rho(r)v(r)dr \qquad 2\text{-}6$$

where $T[\rho]$, $V_{ee}[\rho]$ and $\int \rho(r)v(r)dr$ are the kinetic energy, electron-electron interaction energy and electron-external potential interaction contributions, respectively. The $V_{ee}[\rho]$ contribution may be separated into a classical Coulombic contribution $J[\rho]$, and a quantum mechanical contribution.

DFT, in its basic formulation, has many advantages over conventional wavefunction based methods. The arguably most important property for treating large systems with a quantum mechanical approach, is that the approach uses a single three-dimensional function to determine the state of a N_e-electron system. To model the same system with a wavefunction approach requires a (minimum) $3N_e$-dimensional function with constraints to ensure it is fully antisymmetric.

DFT utilizing only a three-dimensional function to describe the system is referred to as orbital-free DFT and could be considered as an ideal case. In practical terms, however, the accuracy of orbital-free DFT is presently low, largely due to the lack of an accurate method of determining the kinetic energy of electrons, from only the electronic probability density. Hence orbital-free DFT is only an alternative for very large systems where no other alternative is practically feasible. The method employed to remedy this issue, and the reason behind the success of modern DFT, is the Kohn-Sham DFT model.

Kohn-Sham Density Functional Theory

The idea behind the Kohn-Sham model is to utilize the fact that the operator for calculating kinetic energy of electrons from a wave function is known. The kinetic energy is therefore calculated from an auxiliary set of orbitals, which are used to represent the electron probability density $\rho(r)$, commonly referred to as Kohn-Sham orbitals.

The Kohn-Sham method considers a reference system of N_e non-interacting electrons moving in an external potential $v_{ref}(r)$. This external potential is selected such that the reference electron probability density $\rho_{ref}(r)$ is identical to the true electron density $\rho(r)$. For this reference system, the total Hamiltonian is defined as the sum of all one-electron Kohn-Sham Hamiltonians:

$$h_{ref} = \sum_{i=1}^{N_e} h_i^{KS} \qquad h_i^{KS} = -\frac{\hbar^2}{2m_e}\nabla_i^2 + v_{ref}(r) \tag{2-7}$$

where $\hbar$ is the reduced Planck constant, m_e is the electron mass, and ∇_i^2 is the Laplacian of electron i. The Kohn-Sham Hamiltonians have corresponding one-electron Kohn-Sham orbitals:

$$h_i^{KS}\psi_m^{KS} = \varepsilon_m^{KS}\psi_m^{KS} \tag{2-8}$$

The total energy functional for the true system may be written in terms of the reference system functional, plus a correction term to account for the difference between interacting and non-interacting electrons:

$$E[\rho] = T_{ref}[\rho_{ref}] + J_{ref}[\rho_{ref}] + \int \rho(r)v(r)dr + \{T[\rho] + V_{ee}[\rho] - (T_{ref}[\rho_{ref}] + J_{ref}[\rho_{ref}])\} \tag{2-9}$$

The correction term is the exchange-correlation energy. This final equation for the total energy is alternatively written as:

$$E[\rho] = T_{ref}[\rho] + J[\rho] + \int \rho(r)v(r)dr + E_{XC}[\rho] \tag{2-10}$$

This equation, under the constraint that the total electron probability density must remain constant under variation, gives the final Kohn-Sham equation, which gives the electronic energy of any given wavefunction:

$$\left\{h_e + \frac{e^2}{4\pi\varepsilon_0}\int \frac{\rho(r_2)}{|r_1 - r_2|}dr_2 + v_{XC}(r_1)\right\}\psi_m^{KS}(r_1) = \varepsilon_m^{KS}\psi_m^{KS} \qquad 2\text{-}11$$

where e is the fundamental charge, ε_0 is the vacuum permittivity, $v_{XC}(r_1)$ is the exchange-correlation potential, and h_e is the one-electron Hamiltonian:

$$v_{XC}(r) = \frac{\delta E_{XC}[\rho]}{\delta\rho(r)} \qquad h_e = -\frac{\hbar^2}{2m_e}\nabla_i^2 + v(r) \qquad 2\text{-}12$$

The Kohn-Sham equation must be solved to find the electron probability density that minimizes the energy functional, which is done typically by an iterative scheme designed to extract the lowest energy solutions.

The greatest unsolved problem with DFT, is the exchange-correlation functional: its analytical form is not known. Hence, numerous approximate functionals have been proposed. Many of these functionals are, with varying degree, ad hoc corrections to the energy functionals. DFT thus occupies a rather unique intermediate position between status both as *ab initio* and as a semiempirical method. In fact, the main source of error associated with the DFT methodology originates from the approximate nature of the exchange-correlation functional.

Commonly, the exchange-correlation functional is considered as a linear combination of separate exchange and correlation functionals,

$$E_{XC}^{LDA}[\rho] = E_X[\rho] + E_C[\rho] \qquad 2\text{-}13$$

with each part derived separately.

The most basic form of exchange-correlation functionals, are the Local Density Approximation (LDA) functionals, and their spin polarized equivalents, Local Spin Density Approximation (LSDA) functionals.[10]

The general form of these functionals is written as:

$$E_{XC}^{LDA}[\rho] = \int \rho(r)\epsilon_{xc}(\rho)dr \qquad 2\text{-}14$$

Or, with spin correlation included,

$$E_{XC}^{LSDA}[\rho_\alpha, \rho_\beta] = \int \rho(r)\epsilon_{xc}(\rho_\alpha, \rho_\beta)dr \qquad 2\text{-}15$$

The ϵ_{xc} is the exchange-correlation energy of a homogenous electron gas.

A primitive example of an LDA functional is the Thomas-Fermi-Dirac functional, here simplified somewhat:

$$E_{XC}^{TFD}[\rho] = T[\rho] + V_{Ne}[\rho] + \frac{1}{2}\frac{\hbar^2}{m_e}\int \frac{\rho(r_1)\rho(r_2)}{|r_1 - r_2|}dr_1 dr_2$$

$$+C_{ex}\int \rho(r)^{\frac{4}{3}}\,dr \qquad 2\text{-}16$$

The two parts of the total energy functionals that are explicitly written out are the classical Coulomb interaction, and the exchange contribution, respectively. The form in which the latter is expressed is the reason for the name Local Density Approximation: It is originally a property that explicitly depends on the density at more than one position yet is expressed as a function of a single point density.

The methodology assumes the electron probability density may be considered as a uniform gas. Consequently, L(S)DA performs relatively decently on systems where this approximation is appropriate, such as in metals. Systems with highly localized electrons, (and consequently rapidly varying electron density) such as molecules or ionic species are typically badly described by L(S)DA functionals. The LDA class of functionals have a consistent tendency to predict overly strong bonding between atoms, which reflects in their tendency to underestimate bond lengths and lattice constants.

A first improvement over the classical LDA functionals are functionals that take into account the gradient of the electron probability density, the generalized-gradient approximation (GGA) functionals, with a general form:

$$E_{XC}^{GGA}[\rho] = \int \rho(r)\epsilon_{XC}^{GGA}[\rho(r), \nabla\rho(r)]dr \qquad 2\text{-}17$$

The inclusion of the electron probability density gradient in the functional allows for the functional to address divergences from homogenous electron distribution. Consequently, many

of the cases where LDA functionals fall short, may be considerably improved by utilizing GGA functionals. In particular, the description of strongly correlated systems, and systems with occupied d- and f- orbitals, which are highly localized.

GGA functionals generally improve most results compared to LDA functionals, but have a tendency to overestimate bond lengths, as opposed to LDA systematically underestimating them. Band gaps of semiconductors are also notoriously underestimated with GGA functionals. It is not uncommon for the shape of the band structure itself to be close to correct despite the band gap error.

2.2.3. Post-DFT Methods

Improving results beyond GGA functionals generally requires the use of relatively ad hoc post-DFT methodologies. A first improvement beyond GGA is typically utilizing GGA+U (or more generally, DFT+U).

In GGA+U, an extra Hubbard-like term is added to the potential of electrons in specified orbitals. There are two common variants of the "+U" formalism: The Liechtenstein[11] and the Dudarev[12] approaches. In this thesis, the Dudarev approach is used, which utilizes an effective U parameter:

$$U_{eff} = U - J \qquad 2\text{-}18$$

$$E_{DFT+U} = E_{DFT} + \sum_a \frac{U_{eff}}{2} Tr(\rho^a - \rho^a \rho^a) \qquad 2\text{-}19$$

Here, ρ^a is the band occupation matrix. The main difference between the two approaches is that the Dudarev approach ignores higher order Coulomb interactions and is therefore invariant to rotation.

The choice of U_{eff} (or U and J separately) may be done in several different ways, such as fitting to empirical data, or utilizing parameters commonly observed in literature. A more rigorous methodology, however, is to determine the parameter in a self-consistent manner based on a piecewise linearity model.[13] Utilizing an exact exchange correlation-functional, the total energy

of otherwise identical systems with differing fractional charges should exhibit linearity between integer charges, with discontinuities at the integer charges.[14] In standard LDA and GGA functional, the observed behaviors differ from this ideal, rather exhibiting convex curves, due to the self-interaction errors associated with these methodologies, as shown in Figure 2-3.

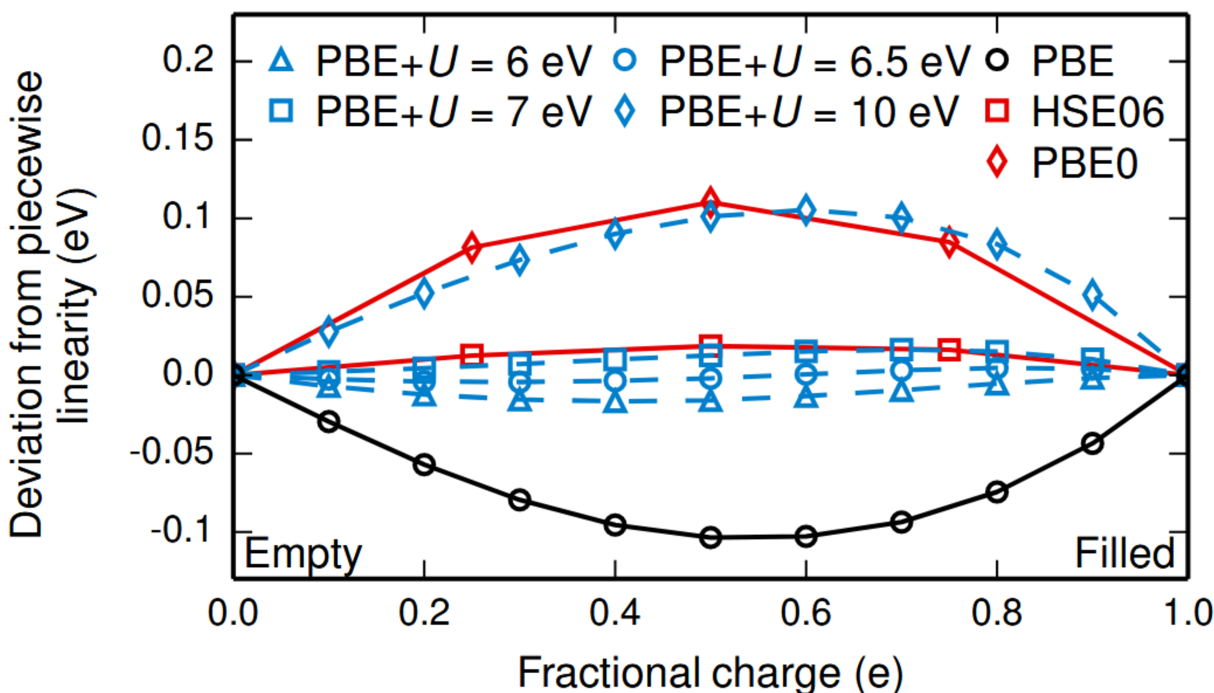

Figure 2-3 A figure describing the piecewise linearity model, and how various functionals and +U values diverge from the ideal behavior. Figure from reference [15].

There are a variety of GGA functionals available for use, among them the PBE functional[16], utilized in this project. It is one of the more common choices for calculations on materials.

A next step beyond GGA functionals are typically hybrid functionals. They take advantage of the ability of Hartree-Fock type calculations to obtain the exact exchange energy, and mix a fraction of this value, as a general standard 25%, with 75% of the density functional exchange energy. The correlation energy is typically entirely from the density functional. Hybrid functionals may be described by the general functional form:

$$E_{XC}^{Hyb}[\rho] = \alpha E_x^{HF} + (1-\alpha)E_x^{DFT}[\rho] + E_C^{DFT}[\rho] \qquad 2\text{-}20$$

The hybrid functional utilized in this project is a hybrid extension of the PBE functional, PBE0.[17] The general structure of the basic functional is the same as the previous equation, with a standard fraction of 25% exact exchange:

$$E_{XC}^{PBE0}[\rho] = 0.25E_{x}^{HF} + 0.75E_{x}^{PBE}[\rho] + E_{C}^{PBE}[\rho] \quad 2\text{-}21$$

2.3. Defect Chemistry

As previously mentioned in in section 2.1 above, a perfect crystalline material consists of a periodically repeating pattern of atoms or ions. For a perfect crystal, this repeating pattern contains no flaws, discontinuities or impurities, at a temperature of 0K. Any divergence from this repeating pattern is termed a defect within the structure. In practical materials, a perfect crystal structure is impossible to achieve, so some degree of defects is always present. Defects may have extensive influences on the properties of the materials, so accounting for their presence is necessary within the scope of material sciences.

Defect may be classified as either 0-, 1-, 2- or 3-dimensional, depending on how they extend in space. 0-dimensional defects, also called point defects, comprise flaws in the crystal structure localized to a single point, such as vacancies interstitial atoms and single atom impurities. 1-dimensional defects include dislocations like displacements along a single direction in the structure; 2-dimensional defects include grain boundaries, interfaces and surfaces; and 3-dimensional defects are flaws like precipitation of a different phase, within the primary material.

2.3.1. Kröger-Vink Notation

Within defect chemistry, the defect species themselves are treated as chemical species, with chemical equations and concentrations that vary with conditions. The most commonly utilized notation to represent these defects and their concentrations, is the Kröger-Vink notation.[18]

Within the Kröger-Vink notation, defect species are assigned a symbol of the general form S_{site}^{charge}. S represents the chemical species under consideration. The $site$ subscript describes, in a

perfect crystal, what should be present at the current site of S. Finally, the charge superscript represents the formal charge of species S, while it is situated at $site$. S does not have to be an atomic species but may also represent defect species, such as vacancies. Within the consideration of a metal oxide species MO, metal and oxygen ions situated at their appropriate lattice sites are denoted M_M^x and O_O^x, respectively. Metal- and oxygen ion vacancies, for instance, are denoted v_M'' and $v_O^{\bullet\bullet}$, where $'$ and * represent formal negative and positive charges, respectively.

The relevant species for the NiO and ZnO systems are described in Table 2-1:

Table 2-1 Kröger-Vink notation for relevant species of the NiO-ZnO system.

Species	Kröger-Vink notation
Nickel vacancy	v_{Ni}''
Zinc vacancy	v_{Zn}''
Oxygen vacancy	$v_O^{\bullet\bullet}$
Electron	e'
Electron hole	h^*
Lithium substituted nickel ion	Li_{Ni}'
Aluminum substituted zinc ion	$Al_{Zn}^{\bullet}$

2.3.2. Intrinsic Defects in NiO and ZnO

NiO and ZnO are p- and n-type semiconductors, respectively. These characteristics are closely tied to certain defect reactions being more prevalent within the intrinsic material, as governed by thermodynamics.

For NiO, being an intrinsic p-type semiconductor, the dominant free charge carrier is electron holes. Charge carriers form within an intrinsic material as a consequence of the need to maintain electronic neutrality within the material upon the formation of a charged defect. Consequently, it may be expected that the dominant intrinsic defect of NiO are nickel ion vacancies, which may form by the reaction with oxygen:

$$\frac{1}{2}O_2(g) = v_{Ni}'' + O_O^x + 2h^{\bullet} \qquad \text{2-22}$$

From this reaction, it is expected that the concentration of both nickel vacancies and electron holes will vary with the external oxygen partial pressure pO_2. Nickel vacancies may form by other processes, such as evaporation of nickel ions from the NiO lattice:

$$Ni_{Ni}^{x} = v_{Ni}'' + 2h^{\bullet} + Ni(g) \qquad 2\text{-}23$$

This process would predominantly occur under higher temperature conditions, but the chemical activity of both nickel and oxygen in the surroundings of the NiO material, will affect the charge carrier concentration. The dissociation of nickel ions from the bulk would not necessarily be compensated by the formation of electron holes, however. The dissociation may also occur accompanied by an oxygen ion; where an oxygen vacancy compensates the charge instead.

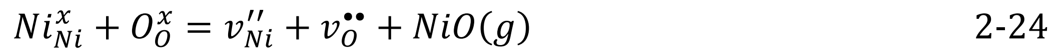

$$Ni_{Ni}^{x} + O_{O}^{x} = v_{Ni}'' + v_{O}^{\bullet\bullet} + NiO(g) \qquad 2\text{-}24$$

This reaction would have no effect on the electronic charge carrier concentration, however.

The intrinsic conductivity of NiO is too low for the pure material to be of practical use. Hence, to increase the hole concentration, NiO may be doped with lower valent lithium, which forms the species Li_{Ni}' within the NiO material. As this species has a negative formal charge, the defect must be compensated, either by the formation of a positively charged defect, or the consumption of a negatively charged one. The doping reaction process may thus occur by one of two processes:

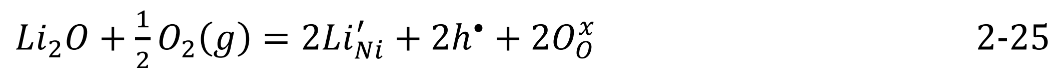

$$Li_2O + \frac{1}{2}O_2(g) = 2Li_{Ni}' + 2h^{\bullet} + 2O_{O}^{x} \qquad 2\text{-}25$$

$$Li_2O + v_{Ni}'' = 2Li_{Ni}' + O_{O}^{x} \qquad 2\text{-}26$$

The first equation shows that both the solubility of lithium in the NiO structure, as well as the extent of electron hole formation, increases with pO_2. The latter of the two processes is unfavorable for the production of p-type semiconductors, as it does not produce electron holes; under the doping process of NiO, controlling the environment to obtain the first reaction is preferable.

ZnO is intrinsically an n-type semiconductor, with, conversely to NiO, electrons as the dominant charge carriers. The origin of the intrinsic n-type conductivity of ZnO is still a debated matter in literature, so the dominant process is not known, but charge carrier electrons within ZnO may form by several defect reactions. Either by intrinsic reactions, such as the formation of oxygen vacancies or zinc interstitials, or by extrinsic reactions such as hydrogen doping. Zinc interstitials and oxygen vacancies may form by metal excess and oxygen deficiency reactions, respectively:

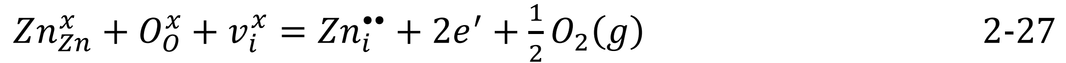

$$Zn_{Zn}^{x} + O_O^{x} + v_i^{x} = Zn_i^{\bullet\bullet} + 2e' + \frac{1}{2}O_2(g) \qquad 2\text{-}27$$

$$O_O^{x} = v_O^{\bullet\bullet} + 2e' + \frac{1}{2}O(g) \qquad 2\text{-}28$$

Differently to the p-type NiO, the intrinsic charge carrier concentration of ZnO would be reduced at high pO_2. Alternatively, at high temperatures, the metal excess may arise from gaseous metal in the surroundings:

$$Zn(g) + v_i^{x} = Zn_i^{\bullet\bullet} + 2e' \qquad 2\text{-}29$$

Extrinsically, n-type behavior may occur by hydrogen doping under reducing conditions by the reaction

$$H_2(g) + 2O_O^{x} = 2(OH)_O^{\bullet} + 2e' \qquad 2\text{-}30$$

The behavior of hydrogen as a donor in ZnO is a relatively unique behavior, as hydrogen usually acts as an amphoteric dopant, counteracting the dominant conductivity of a semiconductor. In ZnO, however, it will always assume a positively charged arrangement, and act as a donor.

Evidence exists to suggest the significance of a different hydrogen defect species in the unintentional n-type doping of ZnO (see section 4.2), the $H_O^{\bullet}$ species. While the exact reaction is not known, the possibilities include

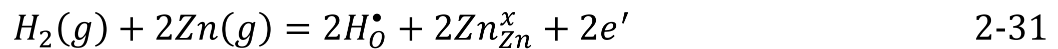

$$H_2(g) + 2Zn(g) = 2H_O^{\bullet} + 2Zn_{Zn}^{x} + 2e' \qquad 2\text{-}31$$

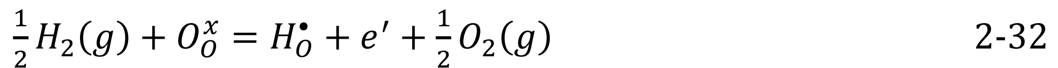

$$\frac{1}{2}H_2(g) + O_O^{x} = H_O^{\bullet} + e' + \frac{1}{2}O_2(g) \qquad 2\text{-}32$$

ZnO is doped to increase the electron concentration for practical applications, with the higher valent aluminum to act as an electron donor, forming the Al_{Zn}^{*} species:

$$Al_2O_3 = 2Al_{Zn}^{\bullet} + v_{Zn}'' + 3O_o^x \quad \text{2-33}$$

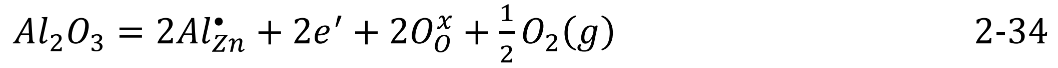

$$Al_2O_3 = 2Al_{Zn}^{\bullet} + 2e' + 2O_O^x + \frac{1}{2}O_2(g) \quad \text{2-34}$$

Similarly to the intrinsic free electron formation process, the doping process of ZnO would preferentially proceed the favorable doping reaction in the presence of lower pO_2.

Within the partially soluble system of NiO-ZnO, the mixed phase systems will exhibit high concentrations of the Ni_{Zn}^x and Zn_{Ni}^x species. Nominally, these will have little to no effect on the respective systems as defects. Results in section 5.2.1 would appear to disagree, however.

2.4. p-n Junctions

In electronics, there are two types of semiconductors; p- and n- type. These two types of semiconductors naturally have, at temperatures above 0 K, an equilibrium excess of positive and negative charge carriers, respectively. p-n junctions are formed when these two types of semiconductors are brought together to form a single system.

The majority of p-n junctions utilized in modern electronics are doped silicon semiconductors, being examples of homojunctions: the p- and n- type materials have equivalent band gap and intrinsic band level but differing Fermi levels due to the presence of the dopants, as shown in Figure 2-4.

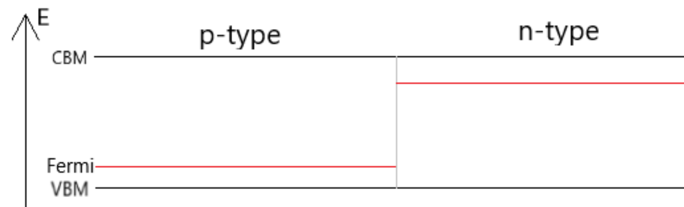

Figure 2-4 Diagram of band edges in p-n homojunction prior to equilibration of fermi levels. The red lines represent the respective Fermi levels of the p- and n-doped semiconductors on their respective sides.

Upon formation, this static junction is unstable, with two differing energy levels within the same system. To obtain a thermodynamic equilibrium, the Fermi levels of both semiconductors must be equalized with one another. When the junction is first formed, a very steep concentration gradient of charge carriers is formed at the interface. Consequently, the charge carriers will tend to diffuse across the junction and into the opposite semiconductor where the opposite charge carrier is dominant, and combine, neutralizing both charges. This process continues until an equilibrium is reached between the rate of charge carrier diffusion, and charge carrier drift in the opposite direction. At this point, a charged depletion zone with low charge carrier concentration has formed around the interface of the two semiconductors. This charged region contains an excess of depleted acceptor- and donor- defects of the p- and n- type semiconductors, respectively, as shown in Figure 2-5.

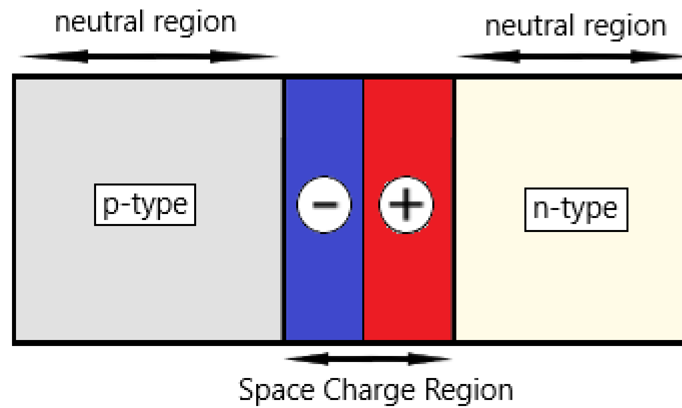

Figure 2-5 Diagram of a p-n junction at thermodynamic equilibrium. The regions labeled as neutral have equal concentration of charge carriers and dopant ions while the space charge region has an excess of depleted acceptors and donors, in the negative and positive regions, respectively.

For investigating the properties of a p-n junction, the two main laws of electromagnetic theory are Gauss's law, which relates the first derivative, or divergence, of an electric field to the charge density:

$$\nabla\mathcal{E}(x,y,z) = \frac{\rho(x,y,z)}{\varepsilon} \qquad \text{2-35}$$

and Poisson's equation, which relates the second derivative, or Laplacian, of the electric potential to the same:

$$\nabla^2 \varphi(x, y, z) = -\frac{\rho(x,y,z)}{\varepsilon} \qquad \text{2-36}$$

where ε is the permittivity. The assumption that the junction extends effectively infinitely along the plane parallel to the junction, so that there are no surface effects, reduces the problem to one dimension, perpendicular to the junction. The simplified form of Poisson's equation for this case is

$$\frac{d^2\varphi}{dx^2} = -\frac{\rho}{\varepsilon_{semi}} = -\frac{q}{\varepsilon_{semi}}(p - n + N_d - N_a) \qquad \text{2-37}$$

where $N_{d,a}$ are the concentrations of electron donors and acceptors, p and n are the hole and electron densities, both respectively, ε_{semi} is the semiconductor dielectric constant, and q is the charge of the carrier under consideration.

Solving this equation may be simplified by invoking the full depletion approximation. Within the scope of this approximation, the depletion region is considered fully absent of free charge carriers (see Figure 2-6), with a discontinuous transition into the effectively charge neutral regions:

$$\rho \cong \begin{cases} q(N_d - N_a) & -x_p < x < x_n \\ 0 & x_n < x \\ 0 & x < -x_p \end{cases} \qquad \text{2-38}$$

where x_p and x_n are the p- and n-type depletion region widths, respectively.

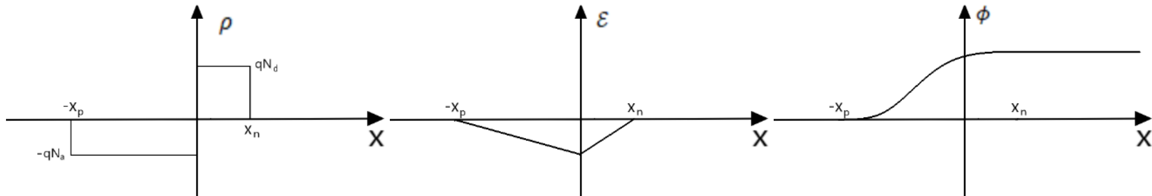

Figure 2-6 Diagrams demonstrating the full depletion approximation. From left to right, the diagrams outline the charge density, electric field, and potential field. The p- and n-type behavior is on the left and right of each diagram.

Under the full depletion approximation, the total charge of the depletion region, and thus the maximum electric field is a linear function of the region's width:

$$\mathcal{E}_{max} = -\frac{qN_d x_n}{\varepsilon_s} = -\frac{qN_a x_a}{\varepsilon_s} \qquad \text{2-39}$$

From this equation the junction potential, or more usefully, the total junction potential $\phi_{I,homo}$ (for a homojunction) with an applied potential V_a may be written as:

$$\phi_{I,homo} - V_a = -\frac{\mathcal{E}_{max}(x_n + x_p)}{2} \qquad \text{2-40}$$

Under the constraint that the total charge on both sides of the junction must be of equal magnitude and opposite sign to one another, the respective widths of the depletion layers are obtained from using Gauss's law to obtain an expression for the electric field across the junction, as well as the effect of an applied voltage:

$$x_p = \sqrt{\frac{2\varepsilon_{semi}}{q}\frac{N_d}{N_a}\frac{1}{N_a + N_d}\left(\phi_{I,homo} - V_a\right)} \qquad \text{2-41}$$

$$x_n = \sqrt{\frac{2\varepsilon_{semi}}{q}\frac{N_a}{N_d}\frac{1}{N_a + N_d}\left(\phi_{I,homo} - V_a\right)} \qquad \text{2-42}$$

The shape of the physical depletion region is gradual at the edges, but for many purposes, the full depletion approximation is sufficient, provided the depletion region is not too thin. As can be seen from the form of this equation, the width of the depletion layer varies with the applied potential: If the direction of the applied potential is opposite the internal potential, the depletion region shrinks.

The formation of the depletion region and its corresponding space charge affects the level of the energy bands that electrons and holes are permitted to occupy in the vicinity of the interface, causing them to shift. When the depletion region has reached equilibrium, the Fermi levels of both materials are the same, and the band edges have shifted accordingly, as shown in Figure 2-7.

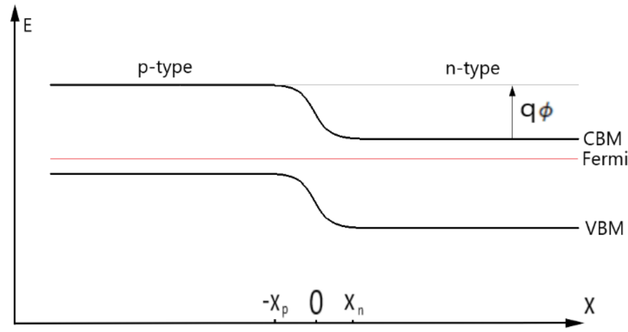

Figure 2-7 Band bending upon achieving thermodynamic equilibrium between the p- and n-doped semiconductors. x_p and x_m correspond to the edges of the p- and n-type depletion regions, respectively, and 0 corresponds to the space charge transition point between p- and n-type. $q\phi$ represents the extent of the shift.

These shifts in the band energy levels represents a barrier to carrier transport across the junction, called the built-in potential. For a homojunction, the built-in potential is equal to the difference between the Fermi level of the p- and n- sides, divided by the electronic charge. Alternatively, it may be expressed in terms of donor and acceptor concentration,

$$\phi_{I,homo} = \frac{kT}{q} \ln\left(\frac{N_d N_a}{n_i^2}\right) \quad 2\text{-}43$$

where n_i^2 is the intrinsic carrier concentration. Due to the built-in potential, the dominant charge carriers on either side cannot cross the junction freely, an external potential must be applied for this to occur at any appreciable rate. Depending on the direction of this potential, the band bending, and consequently the charge carrier transport behavior, responds in different manners.

If a negative potential is applied to the p-type and a positive potential is applied to the n-type, the junction is under reverse-bias. In this state, the bending that occurred during the thermodynamic equilibration of the junction is further exaggerated, widening the depletion region, and decreasing the charge carrier flux across the junction. The total band bending, that is, the displacement of the valence and conduction bands relative to one another across the junction, is equal to:

$$\Delta E_{C,V} = q(\phi_{I,homo} - V_a) \quad 2\text{-}44$$

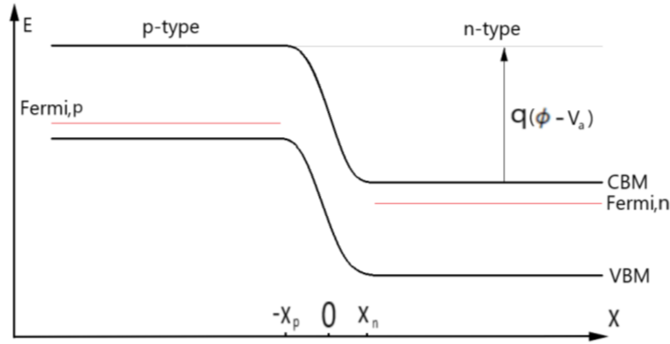

Figure 2-8 Band bending diagram of doped homojunction under reverse bias. p- and n-doped behavior to the left and right, respectively. x_p and x_m correspond to the edges of the p- and n-type depletion regions, respectively, and 0 corresponds to the space charge transition point between p- and n-type. $q(\phi - V_a)$ represents the extent of the shift under applied bias.

If the potential is reversed relative to the previous case, the junction is forward biased. In this case, the band bending from the thermodynamic equilibration is counteracted, and the band levels of the two semiconductors are brought back towards the same energy. When the forward bias external potential is equal to the internal potential of the junction, a flat band structure where there is no band level energy difference (ideally) between the p- and n- sides. In this state, charge carriers may move freely (with respect to potential) across the junction.

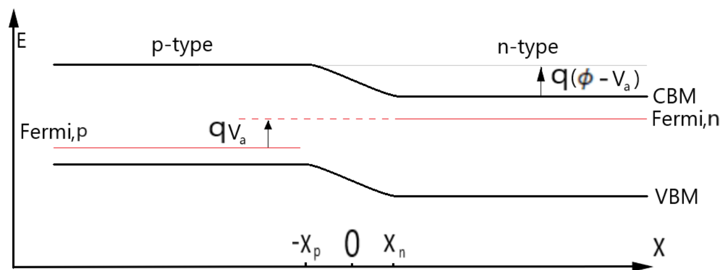

Figure 2-9 Band bending diagram of doped homojunction under forwards bias. p- and n-doped behavior to the left and right, respectively. x_p and x_m correspond to the edges of the p- and n-type depletion regions, respectively, and 0 corresponds to the space charge transition point between p- and n-type. $q(\phi - V_a)$ represents the extent of the shift under applied bias. qV_a is the difference between the fermi levels.

2.4.1. Fermi Levels of Approximate and Practical Semiconductors

Constructing the band bending diagrams for the various interfaces requires the determination of the Fermi levels of the practical materials. The two scenarios of both undoped and doped semiconductors will be considered. In the former case, the intrinsic Fermi level is utilized.

The intrinsic Fermi level of a material is usually near the middle of the band gap. However, to determine the band bending, both for doped or undoped materials, the exact level must be known.

The intrinsic Fermi level of a material may be determined from the band edge energy levels and the effective density of states. For non-degenerate semiconductors, where the following expression applies,

$$E_{VBM} + 3kT \leq E_F \leq E_{CBM} - 3kT \qquad \text{2-45}$$

the intrinsic Fermi level may be determined from the following formula:

$$E_i = \frac{E_{CBM}+E_{VBM}}{2} + \frac{3}{4}kTln\left(\frac{m_h^*}{m_n^*}\right) \qquad \text{2-46}$$

The values $m_{n,h}^*$ are the effective electron and hole masses within the material, and may be determined from the band structure of the material according to the equations:

$$v_{n,p}(k) = \frac{1}{\hbar}\frac{\partial \varepsilon}{\partial k} \qquad \text{2-47}$$

$$m_{n,p}^* = \left(\frac{1}{\hbar^2}\frac{\partial^2 \varepsilon}{\partial k^2}\right)^{-1}\Bigg|_{at\ k=0} \qquad \text{2-48}$$

The first equation relates the curvature of the band structure with group velocities of the electrons and holes for the conduction and valence bands, respectively, while the second equation relates the effective mass of the carrier with the second derivative of the band structure at the band gap transition point.

Effective masses of charge carriers are utilized for several purposes. The primary interest in this thesis is the density of states effective mass, however the conductive effective mass is also useful. The total effective masses are calculated utilizing separate forms of averages. The density of states effective mass is obtained from the geometric mean of separate effective masses, by the equation

$$m_{DOS}^* = \left(g^2 \prod_i^N m_i^*\right)^{\frac{1}{N}} \qquad \text{2-49}$$

where g is a degeneracy factor equal to the number of equivalent band edge extrema within the Brillouin zone, m_i^* is the ith non-equivalent effective mass, and N is the total number of effective masses of the band gap transition point. The conductive effective mass is primarily useful as it is commonly used in literature to report experimental values and serves as a convenient means of comparison. The conductive effective mass is calculated by a harmonic mean, by the equation

$$m_{cond}^* = N \left(\sum_i^N \frac{1}{m_i^*} \right)^{-1} \quad \text{2-50}$$

with the same symbols as equation $m_{DOS}^* = (g^2 \prod_i^N m_i^*)^{\frac{1}{N}}$
2-49.

For doped semiconductors, the Fermi levels of doped semiconductors at thermodynamic equilibrium are obtained from the intrinsic Fermi level by the equations:

$$E_F = E_i + kT \ln \frac{n_o, p_0}{n_i} \quad \text{2-51}$$

for n- and p-type semiconductors, respectively, where n_i is the intrinsic carrier concentration

$$n_i = \sqrt{N_c N_v} e^{-\frac{E_g}{2kT}} \quad \text{2-52}$$

N_c and N_v are the effective density of states in the conduction and valence bands, respectively:

$$N_{c,v} = 2 \left(\frac{2\pi m_{e,h}^* kT}{h^2} \right)^{\frac{3}{2}} \quad \text{2-53}$$

n_o, p_0 are the carrier densities at thermal equilibrium. If the concentration of one dopant dominates in concentration over the other, the carrier density may be expressed as:

$$n_0 = -\frac{N^* + N_a}{2} + \sqrt{\frac{(N^* + N_a)^2}{4} + N^*(N_d - N_a)} \quad \text{2-54}$$

$$N^* = \frac{N_c}{2} e^{\left(\frac{E_d - E_c}{kT} \right)} \quad \text{2-55}$$

where E_d is the donor energy. An equivalent expression applies for hole concentration.

While the previous equations assumed non-degenerate semiconductors, transparent doped semiconductors such as ZnO, are very commonly degenerate. In a degenerate system, the Fermi level lies within $3kT$ of the band edges. Degenerate systems complicate matters, as the approximations necessary for analytically obtained Fermi level values fail to provide an accurate description, and numerical methodologies must be employed to obtain an accurate result.

An alternative to the numerical solution methodology, is to use the Joyce-Dixon approximation for degenerate semiconductors:[19]

$$\frac{E_F - E_C}{kT} \cong \ln \frac{n_0}{N_c} + \frac{1}{\sqrt{8}} \frac{n_0}{N_c} - \left(\frac{3}{16} - \frac{\sqrt{3}}{9}\right) \left(\frac{n_0}{N_c}\right)^2 + \cdots \qquad \text{2-56}$$

2.4.2. Heterojunctions, and How They Differ

In the previous section, the most commonly utilized homojunctions were utilized to demonstrate the basic properties of p-n junctions. Homojunctions are formed of two differently doped sections of the same material: In this case, the band levels are initially equal, but the Fermi levels differ due to the presence of the dopants, which causes the band levels to shift. Heterojunctions, however, are the resulting interface from two different crystalline materials, with intrinsically different band levels and Fermi energies. These two junction types follow the same basic principle with respect to band bending, but there are also some behaviors unique to heterojunctions.

Heterojunctions may form different arrangements of band alignment structures based on what materials they are constructed from, classified into three different categories based on the relative locations of the valence- and conduction band edges: Type I, II and III. A graphical description is given in Figure 2-10.

Figure 2-10 Schematic representation of possible band gap arrangements for heterojunctions, types I, II and III in order from left to right.

In heterojunctions, the differing band alignments cause the built-in potential, and consequently the band bending, of the junction to act in a somewhat different manner from homojunctions upon formation. As a convention to be utilized through this thesis, the band offset ΔE_c is positive for $E_{c,n} > E_{c,p}$, and the band offset ΔE_v is positive for $E_{v,n} < E_{v,p}$. The built-in potential for a doped heterojunction is then described by the equations:

$$\phi_{I,hetero} = \phi_{I,p} + \phi_{I,n} \qquad 2\text{-}57$$

$$q\phi_{I,hetero} = \frac{\Delta E_C - \Delta E_V}{2} + kT \ln\left(\frac{N_d N_a}{n_{i,n} n_{i,p}}\right) + \frac{kT}{2} \ln\left(\frac{N_{v,n} N_{c,p}}{N_{c,n} N_{v,p}}\right) \qquad 2\text{-}58$$

The equation for calculating the width of the depletion region mostly follows the same principles as for a homojunction. However, unlike in a homojunction, each material has a different dielectric constant, and responds differently to an electric field. Thus, the shape of the depletion region depends on the relative dielectric constants of the p- and n- type materials:

$$x_p = \sqrt{\frac{2\epsilon_{s,p}\epsilon_{s,n}}{q} \frac{N_d}{N_a} \frac{(\phi_I - V_a)}{(N_a \varepsilon_{s,p} + N_d \varepsilon_{s,n})}} \qquad 2\text{-}59$$

$$x_n = \sqrt{\frac{2\epsilon_{s,p}\epsilon_{s,n}}{q} \frac{N_a}{N_d} \frac{(\phi_I - V_a)}{(N_a \varepsilon_{s,p} + N_d \varepsilon_{s,n})}} \qquad 2\text{-}60$$

A unique trait of heterojunctions that is not found in homojunctions is that, due to the band level mismatch, discontinuities in the band bending may occur, shown in Figure 2-11. If the depletion region of the junction is narrow, these discontinuities may form potential wells for charge carriers, forming a localized quantized system with corresponding charge carrier transition levels. In a physical system, this requires a sharp junction without defect states, and is not achievable in practice for many combinations of materials.

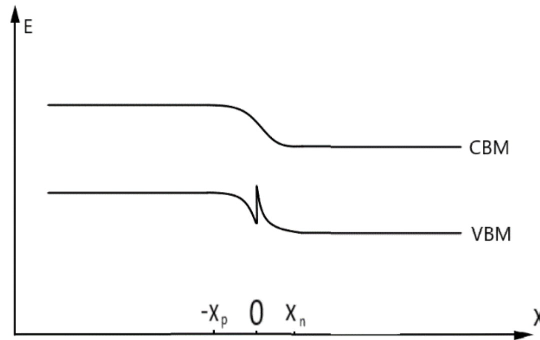

Figure 2-11 Diagram of discontinuous band bending in heterojunction band structure, in a type II staggered gap. The discontinuity is in this case in the VB structure, which could potentially form a hole potential well. Discontinuities may equivalently form in the CB structure as well.

Due to the different potential levels of the p- and n-type band edges, heterojunctions exhibit separate potential barriers for electrons and holes across the junction. These potentials are also separate from the built-in potential. There are two possible scenarios, producing different barrier heights. The barriers are demonstrated in Figure 2-12:

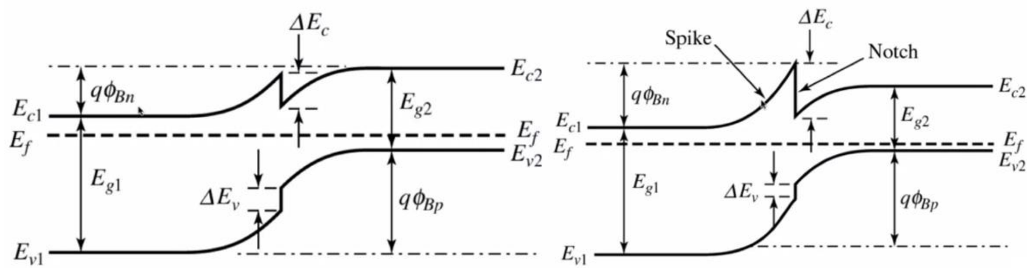

Figure 2-12 Diagram describing the origin of electron and hole barriers of a heterojunction. Left image: Small conduction band offset. Right image: Large conduction band offset. n-type semiconductor to the left, p-type semiconductor to the right in both images. Figures from reference.[20]

For the scenario described by the left image, with the spike at the interface lower than E_{c2}, in a system where the Fermi levels of the materials are equalized, the barrier heights for electrons and holes are equal to the conduction- and valence band offsets (CBO and VBO), respectively. In the scenario described by the right image, the spike at the interface of the interface is at a higher energy than E_{c2}. In this case, the electron barrier is decided by the band bending in the material producing the left-side band gap.

These barriers act similarly to Schottky barriers, and charge carriers may flow past them by two different mechanisms; either by thermionic emission, or by diffusion current. In the case with the

smaller spike (left image), the diffusion current dominates. In this case, both the electron and hole currents are independent of the ΔE_c value, and rather depends on the $\phi_{Bn/p}$ values. In the case shown in the right image, the rate is determined by the thermionic emission current, which is directly dependent on the ΔE_c value, along with the built-in potential. The dependence of the electron current on the barrier in the latter case is given as

$$I_n \sim e^{-\frac{q\phi_{Bn}}{kT}} \quad \text{2-61}$$

and equivalently for holes. In this case, applied forward bias only reduces the barrier height by the extent the n-type semiconductor is shifted in energy. Consequently, the increase in current with voltage is lower compared to the junctions where diffusion current dominates.

2.5. Diodes and Transport Properties

Diodes are an integral part of all modern electronics, but differently constructed p-n junctions display different characteristics and behavior. This behavior is explained by the Shockley diode equation for an ideal diode:[21–23]

$$I = I_0 \left[\left(\frac{e(V - IR_s)}{\eta_{id} kT} \right) - 1 \right] \quad \text{2-62}$$

In this equation, I is the current across the diode, I_0 is the reverse saturation current, e is the elementary charge, V is the voltage across the diode, and η_{id} is an ideality factor. Most of these properties are either fundamental constants, or variables that are adjusted in an experimental setting. The parameter of primary interest to a theoretical analysis is the reverse saturation current:

$$I_0 = eAn_i^2 \left(\frac{1}{N_d} \sqrt{\frac{D_p}{\tau_p}} + \frac{1}{N_a} \sqrt{\frac{D_n}{\tau_n}} \right) \quad \text{2-63}$$

In this equation, A is the cross-sectional area, $D_{p,n}$ are hole and electron diffusion coefficients, respectively, $N_{d,a}$ are dopant and acceptor concentrations at n- and p- side, respectively, and τ are charge carrier lifetimes.

The components of the ideal diode equation cannot be directly calculated from DFT, so it must be decomposed and reformulated in terms of parameters that are available, given in Table 2-2:

Table 2-2 Components of the ideal diode equation and their definitions.

Charge Carrier Diffusion Coefficient	$D_{n,p}$	$\frac{\mu_{n,p} k_B T}{e}$	μ is the charge carrier mobility e is the elementary charge
Series Resistance	R_s	$\frac{1}{e(n\mu_n + p\mu_p)}$	n and p are the charge carrier concentrations.

The difficulty lies with the calculation of the transport properties of the carriers within the materials: the carrier mobilities. These values depend explicitly on temperature, so for a methodology that only calculates absolute zero properties, significant extra steps must be implemented to account for the vibrational properties of the materials.

The Shockley diode equation, being an ideal model, neglects the effects of physical defects in the diode under consideration. While this makes a good model for describing common homojunctions, that may be produced with extremely low defect concentrations and similarly near perfect junction, in a heterojunction between two differing crystal structures the ideal assumptions break down. In particular, for a heterojunction, properties at the interface and the immediate adjacent regions, may have considerable effects. Surface recombination of charge carriers is one process that might be expected to show considerable effects. The recombination rate per area for the interface is described by the equation[21]:

$$U_{SR} = \frac{pn - n_i^2}{p + n + 2n_i \cosh\left(\frac{E_i - E_{st}}{kT}\right)} N_{st} v_{th} \qquad \text{2-64}$$

where E_{st} is the surface trap energy, N_{st} the surface trap density in a two-dimensional interface, and v_{th} the thermal velocity, equal to the mean free path divided by collision time. The recombination rate represents essentially lost efficiency for purposes of photoelectric generation,

but also an increase in the junction recombination – generation current, by the Shockley-Hall-Read process. It is essentially the same process as the interface recombination rate, facilitated by traps, but extends into the depletion regions of both semiconductors. The equation describing the rate is nearly equivalent to U_{SR}, except the trap density is three-dimensional, and the total rate is dependent on the cross-sectional area parallel to the interface. The generated current is described as:

$$J_{SHR} = \sigma q \int_{-x_p}^{x_n} U_{SHR}\ dx \quad (2\text{-}65)$$

where σ is the cross sectional area and q is the charge of the charge carrier under consideration. Strictly, this applies only for a single trap energy, so the integral should also be over trap energies from the valence to the conduction band.

2.6. Wulff Construction

When crystals are allowed to grow freely in space, they tend to assume structures characteristic of the material they are composed of. Prediction of the equilibrium structure for a given material is done using the principles of Wulff construction.

Wulff construction is a method for determining the equilibrium shape of a crystal or other shape of fixed volume within a separate phase, based on energy minimization. The methodology assumes that a crystal will assume the structure which minimizes the surface free energy, defined by the quantity

$$\Delta G_i = \sum_j \gamma_j O_j \quad (2\text{-}66)$$

where ΔG_i is the difference in free energy between a crystal and the equivalent configuration of particles within a bulk material, γ_j is the surface free energy of surface j, and O_j is the corresponding area of this surface.

In order to minimize the quantity of equation 2-66, a condition must be fulfilled, namely that for a given crystal a vector h_j, normal to surface j, representing the length from the center of the crystal to the surface will be proportional to the surface free energy, described by the equation

$$h_j = \lambda \gamma_j \qquad 2\text{-}67$$

where λ is a proportionality constant. Equations 2-66 and 2-67 together constitutes the Gibbs-Wulff theorem.[24]

The Wulff construction methodology only accounts for the surfaces of the crystal, while neglecting the edges and corners that arise at the transitions between these. The justification for the neglect, is that these energies are higher-order, and do not affect the thermodynamics. Further, the proofs of the Gibbs-Wulff theorem only apply at zero kelvin, so divergence from the equilibrium structure in real systems is to be expected.

3.Methodology

3.1. Implementation

This project uses the Vienna Ab initio Simulation Package (VASP)[25–27] to perform all DFT calculations. VASP is a program for calculating atomic scale electronic structure from first principles, or *ab initio*. The program is specialized for handling materials, or more generally systems with systematically repeating structures.

3.1.1. Planewave Basis Set

In this project, a plane wave basis set is utilized. Plane waves do not utilize atom centered basis functions that target electronic orbitals like conventional basis sets but are rather aimed at the entire system. The computational load thus scales with n^3, where n is the number of orbitals in the system.[28]

The idea behind plane waves is that, as a system expands into infinity, the originally discrete molecular orbitals combine into bands. These bands may be described by plane waves, of the form:

$$\chi_k(r) = e^{ikr} \tag{3-1}$$

The value k is a wave vector, which may be interpreted as a position in reciprocal space.

The usefulness of utilizing a plane wave basis is based in Bloch's theorem, which shows that the wavefunction ϕ_n of a band n for a periodic system may be written as the product of a plane wave- and a periodic part:

$$\psi_{n,k}(r) = e^{ikr}\varphi_n(r) \quad \text{3-2}$$

The periodic part matches the periodicity of the unit cell lattice. The complete wave function of the system may thus be written as an infinite sum of plane waves:

$$\psi_{n,k}(r) = \sum_G c_{n,(k+G)} e^{i(k+G)r} \quad \text{3-3}$$

The values $c_{n,(k+G)}$ are the plane wave coefficients, and G are components of the infinite set of reciprocal lattice vectors that fulfill the requirement,

$$G * R = 2\pi m \quad \text{3-4}$$

where R is one of the unit cell lattice vectors and m is a positive integer.

Plane wave basis sets would like all other basis sets, for a complete description of the system, require an infinite number of basis functions. In practice, the plane wave basis set is truncated according to the kinetic energy of the plane waves:

$$E_{cut} \geq \frac{1}{2}|k + G|^2 \quad \text{3-5}$$

The k-points of a system are also infinite in theory, but in practice the wave function varies little between k-points so long as their spacing in reciprocal space is small enough. Thus, only a suitable mesh of sample k-points are used in practice, and the number may be reduced utilizing the space group symmetry of the Bravais lattice. In practice, the number of such k-points must be increased until the calculated energy, or other property one is interested in, converges within a set limit with respect to the total number of k-points within the Brillouin zone.

3.1.2. Pseudopotentials

A plane wave basis has many advantages, but utilizing a basis set that is not centered on the individual atoms gives rise to a problem: There is no good way to properly describe the discontinuous cusp of electron density that occurs at the position of the nuclei with only a planewave basis, without increasing the number of planewaves to an excessively large number.

Also, for large atoms, it is for most purposes a reasonable approximation that there is no need to explicitly model the largely chemically inactive core electrons. Consequently, pseudopotentials are utilized to model these core electrons, and to smear the electronic charge of the nucleus and core electrons, reducing the necessary number of planewaves in a simulation. There are several models of pseudopotentials, but the type utilized in this project, the Projector Augmented Wave (PAW) method, is somewhat unique. Despite being considered a pseudopotential method, PAW formally retains all core electrons: The valence electrons are described by a plane wave basis, plus a core region contribution. The core contribution is expanded as the difference between the electron density of a calculation with all electrons for the isolated atom, and a set of nodeless pseudo-orbital, which allows the core contribution to adjust.

For the particulars of VASP pseudopotentials, see the following references.[29,30]

3.1.3. Supercell Approach

While pure, flawless materials may be modelled from solely the unit cell, altered systems usually cannot. When working with mixed phase systems, or any system differing from a perfect system, one would usually investigate these at certain percentage concentrations, in which case using a unit cell would often not allow. Furthermore, as the Bloch theorem does not apply if the periodicity of the system is lost, a supercell must be used.

A supercell is constructed from the unit cell by using two or more unit cells, and defining this new, larger structure as the new repeating unit under periodic boundary conditions. When a deviation from the pure material is introduced into the supercell, this defect is similarly repeated infinitely in periodic space. As the periodicity of the system is thus conserved, the Bloch theorem may be utilized. However, while the defect in question may be included into the system in this way, its concentration within the supercell defines its concentration throughout the system. Hence, to obtain particularly low concentrations of a defect, the size of the supercell rapidly grows to an unfeasible level, setting a limit to what concentrations may be considered.

For this project, the supercell approach is also necessary to correctly represent the magnetic structure of NiO for certain surfaces. The conventional rock salt structure NiO unit cell does not

allow for the antiferromagnetic arrangement of magnetic moments in NiO to be correctly represented.

3.1.4. Surfaces

Expanding upon the supercell approach, modelling surfaces with a plane wave basis requires a supercell with a vacuum region imbedded along at least one or more axes. This vacuum layer must be sufficiently wide the interactions between the periodically repeating slabs are negligible.

For nonpolar, electrically neutral slabs, this is not problematic. However, if the surface has a dipole moment, the system takes on the form of an infinitely repeating pattern of spaced out plates with electric fields between them, effectively creating a capacitor system. Dipole effects are thus corrected by adding a linear correction to the system, with a method akin to what is described in the reference.[31]

3.2. Calculations

3.2.1. Surface Energy Calculation

When a slab of a material is relaxed while exposed to a vacuum, the outermost layers of this slab will relax in a different manner from within bulk material in order to stabilize with respect to the new environment. However, the presence of a vacuum-surface interface is necessarily less favorable and is accompanied by an increase in the energy of the system. This increase in energy is called the surface energy of the exposed surface, and is calculated as:

$$E_{surf} = \frac{E_{slab} - E_{bulk}}{2A} = \frac{E_{slab} - N * E_{unit}}{2A} \quad 3\text{-}6$$

The bulk energy is defined as the average energy per atom in the bulk unit cell, multiplied by the number of atoms in the surface slab. The A term represents the area of the surface and is multiplied by two to account for the fact that two surfaces are always coupled together, one on either side of the slab.

For nonpolar surfaces, this coupling of surfaces is not an issue, as the same surface can be arranged on both sides of the slab. For polar surfaces, however, two different surfaces, one cation terminated, and one anion terminated surface are coupled together. In this case, the average of the two distinct surface energies is considered as the surface energy.

3.2.2. Band Alignment

When performing calculations on unit cells of materials, there is no way to determine the energy level with respect to a vacuum, and the energy levels resulting from a DFT calculation are placed relative to a rather arbitrary zero point for the energy. To determine the absolute scale energy levels, the energy level within the material must be determined relative to a vacuum. In practice, this is done by modelling a slab in a vacuum and determining the local potential throughout the slab. A planar average; That is, an average over the xy-plane of the slab to obtain a one-dimensional average of the local potential with the z-axis (or any other combination of axes), is calculated for the calculation cell. The planar average may be formally described by the formula

$$\bar{V}(z) = \frac{1}{S}\int_S V(x, y, z)dxdy \quad \text{3-7}$$

where $\bar{V}$ is the planar average, V is the property of interest, and S is the area of the cross section xy-plane.

The local potential planar average is rescaled such that the vacuum region corresponds with an energy level of zero, before the average of the local potential within the slab is determined. The average potential level within the slab is determined from a macroscopic averaging technique.

The macroscopic averaging technique serves to remove the oscillation of the local potential with the atomic positions. By defining a filter function w_a:

$$w_a(z) = \frac{1}{a}\Theta\left(\frac{a}{2} - |z|\right) \quad \text{3-8}$$

where $\Theta(z)$ is the Heaviside step function, the macroscopic average may be expressed as

$$\overline{\overline{V}}(z) = w_a(z-z')\bar{V}(z')dz' = \frac{1}{a}\int_{z-\frac{a}{2}}^{z+\frac{a}{2}} \bar{V}(z')dz' \quad 3\text{-}9$$

where a is a period parameter, equal to the distance between separate planes of the surface slab along the z axis, and z functions a center point value of the z coordinate.

This definition of the planar average only works for surfaces, where only a single period parameter works for the entire system. Is a second phase introduced into the same calculation cell, with its separate lattice parameter and structure, a second one dimensional averaging must be performed with a corresponding period parameter a'. Alternatively, rather than performing a second averaging, the averaging process may instead use an alternate filter function of two period parameters:

$$w(z) = \int w_a(z-z')w_{a'}(z')\,dz' \quad 3\text{-}10$$

in which case the macroscopic average is

$$\overline{\overline{V}}(z) = \int w(z-z')\bar{V}(z')\,dz' \quad 3\text{-}11$$

For determining the average value for an isolated surface, the macroscopic average potential at the coordinate corresponding to the center of the surface slab is selected.

The determined average energy level is set as the zero energy level with respect to all band levels. The position of the band edges themselves, relative to the determined zero level are determined from a unit cell bulk calculation, and may thus be described by:

$$E_{VBM/CBM} = E_{Local,slab\ average} + E_{bulk,VBM/CBM} \quad 3\text{-}12$$

In the heterojunction interface structures, a similar approach is employed, with one difference: A fitted trendline of the macroscopic average plots of both the slabs are extrapolated towards the center point of the interface. The value of the trendline at the point which it intersects the center of the interface, is set as the local potential of the slab for the interface. See Figure 3-1 for an example. From this determination, the offset of the VBM levels is calculated by the following formula:[32]

$$\Delta VBM_{hetero} = \Delta VBM_{bulk} + \Delta E_{Local,slab\ average} \quad 3\text{-}13$$

where the ΔVBM_{bulk} parameter is the difference between the valence band edges relative to the local potential in bulk calculations, and the $\Delta E_{Local,slab\ average}$ term is the difference between the macroscopic averages of the local potential in the interface. Hence, the first term may be considered a bulk term, and the second an interface interaction term.

For non-polar interfaces, the determination of $\Delta E_{Local,slab\ average}$ is straight forwards. For polar interfaces, the macroscopic average potential constantly shifts through the surface slabs, rendering the value at the center of the slabs an extensive property of the surface slab width. The tangent of the macroscopic average potential at the center of the surface slabs are thus extrapolated to the center of the interface gap, and the resulting values at the interface point is utilized to calculate $\Delta E_{Local,slab\ average}$.[33]

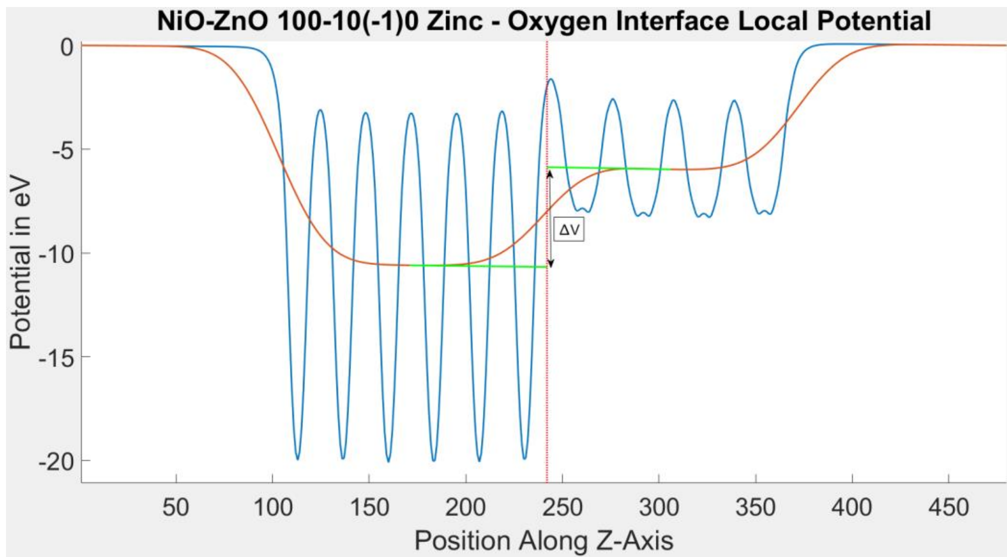

Figure 3-1 Local potential plot of the ⟨100⟩-⟨10$\bar{1}$0⟩ interface- The blue line is the planar average potential; the horizontal orange line is the macroscopic average. The vertical line is the center point of the interface gap, and the green lines are the tangents of the macroscopic average at the center of the component slabs, extrapolated to the center of the interface.

There is one issue with this approach, however. The desired VBM offset, for many purposes, is not that of the strained surface, but rather the strain free junction. To obtain this value, a correction must be implemented for appropriate treatment of the offset, with the resulting equation:[34]

$$\Delta VBM_{hetero}^{strain\,free} = \left(\Delta E_{VBM-Ref}^{A} - \Delta E_{Vac-Ref}^{A} + \Delta E_{Vac-Ref,X}^{A}\right) + \Delta E_{Ref,X}^{A-B} - \left(\Delta E_{VBM-Ref}^{B} - \Delta E_{Vac-Ref}^{B} + \Delta E_{Vac-Ref,X}^{B}\right) \quad 3\text{-}14$$

In this equation, the $\Delta E_{VBM-Ref}^{A}$ is the difference between the VBM level and the reference level for material A obtained by bulk calculation, $\Delta E_{Vac-Ref}^{A}$ is the difference between the reference level at the bulk-like center of the A slab and the vacuum level, in a surface where phase A is strain free, and $\Delta E_{Vac-Ref,X}^{A}$ is the difference between the reference level at the bulk-like center of the A slab and the vacuum level, under the strain conditions of the interface X. Equivalent terms apply for phase B. The $\Delta E_{Ref,X}^{A-B}$ term is the difference between the reference potentials of the A and B phases within the interface.

The conduction band offset values are calculated by adding the experimental band gaps, 3.37 eV and 3.70 eV for ZnO and NiO, respectively, and calculating the difference according to the formula

$$\Delta CBM = \left(VBM_{ZnO} + E_{g,ZnO}\right) - \left(VBM_{NiO} + E_{g,NiO}\right) \quad 3\text{-}15$$

3.2.3. Mixed Phase Band Edge Level

The relative band edge energies between the pure and mixed phase materials are calculated by aligning the average 1s orbital energies of the host material cation between the systems, according to the formula

$$\Delta VBM_{mix} = \Delta E_{core} + VBM_{conc} - VBM_{pure} \quad 3\text{-}16$$

where ΔE_{core} is the difference in core levels $\Delta E_{1s,host,pure} - \Delta E_{1s,host,mix}$, and $VBM_{conc/pure}$ are the VBM levels of the mixed and pure phase materials relative to the core states, respectively. The core levels of the mixed phase materials are determined from the average value across all host cations in the system.

It should be noted that this is not an exact method, but rather a commonly employed approximation. An exact methodology would require forming a single supercell from multiple supercells with different concentrations and calculating the relative VBM values within the same system.

3.2.4. Charge Carrier Transport

The charge carrier effective masses are calculated from the following equation:

$$m_{n,p}^* = \left(\frac{1}{\hbar^2}\frac{\partial^2 \varepsilon}{\partial k^2}\right)^{-1}\Bigg|_{at\ k=0} \qquad 3\text{-}17$$

The symmetry point that gives the lowest effective mass (sharpest curvature) is utilized for the calculation (designated k=0), which is commonly the transition points of the band gap: the VBM and CBM symmetry locations. The effective mass is calculated by preparing a high k-point density band structure at and between the relevant symmetry points of 1000 k-points per symmetry line and fitting a sixth order polynomial to the relevant energy bands. The fitting is required to achieve at least an R^2 coefficient of 0.9999 in the immediate vicinity of the k=0 point to be considered adequate. The second derivative of the band curvature is analytically derived from the fitted polynomial.

In the case of anisotropic effective masses, the fitting process is performed for each degenerate band, on different regions of the band around the k=0 point. The separate polynomial fittings for the anisotropic charge carrier masses are then treated identically to the isotropic equivalents.

The overall density of states effective mass is calculated utilizing a geometric mean, described by the equation

$$m_{DOS}^* = \left(g^2 \prod_i^L m_i^*\right)^{\frac{1}{L}} \qquad 3\text{-}18$$

where g is a degeneracy factor equal to the number of equivalent band edge extrema within the Brillouin zone, m_i^* is the ith non-equivalent effective mass, and L is the total number of effective masses of the band gap transition point.

3.2.5. Interface Energy Calculation

The calculation of the energy change that occurs with the formation of an interface is performed in a similar manner. In addition to the interface relaxation, two slabs with the same structure and applied strain as each slab in the interface is relaxed in a vacuum instead, and the total energy difference is utilized:

$$E_{interface} = \frac{E_{slab,1,2} - (E_{slab,1} + E_{slab,2})}{A} \quad \text{3-19}$$

In this case, as there is only a single interface between the slabs, the area is only included once.

3.2.6. Spatially Resolved DOS

In the interfaces and surfaces under consideration, the density of states is not consistent throughout the surface and interface structures, but rather varies considerably, depending on the environment. To show this behavior, pseudo-spatially resolved DOS graphs are utilized.

They are constructed is the following fashion:

1. The unit cell is divided into a suitable number of sections along the vacuum axis.
2. Atoms that fall into the same section are considered as a single part of the spatially resolved DOS.
    a. The atom resolved partial DOS of each atom that falls within a certain section are summed up, the total partial DOS sum is considered as the spatially resolved DOS for that section
3. The magnitude of the resulting sum DOS is rescaled with a cutoff density. Any state with a density above this value are set to the cutoff value.
    a. The cutoff density varies as necessary to represent surface and interface states as clearly as possible.
4. The resulting total DOS of each section is plotted as a surface plot, with relative position along the z-axis, energy level, and state density along the x-, y-, and z-axes, respectively. The plot orientation is standardly aligned such that the xy-plane forms a 2D plot,

representing density by the surface color scale, but may be tilted if this does not provide a good image of the available states.

a. The zero-energy level corresponds to the VASP calculation zero level and may be considered relatively arbitrary, but close to the VBM of the total system. The dipoles of most interfaces shift the energy to an extent that aligning the Fermi level properly cannot be done properly along a 1D axis.

For interfaces, the process is modified for the sectioning of step 1 to occur out from the interface center coordinate, to avoid the same sections including atoms from both constituent surfaces of the interface.

As an example of a spatially resolved DOS, se Figure 3-2:

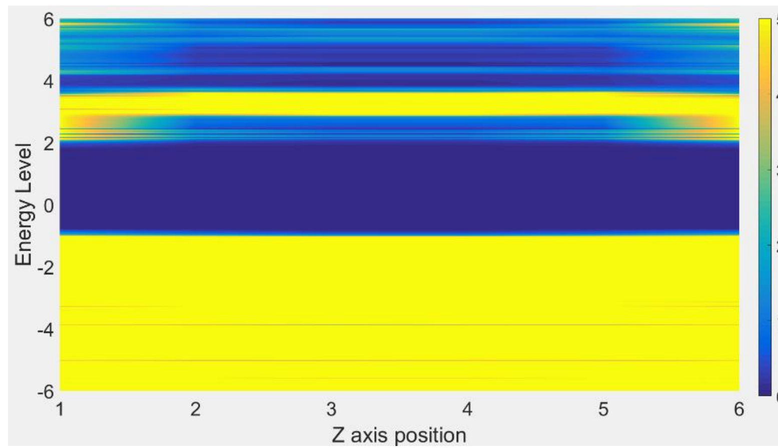

Figure 3-2 Spatially resolved DOS of the NiO ⟨100⟩ surface, calculated by PBE+U functional.

The z-axis position value represents the position of the ions providing the DOS states, as well as the point along the structure parallel to the vacuum axis. The extrema values, in this case 1 and 6, correspond to the surface edges. Each z-axis integer value may be considered to correspond to an individual ab-plane layer of ions.

The colors of the structures correspond with the density of states at the ionic layer of the structure, and energy level (in units eV) determined by the x and y axis of the 2D surface, respectively. The dark blue regions correspond to regions where no energy states are available, typically the band gap. The yellow regions correspond to energy levels where the density of states exceeds the cutoff threshold. Intermediate colors correspond to shallower states.

The bulk, and deep band states, seen at energy level -1 and down, are not of currently of interest but tend to exhibit very dense states, and have been truncated to a maximum value, appearing as continuous states in this diagram.

The key features in this spatial DOS structure lie at z-axis position 1 and 6, at energy level 2-3: The density is observed to considerably increase in these regions, indicating the formation of surface states at the CBM level. Rather than the density at the surfaces, the change in density towards the surfaces from the center of the slabs is the key indicator of surface states.

This example shows a non-polar surface, polar surfaces exhibit continuous change in VBM and CBM along the z-axis position. Interfaces have the corresponding interface transition along the z-axis noted in the image caption.

3.2.7. Induced Interface Electron Density

The change in charge distribution with the formation of the interface is calculated by the following formula:

$$\Delta\rho_{interface} = \rho_{interface} - \rho_{NiO\ Slab} - \rho_{ZnO\ Slab} \qquad 3\text{-}20$$

where the three terms are the total electron distribution of the interface structure $\rho_{interface}$, the total electron distribution of the relaxed NiO slab of the interface $\rho_{NiO\ Slab}$, with its electron distribution calculated separately in the absence of the ZnO slab, and equivalently for the ZnO slab for $\rho_{ZnO\ Slab}$. The $\Delta\rho_{interface}$ charge distribution is then averaged along the ab-planes, to give a planar average of the induced charge density.

3.2.8. Bader Analysis

Bader analysis utilizes the Bader charge analysis program, see references.[35–38]

3.3. Calculation Settings, Convergence and Calculation Procedures

The calculations are set to have convergence parameters with respect to energy of 1E-6 electron volts per electronic calculation iteration, the cutoff force on any particle in the system must be less than 0.02 eV/Å for the structure to be considered converged. All structures, except unit cell bulk calculations, were relaxed using the GGA+U functional. Hybrid PBE0 calculations were used only in a one-shot fashion on already relaxed structures.

3.3.1. Bulk and Interface Settings

Calculation Algorithm

If possible, the tetrahedron method with Blöch corrections (ISMEAR=-5) is utilized for final ionic relaxation and total energy calculation. If not, due to system size, a Gaussian smearing (ISMEAR = 0) of the partial occupancies is used instead, with a smearing width of 0.01 eV (SIGMA = 0.01).

The unit cell calculations utilize the smallest unit cell for both NiO and ZnO of four atoms.

GGA-PBE+U

The +U values utilized within the GGA+U functional are 5.3 eV on the d-orbitals of nickel, and 4.7 eV on the d-orbitals of zinc. This project utilizes the GGA functional of Perdew-Burke Ernzerhof, employing the Dudarev approach of utilizing an effective U parameter.

Planewave cutoff

The plane wave cutoff was determined using the convergence of formation energies of NiO and ZnO, defined as:

$$E_{formation} = E_{bulk} - \sum_{n}^{S} N_n * \mu_n \qquad 3\text{-}21$$

Where S is the atomic species in the material, N_n is the number of atoms of species n, and μ_n is the chemical potential of species n.

The chemical potential of the individual species is calculated as the total unit cell energy, divided by the number of atoms in the cell:

$$\mu_{Ni} = \frac{E_{Ni,bulk}}{N_{Ni}} \quad \text{3-22}$$

This is equivalent for all atomic species utilized:

$$\mu_{Zn} = \frac{E_{Zn,bulk}}{N_{Zn}} \quad \text{3-23}$$

$$\mu_{O} = \frac{E_{O,bulk}}{N_{O}} \quad \text{3-24}$$

The convergence cutoff requirement for the formation energy was

$$\frac{\Delta E_{rel}}{\Delta E_{cutoff}} \geq \frac{1\ meV}{50\ eV} \quad \text{3-25}$$

All calculations utilized a plane wave cutoff energy of 500 eV.

The k-points used a gamma-centered mesh for both NiO and ZnO, as both would be used within the same system for the interfaces. ZnO and NiO bulk energy for a minimal unit cell converged within 1 meV with meshes of 5x5x3 and 7x7x7, respectively. All supercell *k*-point meshes used the same density as a reference point. All interface and surface calculations use the density of the NiO bulk calculation, however only a single *k* point along the vacuum axis. GGA+U DOS calculations uses a mesh twice along all axes except the vacuum axis, which still uses a single k point.

PBE0

With the PBE0 hybrid functional, the NiO unit cell energy converges with a 4x4x4 gamma centered mesh, and the ZnO unit cell converges with a 5x5x3 mesh.

All hybrid calculations on supercells, mixed phases, surfaces and interfaces use a gamma point only mesh. This is a choice made due to hardware restrictions and is likely to introduce some error.

For all structures where both NiO and ZnO are present, the exact exchange fraction is set to the standard value of 25%. For each material separately, however, good agreement for the respective band gaps of the structures is obtained with fractions of 18.5% and 27.5%, respectively.

Surface Slabs

Within the scope of this project, only low Miller index surfaces of NiO and ZnO are considered. Hence, three surfaces of the NiO crystal structure, $\langle 100 \rangle$, $\langle 110 \rangle$ and $\langle 111 \rangle$, and four surfaces of the ZnO crystal structure, $\langle 0001 \rangle$, $\langle 000\frac{1}{2} \rangle$ $\langle 10\bar{1}0 \rangle$ and $\langle 11\bar{2}1 \rangle$ are included in this investigation.

The number of unit layers necessary for the surface energy to converge with respect to thickness are given in Table 3-1.

Table 3-1 Surface slab layer number: The required width of the slabs for energetic convergence with respect to thickness.

NiO	Number of layers	Number of Atoms
$\langle 100 \rangle$	6	96
$\langle 110 \rangle$	6	48
$\langle 111 \rangle$	6	48
ZnO	Number of layers	
$\langle 000\frac{1}{2} \rangle$	12	24
$\langle 0001 \rangle$	12	24
$\langle 10\bar{1}0 \rangle$	4	16
$\langle 11\bar{2}1 \rangle$	6	24

The $\langle 0001 \rangle$ and $\langle 000\frac{1}{2} \rangle$ surfaces are both c-axis polar terminations of the wurtzite structure, but rather than the termination ion, the terminology is here meant to refer to each of the two different termination ion arrangements: $\langle 0001 \rangle$ represents the relatively stable, physically observed polar termination, while $\langle 000\frac{1}{2} \rangle$ represents a much less stable, alternate termination.

All surface structures, as well as interface structures, have a vacuum layer of at least 20Å and have dipole corrections to both energy and electronic structure applied along the vacuum axis. For surface slabs within the interface structures that exhibited instability towards the vacuum surface, ionic relaxation is restricted in the ab-plane, allowing movement along the c-axis to allow the slab- and interface width to correctly adjust. The surfaces in question all exhibited relaxation only along the c-axis when relaxed in vacuum, so the interference with the interface structures is minor.

Interface Construction

Forming an optimal interface between two materials is a rather complex procedure. Even when simplified to the optimization of two static structures, the process is an optimization problem in a four-dimensional phase space: Three dimensions of relative space optimization, corresponding to relative movement along the x, y and z axes, as well as one relative rotational dimension in the ab-plane. Furthermore, complete optimization of any one of these parameters is a complex task in itself, so a simplified approach is assumed here.

Optimization of the relative rotations of the slabs is particularly complicated by the requirements of the surface calculation cell: Both structures must be fitted within the unit cell, lining up exactly with the cell walls. For any cell containing two or more mismatched structures like in a heterojunction, this almost always requires at least one of the surfaces to be strained into an appropriate fit. Either that, or the cell must be extended by adding further surface cells in the ab-plane. Both these options are problematic as the former would add the effects of changing strain to the calculated energies, while the latter would result in unfeasibly large supercells for certain rotation. Hence, in this project, only the relative displacements along the x, y and z axes are considered.

The energetically optimal interfaces were constructed through a multi-step process, to account for the instability of the magnetic structure of NiO. For images describing steps 3 and 4, see Figure 3-3.

1. The slab structures were constructed using the lattice parameters from prior calculations on the bulk material. The convergence of the surface energy with respect to slab thickness was within a cutoff of 1 meV per layer, or double layer depending on the surface.
    a. Spin polarized calculations were used in this step.
    b. One ZnO surface slab, the polar $\langle 000\frac{1}{2}\rangle$ surface, was excepted from this requirement, and instead considered converged due to the surface energy convergence having entered a constant cyclic behavior with respect to slab thickness. The lowest slab thickness with that followed this trend was selected for further calculations.
2. The initial interface structures were constructed in two sets, one with all strain placed on the ZnO slab, and one with all strain on the NiO slab. Two sets of interfaces were created from each of these: One with relaxed atomic positions, and one where the atomic positions were kept static. In the latter case, step 6 was not performed.
    a. A balance was struck between structure size and total strain within the system.
3. The respective surface slabs were first placed at fixed points along the c-axis of the interface unit cell. This distance was chosen to be slightly larger than the bond length of either material to avoid steric repulsion dominating the energy calculation. Structures forming a 4x4 grid of relative positions of the two slabs along the ab-plane perpendicular to the surfaces were created, and the energy of these structures without relaxation of atomic positions was calculated.
    a. The energy determination of the grid points utilized non-spin polarized calculations.
    b. The grid positions were all unique with respect to the repeating pattern of the crystalline materials, as the process of minimizing the strain on the structures of the surfaces required multiple unit cells in the ab-plane of one or more of the slabs. The selected grid positions did not account for symmetrically (and hence energetically) identical relative positions, however, as these were complex to distinguish beforehand with the strained and angled surface slab structures.

4. The most energetically favorable relative positions of the previous step were selected. While fixing the relative positions of the slabs in the ab-plane, the relative positions of the surface slabs were varied along the c-axis. The resulting energies were plotted, and the structures corresponding to the energetic minima positions were selected.
    a. The energy determination utilized non-spin polarized calculations.
    b. Before the next step, for interface structures that required it, the structures were expanded in the ab-plane to accommodate the magnetic structure of NiO.
5. A second optimization step was performed on the selected interfaces of the previous step: The atoms within the system were restrained such that they could only relax along the c-axis, and the structures were relaxed under these conditions.
    a. The structure relaxation utilized spin polarized calculations.
    b. The interface distance between the surfaces after the relaxation was retrieved, and the initial static structures were manually adjusted to have the same interface distance.
6. A complete ionic relaxation was performed on the resulting structures of the previous step, to obtain the final relaxed structures.
    a. The energy determination utilized non-spin polarized calculations.
    b. At this step, the interface of certain surfaces collapsed, indicating the interfaces were either energetically unfavorable, or unstable under the strain conditions and were hence removed from further calculations.

For the polar surfaces with two possible interface termination arrangements each, both are included as separate interfaces, with exception for the polar-polar interfaces. In this case, only the oppositely charged termination ion pairs are considered.

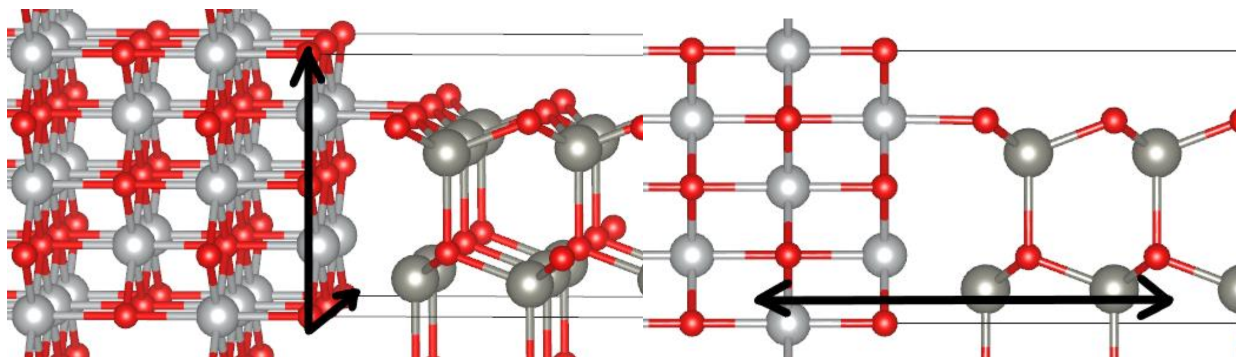

Figure 3-3 Left image: Step 3. Optimization of the relative ab-plane arrangement of the surfaces. The NiO structure is kept fixed, while the ZnO structure is aligned to different arrangements along the plane described by the black arrows. The arrangement with the lowest electronic energy is selected as the best interface position. Right image: Step 4. Optimization of the relative c-axis arrangement of the surfaces. The surface positions are varied along the direction of the black arrow, and the electronic energies of the arrangements are compared. The positions that give the lowest energy is selected as the best interface.

Mixed Phase Calculations

The calculations on the mixed phase systems utilize supercells of size 216 and 256 atoms formed from 3x3x6 and 4x4x2 supercells for the Ni:ZnO and Zn:NiO systems, both respectively. The NiO unit cell is not the one utilized for most bulk calculations in this study, but rather the space group 225 representation, comprised of eight atoms. It requires supercells of even dimensions to correctly represent the magnetic structure of NiO.

The ionic relaxation utilizes the PBE functional with the same energy cutoff as all other calculations, and the k-point density of NiO, scaled for the supercell size. Due to the similar ionic sizes of the Ni^{2+} and Zn^{2+} species, the mixed phases are assumed to be fully substitutional. The solute phase ions substitute the solvent phase ions entirely at random; however higher concentration supercells retain the swapped ions from the lower concentration calculations in the same lattice sites.

Electronic calculations are performed using the PBE0 functional.

4. Review of Relevant Literature

4.1. Nickel Oxide

Nickel has been claimed to form three different oxides: NiO, NiO_2 and Ni_2O_3[39]. In this case, the oxide of interest is the most well characterized of them, NiO.

Nickel oxide is a p-type wide band gap semiconductor with a direct band gap of 3.6 to 4.3 eV[2–5], depending on the literature consulted, and method of measurement. It is notable that single crystal measurements have reported band gaps located both at and near either extreme of this range. This band gap corresponds to an absorption of ultraviolet light and up, without interfering with light at visible wavelength. Stoichiometric nickel oxide is, despite this, a distinct green color, which are attributed to low oscillator strength d-d transitions[40]. NiO may contain non-stoichiometry in the form of cation vacancies compensated by electron holes. Highly non-stoichiometric NiO has a black appearance.

NiO assumes a rock-salt structure, where every ion is octahedrally coordinated with six oppositely charged ions. The structure has space group $Fm\bar{3}m$, and a structure parameter a=4.177 Å[41]. This representation is somewhat simplified, however, as NiO has a number of factors playing in on the detailed structure. In particular, the highly ordered magnetic structure nickel oxide assumes as a ground state, causes a slight rhombohedral distortion, equivalent to a contraction of 4*10^-3 Å along one of the <111> axes, per unit cell, at 9°C.[42] The effect is attributed to magnetostrictive effects[43]. Consequently, ground state NiO actually has a rhombohedral structure, with a cube angle of 90.1° at 0K[43]. The fully cubic structure has been determined to be completely assumed at a temperature of 433K, with the actual transition probably taking place in the region of 373-433K.[42]

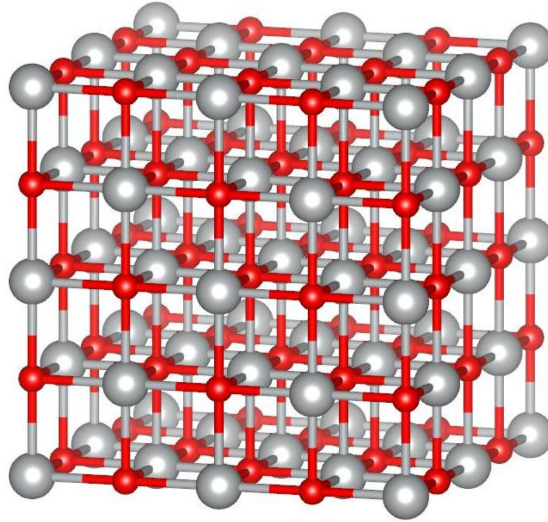

Figure 4-1 Structure of NiO. Nickel ions are represented by light gray spheres, oxygen by red spheres. The relative sizes of the spheres are arbitrary with respect to the specific system; The oxygen -2 ions have a greater ionic radius than the nickel 2+.

NiO is an anti-ferromagnetic material. In its ground state, neutron diffraction experiments determine the electron spins are arranged in parallel along the 111 planes.[44,45] The magnetic ordering does, however, not seem to have a significant effect on the valence band structure of the material.[46]

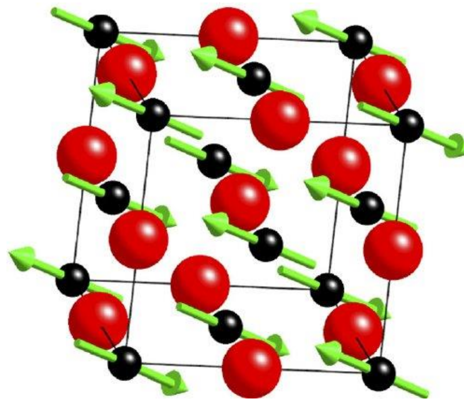

Figure 4-2 Antiferromagnetic structure of NiO. The black and red spheres represent nickel and oxygen, respectively. The green arrows represent spin alignment. Figure from reference [47].

NiO has three low-miller index surfaces:$\langle 100 \rangle$, $\langle 110 \rangle$ and $\langle 111 \rangle$. $\langle 100 \rangle$ is the surface that is the most commonly studied, likely due to being the most stable surface, and may be prepared either by thin film growth or cleavage of single crystal. The surface displays distinct (100) terraces, separated by monoatomic steps. The steps mainly run along the $[010]$ axis.[48] The $\langle 111 \rangle$ surface

would, in an ideal case, consist of only a single layer of oxygen or nitrogen ions, but this is relatively unstable, hence the surface will either rearrange itself, or adsorb atoms. Hydrogen and hydroxy groups are common candidates for the oxygen- and metal- terminated surfaces, respectively. Experimental evidence shows characteristic surfaces of octopolar reconstruction on the NiO $\langle 111 \rangle$ surface, upon removal of adsorbent groups by heating.[49]

In the production of pellets, NiO is a relatively difficult material to sinter, and is prone to assuming a relatively porous structure. Reported pellet densities after sintering range from 70% - 95% of the theoretical density.[50,51] The reported density ranges appear to increase with increased sintering temperature.

The intrinsic electronic p-type conductivity of NiO is due to metal vacancies within the crystal structure of the compound.[52] The p-type conductivity arises as the charge of these vacancies are compensated by electron holes in the valence band, representing an oxidized state in the Ni^{2+}-O^{2-} bonding orbitals. The form of this oxidation, whether it is most accurately represented as Ni^{3+} or O^{-} (Mott insulator and charge transfer, respectively), and the transport of the holes within the materials, whether it takes place either by a band-like or a small polaron hopping mechanism, are disputed properties of NiO.[50,53,54] Experimental evidence supports the presence of the doubly ionized nickel vacancy in pure NiO, in support of the Kröger-Vink defect reaction 2-22 providing a proper description of the physical system.[55]

The conductivity of pure NiO displays different characteristics, depending on the preparation of the sample, but a general trend is observed for single crystal measurements: All temperature dependent conductivity measurements exhibit thermally activated Arrhenius behavior. The unique point to note, is that there are two anomalous points where this dependency changes in a discontinuous manner. One is at the Neel temperature, and may be attributed to the rearrangement of the magnetic structure. The other is near 390K and has been argued to be caused by a small Jahn-Teller effect removing the spin degeneracy of the ground state.[42]

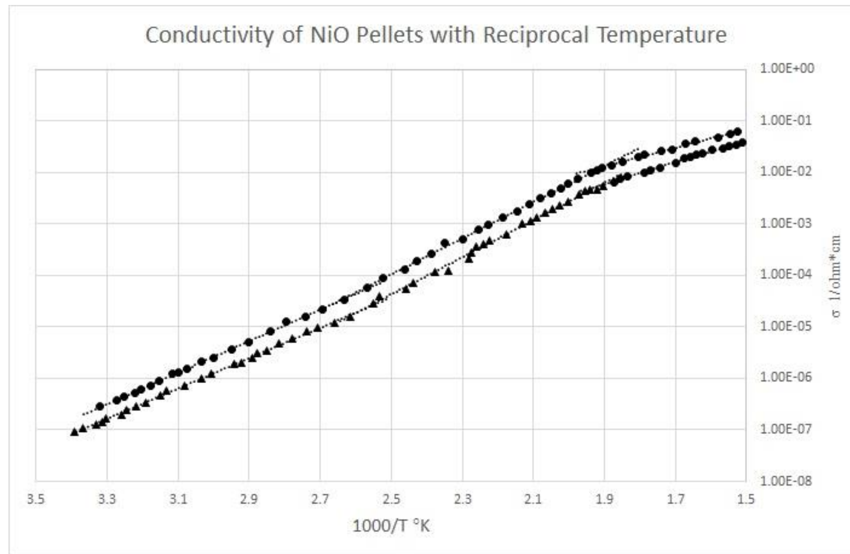

Figure 4-3 Plot of conductivity of NiO against reciprocal temperature. The circular datapoints represent measurements before annealing, and the triangular represent results after annealing. Figure reproduced from data in source [42]

NiO may be doped with lithium to increase the conductivity[50], increasing the concentration of electron holes within the material.[56] The doping lithium ions are reported to randomly substitute the nickel lattice sites without changing the crystal structure up to a concentration of 25%.[53] In accordance with equation 2-25, the solubility of lithium in NiO is dependent on the partial oxygen pressure, with certain sources reporting that, at low partial pressures of oxygen, 1.9% is the maximum concentration of lithium dopant before the segregation of a new phase occurs.[57] Equivalently with the nominally pure NiO material, the Kröger-Vink electron hole formation reaction of equation 2-25 upon doping with lithium, is also found to be supported by experimental evidence.[58]

At room temperature, the specific conductivity of pure NiO for a single crystal has been measured as 10^{-5} S cm^{-1}.[59] Lithium doping has been reported to increase this value to nearly 100 S cm^{-1} with optimal doping, albeit at a slightly higher temperature of 100°C, increasing to about 200 S cm^{-1} at about 900°C.[60] The addition of lithium dopant causes the conductivity of NiO to sharply increase for lower concentrations of lithium, but the effect of increased dopant concentration plateaus at around 2%, indicating this to be the ideal concentration.[56]

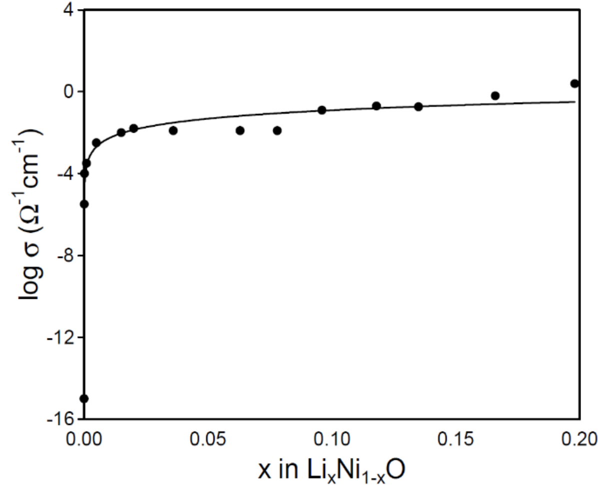

Figure 4-4 Conductivity of NiO with concentration of lithium dopant at room temperature. Figure from reference [61].

Doping of NiO with lithium ions has some effect on the size of the unit cell of NiO, with a 1.6% concentration of dopant resulting in a 0.043% reduction of the lattice parameter at room temperature.[57] The inclusion of lithium dopant does not appear to affect the magnetostrictive effects in NiO to a significant degree, as, for the measured dopant concentrations, the unit cell angle remained constant.[57] With respect to both structural and magnetostrictive effects, more significant alterations to the structure occurs at lithium concentrations near and above the random substitution solubility limits.[53]

There have been many computational studies on the properties of NiO. In later years, Density Functional Theory based methods have been the most prominent. At the same time, basic DFT functionals with approximate exchange-correlation potentials such as LDA (and LSDA) describe NiO rather badly, especially failing with respect to the electronic structure and the band gap. The cause of the failure has been claimed to occur due to the potentials badly describing the valence band of NiO.[62] In more recent studies, the functionals of choice are the DFT+U and hybrid functionals, such as PBE0 or HSE06.

In studies utilizing the GGA+U formalism, commonly utilized parameters for optimal electronic and magnetic structures are U=6.3 eV and J=1.0 eV. Commonly obtained parameters is an equilibrium lattice parameter of 4.19 Å, band gap and magnetic moment of 3.1 eV and 1.69 μ_B,

respectively.[63] Experimentally reported magnetic momenta are, for comparison, 1.64 to 1.90 μ_B showing good agreement.[64–66]

The surface energies of NiO vary significantly between the various cleavage planes. The calculated surface energies of the $\langle 100 \rangle$ and $\langle 110 \rangle$ surfaces are, respectively, 1.15 (Jm^{-2})[67] and 2.77 (Jm^{-2})[67]. In the case of the NiO $\langle 111 \rangle$ surface, a very thin film of four layers will have a rather high surface energy of 4.5 (Jm^{-2}), but reconstruction of the surface by what is referred to as octopolar reconstruction, may lower this value to 4.27 (Jm^{-2}).[49]

Band structure calculations of NiO have been performed in numbers, but the results do not completely agree. In particular, it may be noted that the band structure of NiO is sensitive to the exact choice of functional employed, displaying considerable changes in the structures, both qualitative and quantitative, between different methods/functionals.[68] DOS calculations show that the Ni-3d and O-2p orbitals mix near the top of the valence band, making NiO a mix of charge-transfer and Mott-Hubbard.[63] The Ni-3d orbital is, however, significantly enhanced over the O-2p, giving the band gap a character closer to Mott-Hubbard.[69]

4.2. Zinc Oxide

Zinc oxide is an intrinsic n-type semiconductor with a wide direct band gap of 3.37 eV, and a high exitonic binding energy of 60meV.[1] ZnO consequently absorbs light from the lower end of the ultraviolet spectrum, and is transparent to visible light. The exact physical and electronic properties of ZnO are notoriously sensitive to the methods of preparation, both for single crystal and pellets, to the extent the material is used as a test bed for investigation of physical phenomena generic to semiconductors in general.[70]

Under ambient conditions, ZnO has two stable crystal structures: A cubic zinc blende structure which is formed when ZnO is grown on a cubic lattice structure, or a wurtzite structure with space group $P6_3mc$ and structure parameters a=3.2497Å and c=5.2055Å.[71] Between the two forms, the wurtzite structure is the more stable due to filled 3d orbitals in Zn^{2+}, and is thus the

most common form.[5] The wurtzite structure and space group of ZnO lacks inversional symmetry, which results in ZnO having notable piezoelectric and pyroelectric properties.[72]

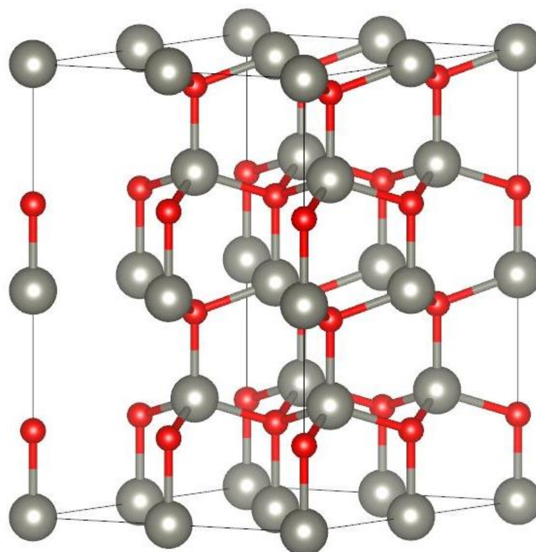

Figure 4-5 Structure of wurtzite ZnO. Zinc atoms represented by grey spheres, oxygen by red spheres. The relative sizes of the spheres are arbitrary with respect to the specific system; The O^{2-} ions have a greater ionic radius than the Zn^{2+}.

The binding between Zn and O within the crystal structure is highly ionic but has significant covalent contribution. The wurtzite structure places the charged Zn^{2+} and O^{2-} ions in individual planes, which would usually lead to the atoms restructuring themselves, but not in ZnO. The exact reason for this behavior does currently not have an explicit consensus.[72]

Wurtzite ZnO has four distinct low miller index surface planes, consisting of the two polar $\langle 0001 \rangle$-Zn and $\langle 0001 \rangle$-O termination surfaces, and the two nonpolar $\langle 10\bar{1}0 \rangle$ and $\langle 11\bar{2}0 \rangle$. The latter two are the natural cleavage planes due to requiring the lowest density of bonds to break.[73] Relaxation of the $\langle 10\bar{1}0 \rangle$ surface against a vacuum proceeds with the anion moving outwards and the cation moving inwards into a nearly planar sp^2 coordination.[74] The approximate bond lengths remain largely the same, but dangling bonds are changed to surface- and back-bonded states, lowering the energy and reactivity of the surface. Relaxation of the $\langle 11\bar{2}0 \rangle$ surface is more complex, involving anion-cation rotation, and a nonplanar puckering of the surface plane.

The behavior of these relaxations are characteristic of common II-VI and III-V binary compound semiconductors.[74]

The various surfaces in an experimental setting also display surface-dependent imperfections from ideal terraces.[75] The $\langle 0001 \rangle$ Zn-polar surface displays triangular islands, with pits of varying size. The triangular structure is considered suggest electrostatic stabilization of the surface that acts to cancel the surface polarity.[76] The islands are rotated 180° with respect to neighboring triangular terraces. The opposite O-polar surface rather displays flat hexagonal terraces that are separated by double layer steps but is without holes. The $\langle 0001 \rangle$ surface displays flat, rectangular terraces, separated by steps of a single atomic layer, perpendicular to the $[0001]$ and $[1\bar{2}10]$ vectors. Finally, the $\langle 11\bar{2}0 \rangle$ surface has terraces with atomic "stairs", building up and down a single layer at a time, along the $[0001]$ vector.[70]

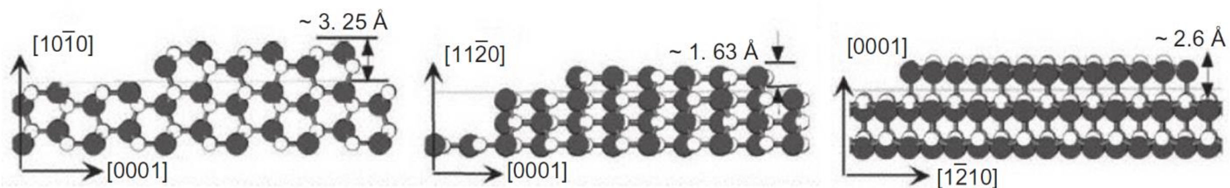

Figure 4-6 Termination structures of wurtzite ZnO, with experimentally observed rearrangements. The terminations are from left to right: $\langle 10\bar{1}0 \rangle$, $\langle 11\bar{2}0 \rangle$, $\langle 0001 \rangle$-Zn termination. The white spheres represent zinc ions, the grey represent oxygen. Figure adapted from reference [75].

As-grown ZnO is always n-type. The origin of this conductivity has been considerably disputed, due to the previously mentioned sensitivity of the material. Several possible causes, both intrinsic defects, including zinc interstitials[77,78], oxygen vacancies and zinc antisites[77], as well as extrinsic causes like impurities, have been investigated. All intrinsic causes are found to be unlikely for differing reasons. Among the extrinsic causes, hydrogen is likely the most extensively investigated possibility, as it is the most likely to contaminate any specific sample. While interstitial hydrogen is found to be too mobile to be retained at high temperature,[79] evidence suggests a possible cause to be hydrogen-substituted oxygen sites within the material, forming a shallow donor.[80] This species is only stable up to about 500°C, so it only constitutes a possible source of n-type conductivity below this limit.

The electrical conductivity of ZnO is relatively complex. In a single crystal, the uniaxial wurtzite structure results in anisotropic conductivity. The variance in the conductivity is, however, not too pronounced. A study found the conductivity to be isotropic to within the experimental uncertainty of 10%.[81] In both sintered compressed powder samples, as well as single crystal samples, the preparation method of the sample can affect not only the absolute conductivity, but also how the conductivity changes with temperature. For pellets, certain preparatory procedures may cause anomalous behavior such as reduced conductivity with higher temperatures.[82]

This instability of the properties of ZnO with preparation method, also apply to single crystal measurements. Variance of room temperature conductivity with preparation method has been observed to span six orders of magnitude.[83] The higher end conductivities obtained in this study were produced under oxygen poor conditions utilizing transport agents including hydrogen, in agreement with the previously noted possible cause of unintentional ZnO n-type conductivity.

ZnO may be doped with aluminum to improve the conductivity. The aluminum ions substitute the zinc lattice positions in an Al^{3+} oxidation state and introduce donor defects, increasing the charge carrier concentration within the material, according to 2-34. Undoped ZnO has a conductivity of about 0.1 S/cm at room temperatures, increasing to 25 S cm^{-1} around 1000°C. 2% Aluminum doped ZnO has, in comparison, a conductivity around 1000 S cm^{-1} at room temperature, decreasing to 400 S cm^{-1} at 1000°C.[84]

As noted previously, unintentional hydrogen doping is considered a possible cause for nominally undoped ZnO n-type conductivity. Alternatively, hydrogen dopants may be deliberately introduced to increase the free carrier density of the material. The most prevalent active forms of the hydrogen dopants are, however, found to be unstable against annealing above temperatures of 500°C.[85] Hydrogen doping may be used in conjunction with other dopants, such as aluminum. Depending on the method of preparation, optimal conductivity of ~2000 S cm^{-1} may be achieved for such multiple dopant materials at room temperature.[86–88] ZnO thin films doped only with aluminum in the same studies had a conductivity of ~100-400 S cm^{-1}.[87,88]

Lithium doping of ZnO has been investigated as a possible method of inducing p-type conductivity in ZnO. Lithium ions may behave as either donor or acceptor dopants in ZnO

depending on the sites occupied by the defect ions; they act as electron donors at interstitial sites, and electron acceptors at substitutional sites.[89] This trait inherently limits the p-type doping efficiency of lithium, yet p-type ZnO as a result of lithium doping has been reported.[90] These reports are rather controversial, due to issues of reliability and reproducibility.

GGA and GGA+U are common functionals for theoretical investigation on the electronic structures of wide band gap transition metal oxides. The GGA functional is, however, bad at predicting the band gap, significantly underestimating it. The GGA+U functional is used to correct for this shortcoming. Commonly often seen U parameters utilized to obtain correct band gap are 10 eV for the Zn-3d orbitals, and 7 eV for the O-2p orbitals.[91,92] These high potentials do, however, cause the structure parameters of the unit cell to be significantly underestimated. It should also be noted that there appears to be no universally applicable values of +U that work properly for ZnO, with a very large range of values reported utilized.[93] For the application of a $+U_{eff}$ parameter on only the Zn-3d orbitals, a value in the vicinity of 5 eV has been reported to give the best results, striking a balance of agreement for lattice parameters and other properties.[94] Other choices for functionals are hybrid functionals, such as PBE0 and HSE, which are commonly utilized for electronic structure calculations. There is little unity in what other basic calculation parameters are utilized, so the necessary values appear to vary considerably on a case to case basis, depending on the system of interest.

The surface energies of the various low-index ZnO surfaces have been investigated by computational means by both computational and experimental methods. With respect to the polar surfaces, the obtained values have been found to rely significantly on whether the surface is exposed to an oxygen rich- or poor environment. In the oxygen rich limit, reported values for relaxed surface energies of $\langle 0001 \rangle$-Zn and $\langle 000\overline{1} \rangle$-O are 2.39±0.0063 and 1.35±0.0063 J m^{-2}, respectively, from one source[95], and ~3.4 and ~1.1 J m^{-2}, from another.[96] The significant difference in values stems from the inherent difficulty in separating the contribution of the two termination interfaces from each other, as any cleavage forming this interface will necessarily form both of them. The reported coupled values for the surface energy show considerably more consistency, with reported values of 3.31[95] and ~3.4[97] J m^{-2}.

The surface energies of the nonpolar surfaces are considerably lower, reported to be 1.6 and 1.7 Jm^{-2} for the $\langle 10\bar{1}0 \rangle$ and $\langle 11\bar{2}0 \rangle$ surfaces, respectively.[97] It should be noted that these values display considerable dependence on the functional utilized.

Band structure calculations for ZnO performed with GGA+U are able to qualitatively reproduce the experimental trait of a direct band gap, which is found to be located at the gamma symmetry point. If the +U parameters are properly fitted, a correct band gap may also be obtained.[98]

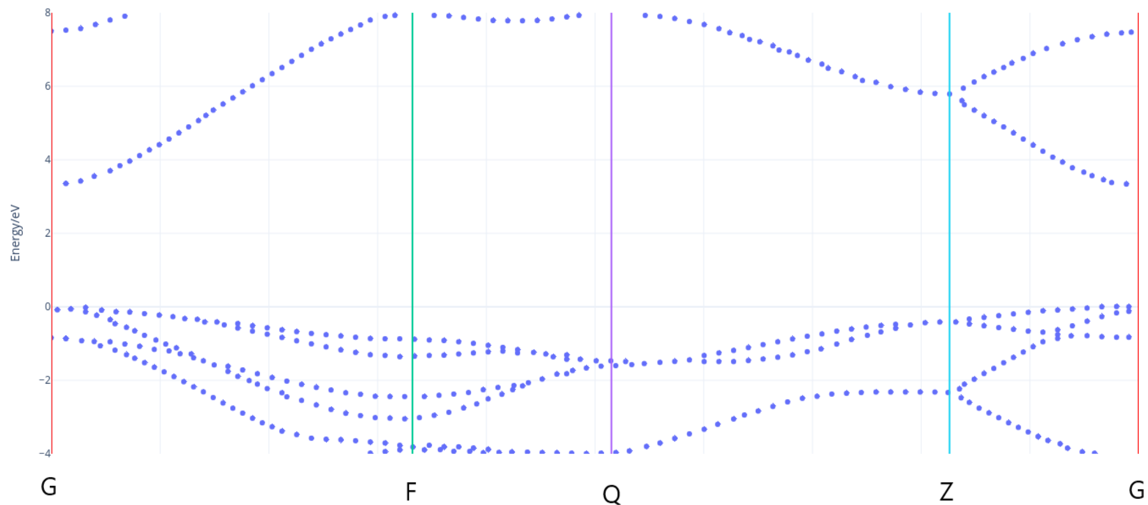

Figure 4-7 Band structure of ZnO, calculated by GGA+U. Data from source [98].

DOS calculations show the valence band maxima to be constructed predominantly from O-2p and Zn-3d orbitals, while the conduction band minima is constructed from Zn-4s orbitals.[98]

4.3. Nickel Oxide – Zinc Oxide Mixed Phase System

Mixing pure NiO and ZnO does not form a new product phase. The Ni^{2+} and Zn^{2+} ions have similar radii of 0.72 Å and 0.74 Å, respectively,[99,100] resulting in the ions inter-diffusing into each other's crystal structures. The crystal structures of the two materials are, however, dissimilar, resulting in a system of limited solubility of each ion in the opposite crystal. The

solubility limits for the formation of a single phase are somewhat uncertain, with different sources reporting different concentration limits and trend with temperature. The reported solubilities for the system at high temperature conditions of 800-1400°K to range from 1-7% nickel in ZnO, and ~27%-35% zinc in NiO.[101–104]

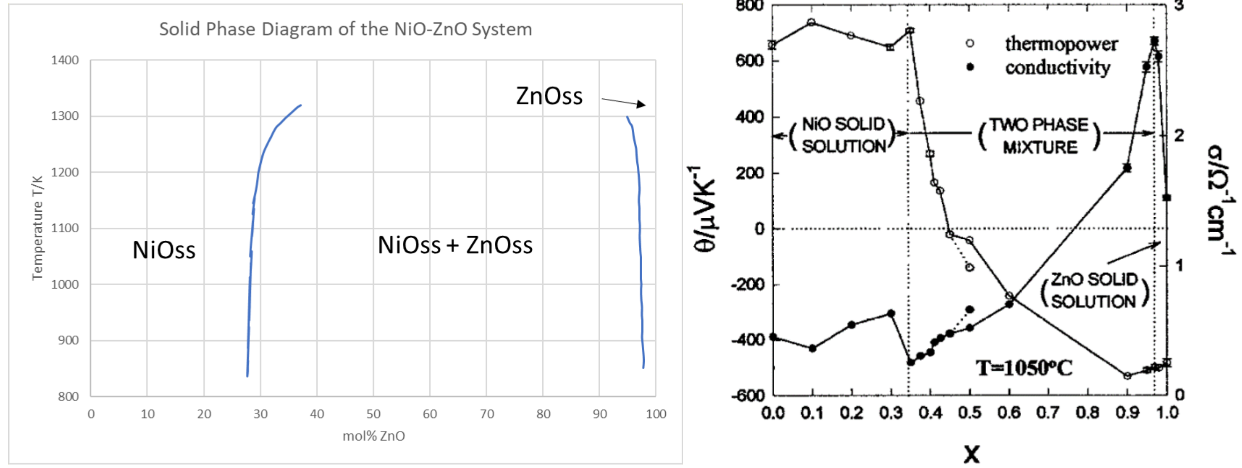

Figure 4-8 Left image: Phase diagram of the $Zn_xNi_{1-x}O$ system.[101] Right image: Conductivity and thermopower of the NiO-ZnO mixed phase materials at a temperature of 1050°C, with the composition of the ZnO material along the x axis. The dotted vertical lines represent the solubility limits.[102]

The mixed phase materials exhibit electronic properties that differ from the pure phase materials. The change in the conductivity with composition is plotted in Figure 4-8, right image. The conductivity of the ZnO_{SS} phase increases sharply with nickel content, peaking at the solubility limit of about 3%. The conductivity change of Zn:NiO is to a lesser extent, showing a non-linear change. At room temperature, the conductivity change is to a much greatest extent, spanning nearly nine orders of magnitude, increasing from NiO to ZnO along the composition axis.[102]

In experimental investigation of the Ni:ZnO system, the VBM level has been observed to increase in energy relative to the pure ZnO phase, accompanied by a decrease in the band gap width. While the band gap has been specifically reported to decrease, no exact value of the VBM level increase is known. The band gap effects are primarily reported for thin films and nanoparticles, which depend significantly on the construction. Reported band gap changes for approximately 5% nickel dopant cover a range of 0.04-0.30, with outliers at 1.25 eV.[105–109] The results depend on the preparation, the values A Ni:ZnO-ZnO heterojunction has been reported to exhibit a VBO of 0.32 eV.[110] The effects of the doping on the lattice parameters on ZnO have

only been reported for nanostructures and is likely affected by the particle size, as there is no agreement between studies. Increase, decrease and no change in lattice parameters with nickel concentrations have all been reported.[105,111,112]

A theory that experimental studies use to describe the narrowing of the band gap of ZnO with nickel doping, is a d-orbital splitting model, where magnetic impurity d-orbital states are split, resulting in a high-spin arrangement of the electrons, with the bands arranged as described in Figure 4-9 (left image). One study indicates this effect only appears at around 2% concentration of nickel, as shown in Figure 4-9 (right image), with a separate doping effect occurring at 1% concentration.[113]

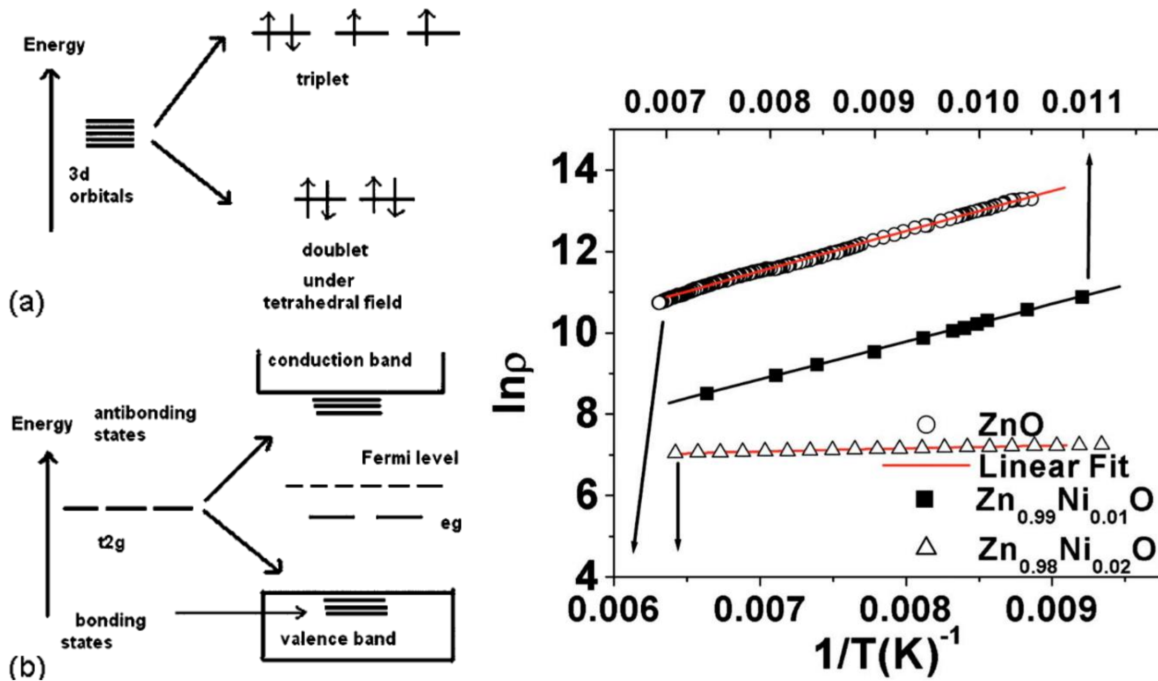

Figure 4-9 Left image: A diagram describing the d-orbital splitting model to describe reduced band gap effect in transition-metal doped wurtzite structure. Right image: Resistivity of nickel doped ZnO vs. inverse temperature. Figure from reference [113].

The effect of incorporation of nickel ions into the ZnO structure with respect to magnetic properties is somewhat unclear. The majority of studies are on nanostructures of the mixed phase compounds, so particle size might have a significant effect, however both ferromagnetic and paramagnetic behavior has been reported.[114,115] The ferromagnetic properties have been suggested to arise both as a property of the Ni:ZnO material or as a consequence of nickel-

oxygen vacancy interactions.[114,115] Antiferromagnetic interactions between the nickel ions have been observed to suppress the ferromagnetic properties as well.[116]

For the Zn:NiO mixed phase structure, the lattice parameter of NiO in bulk material has been reported to increase slightly with concentration of zinc ions, by about 0.03 Å, or by about 0.7% on the NiO lattice parameter, at 30% zinc ion doping, following a generally linear trend.[117] While separate studies disagree on the quantitative degree, the band gap of Zn:NiO is observed to decrease with zinc ion concentration.[118,119]

For the native magnetic structure of NiO, neutron diffraction experiments have shown the antiferromagnetic structure of NiO to remain upon the formation of the Zn:NiO system. At the 0K limit, at 30% zinc ion concentration, the magnitude of the magnetic moments of the nickel ions is observed to decrease by about 4-5%.[120]

For a system of doped polycrystalline NiO and ZnO, a heterojunction composed of $Li_{0.02}Ni_{0.98}O$ and $Al_{0.02}Zn_{0.98}O$ (the compounds will henceforth be referred to as Li:NiO and Al:ZnO), the rates of interdiffusion of atoms and dopants have been investigated for high temperature environments.[121]

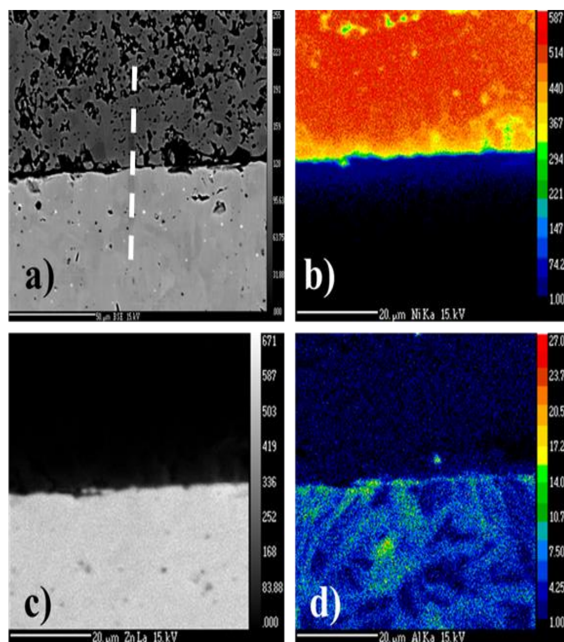

Figure 4-10 Interdiffusion over a Li:NiO (top) - Al:ZnO (bottom) junction. a) Scanning Electron Microscopy image of the junction. b) Concentration of Ni2+ ions, c) Concentration of Zn2+ ions. d) Concentration of Al3+ ions.

Ni^{2+} is shown to diffuse into Al:ZnO with an essentially uniform inter-diffusion zone, while Zn^{2+} diffuses a considerably shorter distance into the Li:NiO in the same period of time. Diffusion of the dopants into the opposite materials was found to be nearly undetectable for Al^{3+}, despite the concentration being significantly lower than the solubility limit.[122] The reason for Ni^{2+} relatively rapid rate of interdiffusion is due to its diffusive process being dominated by enhanced grain boundary diffusion by orders of magnitude, relative to bulk diffusion. Zn^{2+} does not exhibit this behavior, rendering the interdiffusion of Ni^{2+} the limiting factor to the lifetime of a Li:NiO-Al:ZnO heterojunction.[121]

In doping of NiO with zinc, the zinc ions randomly substitute cationic sites within the crystal structure, assuming the rock salt structure of NiO, which is an unusual configuration for Zn^{2+} ions.[5] Increasing the zinc ion concentration causes the structure parameter of the mixed phase NiO to change linearly towards the structure parameters of ZnO, in accordance with Vegard's law.[5] The band gap of the mixed phase changes in a similar manner. NiO and ZnO remain as p- and n-type semiconductors up to the saturation concentration of the other metal ion for bulk material.[102]

4.4. Properties of the Li:NiO-Al:ZnO p-n Junction

Theoretically, the Li:NiO-Al:ZnO p-n heterojunction has a built-in potential of 0.80 eV[123,124] from the difference in the doped materials' work functions. Good agreement is achieved with experimental observations, which places the value at 0.90±0.10 eV.[121] The heterojunction is rectifying at lower temperatures of 500°C, but this property is gradually lost with increasing temperature. At 1000°C, it is for practical purposes entirely lost.[121]

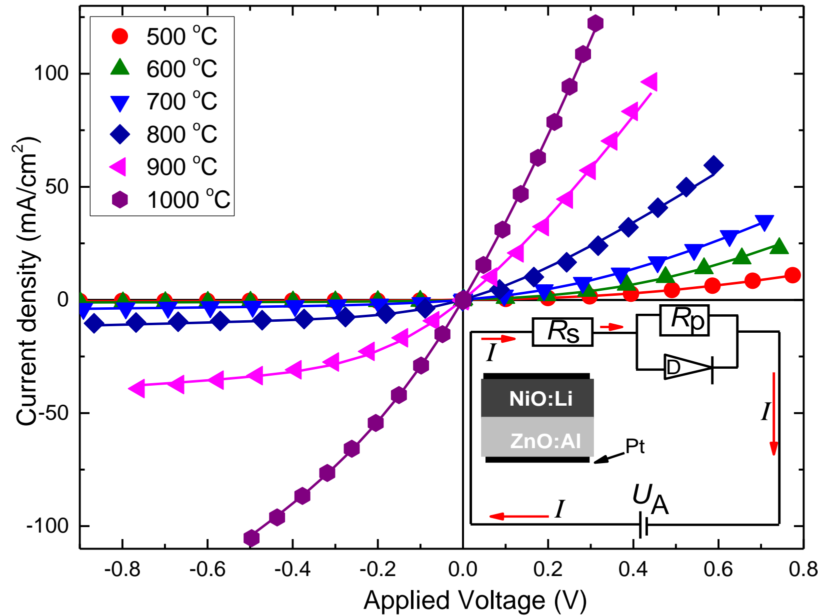

Figure 4-11 I-UA characteristics of the Li:NiO-Al:ZnO heterojunction across a temperature range of 500-1000 °C. The solid lines represent fitted lines. The lower right schematic shows a circuit equivalent to what is utilized in the measurements.[125]

In undoped materials, the experimentally reported work functions of NiO and ZnO cover a considerable range. NiO typically exhibits values of 5.0-5.6 eV, reaching 6.7 eV with special preparation.[126–129] A commonly used value is 5.4 eV, around the center of the reported range. The work function of ZnO exhibits considerable variance with preparation and termination surface, with reported values covering a range of 3.7-5.05 eV, with an outlier value at 6.0 eV.[130–132] It should be noted that, depending on the temperature employed in the preparation of the surfaces, the differences between the individual surfaces may change considerably. Form the range of the work function values, the possible theoretical built-in potentials consequently cover a range from 3.0 eV to -1.0 eV.

In experiments with thin films, one study has claimed the band alignment over the heterojunction interface is dependent on the orientation of the ZnO. The most significant effect was observed in the potential difference of the conduction and valence bands of the two materials: The bands were found to lie ~0.3eV closer with a junction across the polar surface, compared to the nonpolar.[61] Separate studies of NiO-ZnO heterojunction band offsets have been performed, reporting values of 1.3 eV[6], 1.47 eV[133] and 1.50 eV[134], with outlier values of VBO of 2.6 eV[7] for the similar heterojunctions. The surface orientations in the studies with similar values reported

polar-polar interfaces in all cases. The observed effects of the interface on the respective energy levels, as well as the bulk material properties, produce different values. The most likely possibility is that the interface VBO is significantly dependent on the surface conditions.

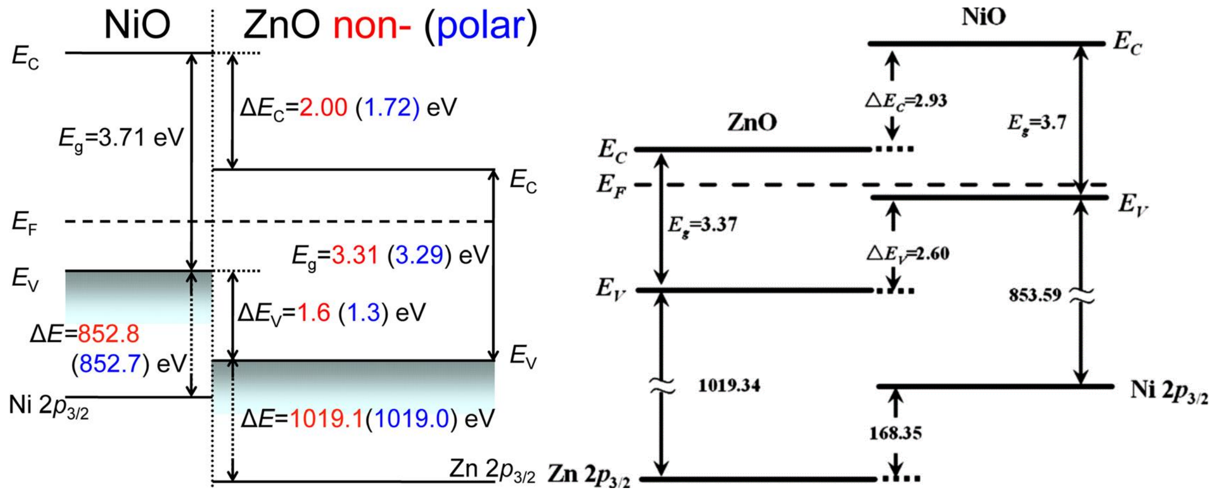

Figure 4-12 Left Image: Schematic energy band alignment of NiO(111)/ZnO(1120) (nonpolar) and NiO(111)/ZnO(0002) (polar).[121] Right Image: Schematic energy band alignment of NiO(111)/ZnO(Unknown alignment).[7]

In experiments with deposition of NiO on thin films of ZnO, the NiO was found to preferentially arrange itself with a $\langle 111 \rangle$ orientation regardless of the ZnO surface it was deposited onto. The in-plane lattice mismatch of the $\langle 111 \rangle$ plane of NiO with the $\langle 11\overline{2}0 \rangle$ and $\langle 0001 \rangle$ planes of ZnO has been calculated to be 13.7% and -8.7%, respectively.[6]

Heterojunctions incorporating ZnO as the n-type material have been explored with several other materials, such as Cu_2O[135–138], CuO[139,140], CuI[141], $BiFeO_3$[142], Ga_2O_3[143] and In_2O_3[144] as examples. The full list is more extensive, owing to the favorable properties of ZnO as an n-type metal oxide material. A heterojunction of particular interest is the GaN-ZnO system, due to its properties as a LED with peak emission in the violet-blue region of the spectrum.[145]

5.Results and Discussion

5.1. Bulk Parameters

By the nature of modern DFT, the methodology does not provide all physical parameters directly. Many properties must be calculated as relative values, between two or more different calculations. Consequently, obtaining a baseline for comparison with later calculations is necessary, and the properties of the bulk materials of interest is a natural place to start.

NiO and ZnO are notoriously difficult materials to model correctly within a DFT formalism. To obtain an adequate description, even extremely high-level theory such as GW is not necessarily enough. Such calculations are only feasible for unit cell sized systems and cannot be utilized for surface calculations. In this case, GGA+U and hybrid functionals are utilized, despite the known inadequacies.

5.1.1. Bulk NiO

The parameters obtained for a bulk NiO unit cell with both the GGA+U and PBE0 functionals are given in Table 5-1.

Table 5-1 Basic parameters obtained for bulk NiO calculations.

Functional	Lattice parameter (Å)		Band Gap (eV)	Band Gap Transition	Ni Magnetic Moment (μ)
GGA+U	a=b=c	4.200	3.03	L-G	1.71
PBE0: 18.5%	a=b=c	4.171	3.82	L-S	1.64
PBE0: 25%	a=b=c	4.166	5.02	L-S	1.68
Experimental	a=b=c	4.178	3.6-4.3	Direct	1.64-1.90

The GGA+U functional overestimates the lattice parameters of the NiO structure but still produces a reasonable result. The band gap, however, is significantly underestimated by nearly one eV. The nature of the band gap transition is also wrongly predicted to be indirect in nature, with a transition from the L to the Gamma point, see Figure 5-2. The calculated magnetic moment shows good agreement with experimentally determined values. Computational results from literature with the same parameters give a lower value, corresponding to the value obtained in this study if the non-spherical contributions to the gradient of the electron density in the PAW pseudo-potentials are excluded from the calculation.

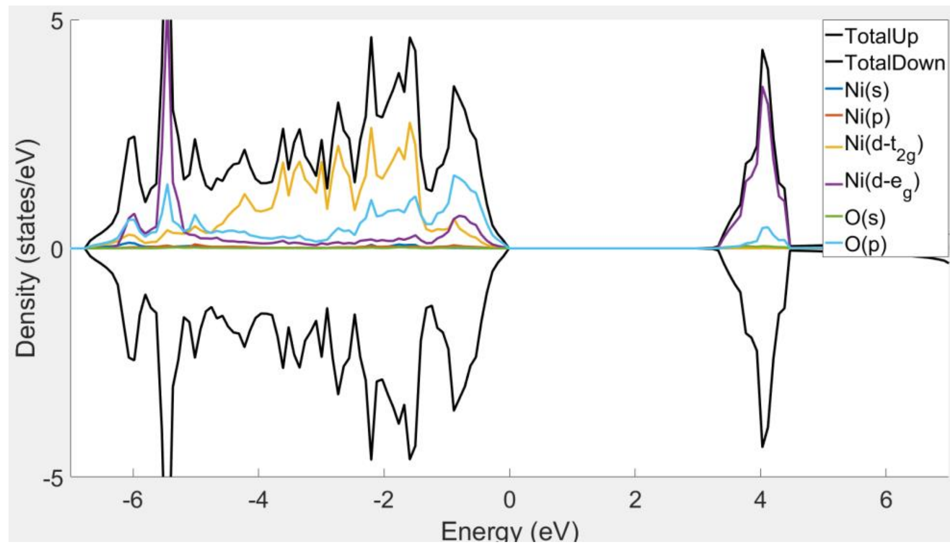

Figure 5-1 Species and orbital decomposed DOS of NiO, calculated with GGA+U.

From the GGA+U DOS structure, decomposed by species and orbital, the valence band edge is predominantly composed of O-2p orbitals, but it is mixed with Ni-3d orbitals of both, producing the mixed charge transfer, Mott-Hubbard transition obtained by prior studies.[63,69] The conduction band edge is predicted to be constructed from mixed Ni-4s orbitals and O-2s orbitals in roughly equal proportion. The Ni-3d states dominate the conduction band slightly higher in energy past the edge, however.

The hybrid calculations give the same composition for the valence band; however, the composition of the conduction band differs. The character is predicted to be nearly only of the Ni-3d states, with only minor components of the Ni-4s and O-2s. It should be noted that the CBM energy location in k-space has changed compared to the GGA+U. Comparing the CBM

compositions at the same symmetry transition point shows the hybrid functional still predicts the CBM edge to be composed from Ni-3d states. The O-2p, O-2s and Ni-4s enter at a slightly higher energy.

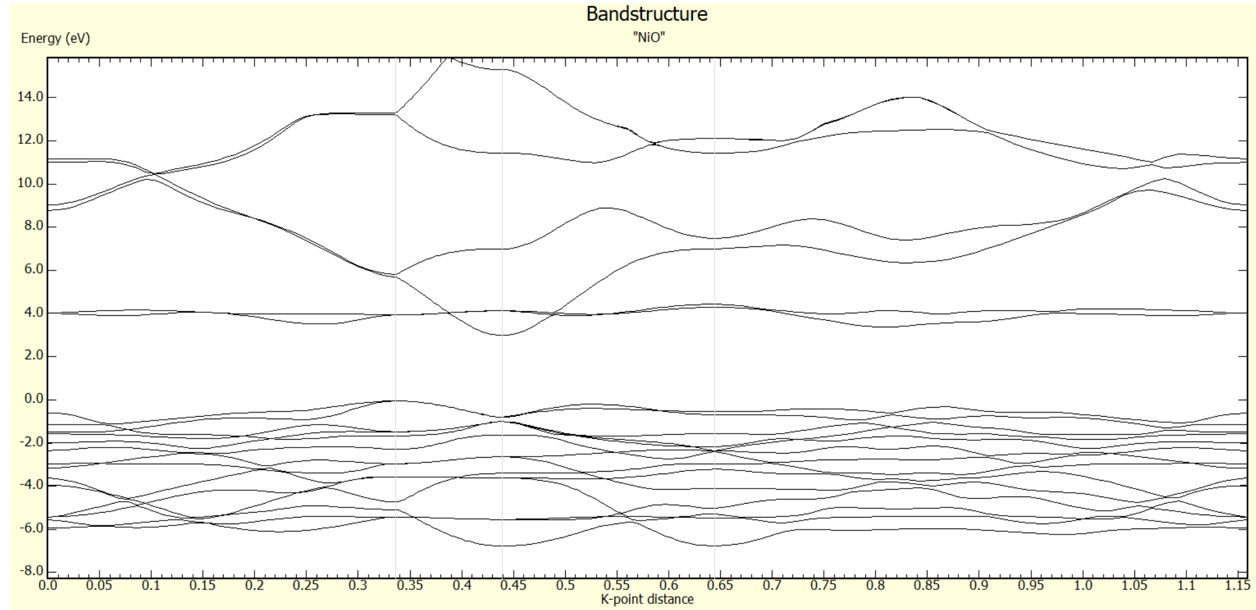

Figure 5-2 Band structure of NiO, calculated with GGA+U. The symmetry path is W-L-GM-X-W

The band gap of NiO is, contrary to experimental evidence, predicted to be an indirect transition from the L to Gamma symmetry points. The VBM is composed by two degenerate bands (four with spin), where curvature differs between the W-L and L-GM directions. Consequently, the effective masses of charge carrier holes will be slightly anisotropic.

The experimental magnetostrictive effects on the structure are also observed, although the magnitude is underestimated: The cubic angle of a perfect rock salt structure is distorted by about 0.5 degrees from a cubic arrangement, compared with the 1 degree of distortion at 0K expected from extrapolating experimental evidence.[43]

The PBE0 functional with 18.5% exchange fraction improves the lattice parameter, underestimating it slightly. The obtained band gap is in the region of experimental values, but the nature of the band gap has changed from the GGA+U result and is predicted to be an indirect L-S transition band gap, where S is a point along a symmetry line between the Gamma and K

symmetry points. The obtained magnetic moment shows good agreement with experimental evidence, agreeing with the experimental range.[64–66]

The PBE0 functional with a standard exact exchange fraction performs worse than the adjusted version with respect to most parameters. The underestimation of the lattice parameters has increased, but the resulting structure is still more accurate than the GGA+U results. The band gap is overestimated by about 1.3 eV. The standard exact exchange thus overestimates the band gap more than the GGA+U functional underestimates it. The obtained magnetic moment is still at an acceptable value, within the experimental range.

Effective Charge Carrier Mass

Within a material such as a semiconductor, electrons do not necessarily behave as though it possesses the same mass as it would in a vacuum. The same applies to electron holes, and determining these values, and the ratio between them, provides information on the properties of the material. In particular, the effective mass is a determining factor in the movement of charge carriers between the valence and conduction bands and play a role in determining the intrinsic Fermi level.

The band structure of NiO has previously been noted to not describe experimental results properly, as the band gap transition is of the wrong nature. As the effective mass values are calculated from the band structure at these points, the obtained values must be taken with caution. The effective masses of NiO are given in Table 5-2:

Table 5-2 Effective charge carrier masses for NiO. All units are given in terms of electron masses m_0. The mass subscript represents the symmetry path, the superscripts mean electron (n), heavy hole (hh), light hole (lh), and hole (h). The latter means there are no degenerate bands with different curvature on the subscript symmetry path.

	m_{W-L}^{hh}	m_{W-L}^{lh}	m_{GM-L}^{h}	m_{X-GM}^{n}	m_{L-GM}^{n}
Calculated	1.79	0.51	1.24	0.29	0.30
Literature Calc	1.66[146]	0.55[146]	0.86[146]		
Experimental	0.80 – 1.00[147]				

The harmonic mean of the calculated effective hole masses shows excellent agreement with experimental evidence for NiO, albeit under high temperature conditions, giving a value for the effective hole mass of $0.90m_0$. The effective hole masses display anisotropy between the $W - L$ and $GM - L$ directions, while the electron masses are near equal. The effect of the anisotropy in a physical system is diminished by the light and heavy holes both contributing to conduction along the $W - L$ direction. As NiO is a p-type semiconductor, however, this anisotropy might affect the properties of certain interface alignments for junctions.

The overall agreement between the calculated and experimental effective hole masses could be considered evidence to the GGA+U valence band maximum being correctly located, although not conclusive. If it was correct, however, the low electron effective masses would originate from the wrong CBM band. The low magnitude of these values would indicate an intrinsic n-type behavior of the NiO Fermi level with temperature, contrasting observed p-type behavior.

5.1.2. Bulk ZnO

The parameters obtained for the bulk ZnO calculations are given in Table 5-3:

Table 5-3 Basic parameters for bulk ZnO calculations.

Functional	Lattice parameter (Å)		Band Gap	Band Gap Transition
GGA+U	a=b/c	3.237/5.198	1.43	G-G
PBE0: 27.5%	a=b/c	3.261/5.213	3.43	G-G
PBE0: 25%	a=b/c	3.258/5.215	3.11	G-G
Experimental	a=b/c	3.2497/5.2055	3.37	Direct

The GGA+U functional gives excellent agreement with experimental values for the lattice parameters. The band gap is underestimated significantly, with the predicted value about 42% of the experimental value.[1] The hybrid calculations perform worse with respect to the lattice parameters, but the results still agree with the experimental range. With respect to the band gap, the hybrid functionals perform better than the GGA+U functional, for either specifically chosen,

or standard exact exchange fraction. The prediction of a direct band gap in both cases is also in accordance with experimental results.[1]

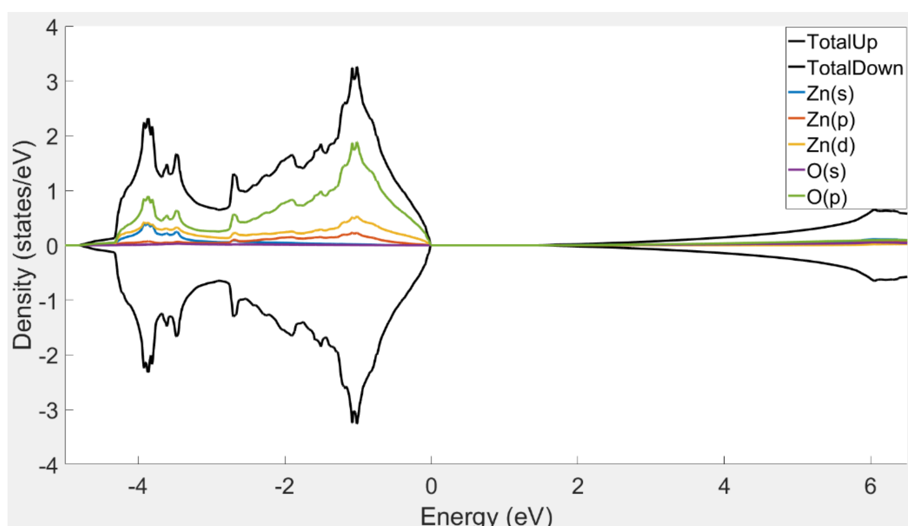

Figure 5-3 Species and orbital decomposed DOS of bulk ZnO from GGA+U.

As may be seen from the figure, in GGA+U, the valence band edge of ZnO is predicted to be partially formed of both zinc and oxygen states, but the O-2p orbital states dominate the structure overall, predicting a partly covalent nature of the bonding. The conduction band is predicted to be about equally composed of Zn-4s and O-2s states, with the Zn-4s states arising at a slightly lower energy than the latter, in accordance with prior computational results.[98] The hybrid DOS predicts a similar result, except the band gap error of GGA+U.

The GGA+U band structure of ZnO is shown in Figure 5-4:

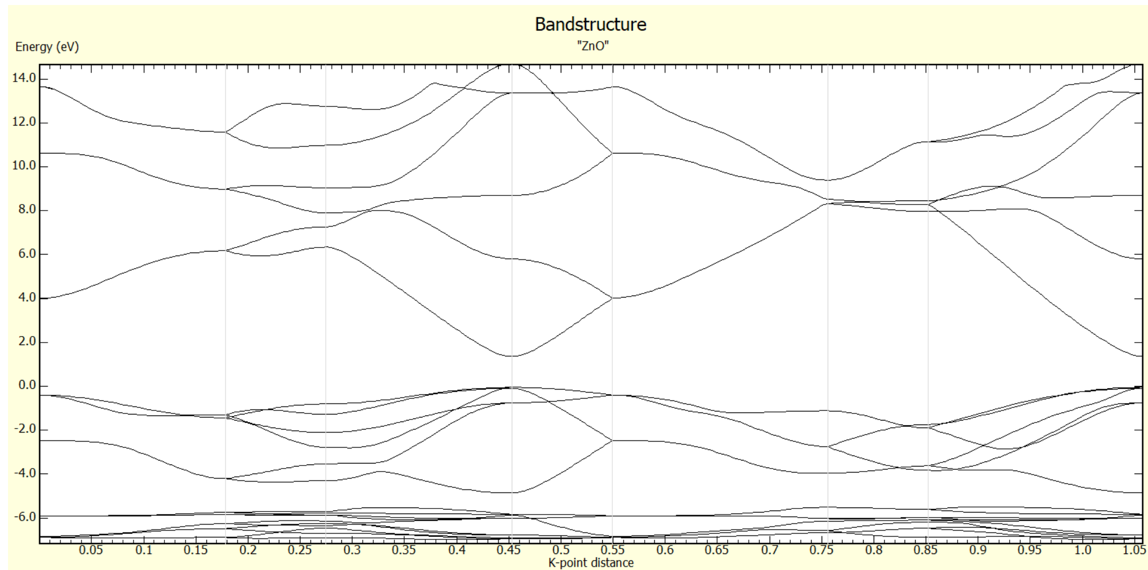

Figure 5-4 Band structure of ZnO, calculated with GGA+U. The symmetry path is A-L-M-GM-A-H-K-GM.

The band gap is shown to be direct in nature, occurring at the gamma point. There are several bands close in energy to the VBM band, that have a relatively sharp curvature comparatively. Holes formed within these lower energy bands would have a lower effective mass than holes in the higher valence band. The obtained structure closely matches previous calculations. Comparison with HSE functional band structure indicates the GGA+U band shapes are approximately correct, although the band gap is underestimated.[148]

Effective Charge Carrier Mass

The effective masses of ZnO are given in Table 5-4:

Table 5-4 Effective charge carrier masses for ZnO. All units are given in terms of electron masses m_0. All values are derived according to the methodology described in the calculation section, except the m^{lh}_{M-GM} value. The band structure around the k=0 point displays abrupt change, not permitting enough data points for a sixth-degree polynomial fitting. A second-degree fitting is used instead. The mass subscript represents the symmetry path, the superscripts mean electron (n), heavy hole (hh), light hole (lh), and hole (h). The latter means there are no degenerate bands with different curvature on the subscript symmetry path.

	$m^{hh}_{M-GM\perp}$	$m^{lh}_{M-GM\perp}$	$m^{h}_{A-GM\parallel}$	$m^{hh}_{K-GM\perp}$	$m^{lh}_{K-GM\perp}$	$m^{n}_{M-GM\perp}$	$m^{n}_{A-GM\parallel}$	$m^{n}_{K-GM\perp}$
Calculated	2.90	0.24	3.32	2.90	0.24	0.19	0.20	0.19
Literature Calc	0.35-0.63[149]	0.23-0.63[149]	3.23[149]			0.13 - 0.25[146,149]	0.14-0.30[146,149]	0.13-0.25[146,149]
	2.90[150]							
Experimental	0.45-0.59[151,152]					0.21 – 0.29[149,151,153,154]		

The calculated effective electron masses underestimate the experimentally observed range but shows overall good agreement. The calculated masses show anisotropy between the perpendicular and parallel values, relative to the c-axis, but the difference is minor. Literature results vary somewhat, however, on which of the two axes exhibits the lower or higher effective mass.

The calculated hole masses show good agreement with previous calculations, depending on the source, although there is considerable difference between the obtained results. The results individually appear to either over- or underestimate the experimental hole masses. The harmonic mean of the calculated values provides better agreement, with a value of $0.54m_0$. The two sets of perpendicular mass values display no anisotropy between each other, but between the perpendicular and parallel masses, there is considerable difference, same as with the electron masses.

Final Considerations for Bulk Parameters

The obtained parameters and properties of the NiO and ZnO bulk materials, display significant divergence from the experimental values. This is partly because experimental measurements occur at finite temperature conditions, while DFT is a 0K methodology. However, as mentioned in the introduction of the bulk parameter section, both NiO and ZnO are materials that are not well described by neither GGA+U or hybrid functionals. Consequently, a considerable degree of error is to be expected. In this specific case, the main discrepancies are the band gaps, and the nature of these transitions. Both are significantly underestimated, and since band gaps decrease with temperature, this is fully due to the error within the chosen level of theory. For NiO, the transition of the band gap is also wrongly predicted, with different, both in disagreement with experimental evidence, transitions for each functional, indicating that not just the band gap, but also the relative positioning of the valence and conduction bands with respect to energy are not correctly predicted either. The calculation of effective masses for both materials, do show agreement between the calculated and experimental values, indicating the shape of the bands are well predicted.

The results obtained with this level of theory are consequently subject to a considerable margin of uncertainty and error, but GGA+U and hybrid DFT is also the limit of what may be utilized for the system sizes that are necessitated for calculations in this study.

5.2. NiO-ZnO Mixed Phase

The goal of the greater project of which this thesis is part of, is the feasibility of constructing a p-n junction which is thermodynamically stable with respect to interdiffusion, by utilizing equilibrium concentration mixed phase semiconductors. Such mixed phase semiconductors would exhibit different electronic properties, compared to the pure materials. As the equilibrium concentrations vary somewhat with the intended operational temperature range, the properties of the junction would exhibit a degree of variance with the specific conditions. The properties of the mixed phase materials are thus investigated in this section.

5.2.1. Nickel Dissolved in ZnO (Ni:ZnO)

Structural Analysis

In the limit of low concentrations (0.9%), the effect of nickel substitution of zinc ions is minor. The bond lengths of the wurtzite coordinated nickel ion are about 4.2% longer compared to the bonds of pure wurtzite ZnO for the bond parallel to the c-axis, and about 1.8% longer for the bonds nearly parallel to the ab-plane. The nickel ion distorts the angles of its planar direct bonds, reducing the angle between them and the ab-plane by about 1.9°.

Despite the expansive distortion caused by the nickel ions, the total volume of the mixed supercell displays a small reduction of about 0.1%. The reduction of the volume occurs due to the c-axis bonds of Zn-O pairs surrounding the nickel impurity contracting and shortening in response to the presence of the nickel ion. The a- and b- lattice parameters are both extended slightly, but the contraction along the c-axis dominates the volume change.

Past the lower limit concentration, the volume of the structure will increase with concentration of nickel ions. At the limit concentration for the temperature range under consideration, 5.5%, the total volume is still smaller than that of a pure ZnO structure. The original angles of the ZnO unit cell structure are also displaying distortions, albeit on the order of less than 0.1° from the ideal angle.

Thermodynamic Analysis

At the limit of low concentration, the total internal energy of the system increases with the addition of the nickel ions, indicating the mixing process to be endothermic, and consequently driven by entropy. At higher concentrations than this initial increase, however, the trend reverses, and the energy decreases with concentration, indicating the process to be exothermic instead. This trend continues past the experimental solubility limit, to the limit of complete substitution.

Electronic Structure Analysis

The electronic structure of the Ni:ZnO mixed phase is somewhat complex to ascertain, as the introduced nickel ions are predicted to retain their magnetic properties in the new environment. Hence structures with an odd number of nickel ions exhibit a considerable difference in the energy levels between up- and down-spin states, complicating the results. Due to the small solubility range of the Ni:ZnO system, only the DOS structures of the ~1.8%, ~3.7% and ~5.6% concentration nickel ion systems are considered here, along with the pure ZnO system for reference. The relative band edge levels are shown in Figure 5-5.

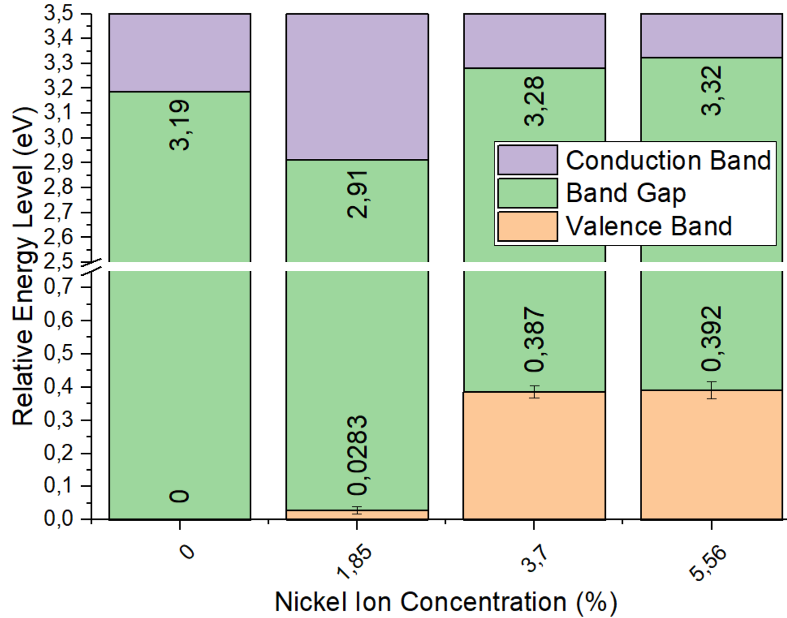

Figure 5-5 Relative band edge levels of ZnO with concentration of nickel ions. Energy scale of VBM values relative to the band edge of pure NiO, calibrated against the average 1s orbital energy of zinc. The error bars represent the standard deviation of the reference core level energies.

At lower concentrations of 1.8% nickel ions, the VBM level lies about 0.018 eV above the bulk ZnO value, and the band gap is narrower by about 0.3 eV. The decrease of the band gap agrees with the higher range of experimental results, and while there are differing results, saturation of the band gap change around 2% has been experimentally reported.[155,156] The VBM edge composition mostly matches that of bulk ZnO, although Ni-3d states are mixed in, in a much smaller ratio. The increase in the VBM level at this low concentration is of a different nature compared to higher concentrations, likely caused by the decrease in the system volume. The limit concentration VBM increase of 0.39 eV overestimates the band gap reduction, but is in agreement with the experimental attribution of the band gap reduction to shallow acceptor states.[110] The occurrence of the band gap reduction and VBM increase at separate concentrations, however, is against this assumption.

Contrary to expectation, nickel ions are predicted to act as electron donors in Ni:ZnO, for low nickel concentrations at and below 2.8%. For these low concentration states, the electrons in the conduction band originate from the valence band nickel 3d-orbitals, one from each nickel ion.

The nickel electrons assume a high spin arrangement, with a magnetic moment of 2.56 μ_B. In terms of defect chemistry, the system may be described by the equation

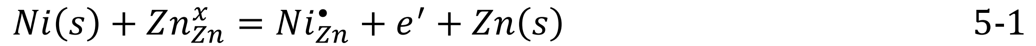

$$Ni(s) + Zn_{Zn}^{x} = Ni_{Zn}^{\bullet} + e' + Zn(s) \quad 5\text{-}1$$

where the $Ni_{Zn}^{\bullet}$ species assumes a high-spin electron configuration. The spin arrangement of the mixed phase Ni:ZnO follows a consistent trend with concentration: ~0.9% to ~2.8% concentration assumes the high-spin arrangement, and nickel is predicted to act as an electron donor. At 3.7%, the regular spin states of nickel are assumed, and the donor behavior is no longer predicted to occur, accompanied by the formation of a new VBM state. High spin arrangements of nickel in ZnO have been experimentally reported, although the values are slightly higher at 3.29 μ_B.[157] Nickel ions acting as a donor in ZnO at low concentrations would, assuming no other effects dominate, cause the conductivity of the mixed phase to increase due to the increased concentration of free electrons, a behavior which has been experimentally reported,[102,113] however the studies find the conductivity to be activated with some studies assigning the effect to a d-orbital splitting impurity model.[158] The data used in the construction of this model, however, only considers concentrations of 5% dopant and up, the range where this dopant behavior is not observed.

At the higher concentration of 3.7% Ni, the VBM level has increased sharply, by about 0.39 eV compared to pure ZnO. The band gap has reversed the previous trend and slightly increased from the 1.8% concentration value. The composition of the VBM edge at this concentration has changed from the bulk ZnO. This effect is due to the nickel states, and surrounding oxygen states, assuming an energy level that forms a new valence band for the mixed phase structure. The valence band edge is, at a concentration of about 3.7% nickel, formed primarily from O-2p states, mixed with Ni-3d states. Hence, from even a low concentration, the presence of nickel ions within the ZnO structure dominates the valence band edge. At the same concentration, the composition of the conduction band fully matches the character of the bulk ZnO CBM. At the 5.6% concentration limit, the properties of the mixed phase are largely unchanged from the 3.7% concentration. The VBM level and band gap width have both increased slightly, but the difference from the 3.7% values are small.

The sharp increase in the VBM level between the 1.8% and 3.7% concentrations indicate that the concentration limit for the formation of the new VBM edge state is a relatively sudden shift. The qualitative change in the behavior of the nickel ions may be considered as a transition from acting as a dopant, to acting as a substituent. The exact transition point is not known, but the presence of the high-spin nickel species at 2.8% concentration indicates the transition has not occurred at this point. The origin of the transformation appears to be a flip in the spatial orientation of the nickel d-orbital, and the hybridization with the surrounding oxygen p-orbitals. The orbital arrangements are shown in Figure 5-6, which displays the partial charge density, corresponding to the sum 3D isosurfaces of the orbitals within a certain range of energy.

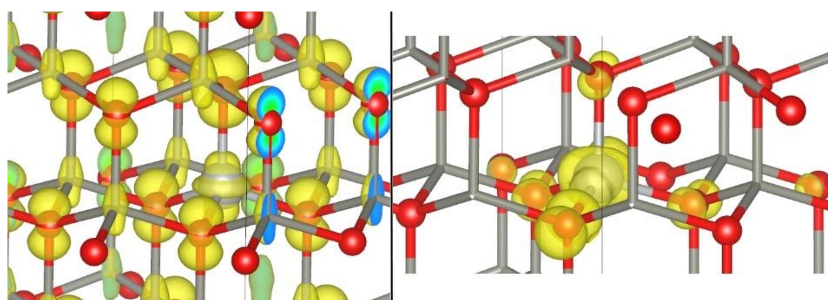

Figure 5-6 Left image: Low limit concentration orientation of orbitals for the Ni:ZnO system, with isosurface level 0.0008. High nickel concentration orientation of orbitals for the Ni:ZnO system, with isosurface level 0.005.

At low concentrations, the Ni-d orbitals are aligned parallel to the c-axis. At higher concentrations, however, the favorable axis is changed, and the d-orbital axis is rearranged parallel with one of the ab-plane wurtzite bonds. The ab-plane arrangement creates significantly more localized energy states, with the surrounding O-2p orbitals with the same axis assuming the same energy level and may be considered a localized impurity state. These ab-plane arranged nickel d-orbital states are the origin to the VBM at high nickel concentrations, explaining the sudden transition, as well as the largely constant VBM level before and after the transition. The transition in magnetic behavior is also caused by the orientation flip. These localized ab-plane states have been experimentally attributed as the origin of the Ni:ZnO band gap red shift, displaying good experimental agreement.[104] Furthermore, while the concentration range differs from the experimental setting, a relatively sudden shift in the effects of nickel doping has also been reported.[113] Due to the nature of this transition, it is possible the specific arrangement of nickel ion in the supercell may affect the transition concentrations. The supercell dimensions

may also have influenced the results, as the a- and b-axes are shorter than the c-axis, resulting in a roughly 1.5 times higher lattice occupancy along the ab-plane.

The CBM energy of ZnO decreases sharply by about 0.3 eV at 1.8% nickel concentration. The change in the band gap width with further addition of nickel is very small, less than the core level uncertainty. The origin of this effect appears to be a shift in the zinc and oxygen s-orbital state energies, induced by the presence of the nickel ions. The nickel e_g orbitals are mixed in with the CBM slightly above energy band edge and is likely the cause of the dopant behavior. The nickel hybridization does not occur at this concentration, in contrast to experimental evidence that assigns the band gap decrease to the same nickel-oxygen hybridized state that forms the VBM. At higher nickel concentrations of 3.7% where the hybridization behavior is present, the DOS indicates a d-band impurity splitting of t_{2g} orbitals (described in the reference) to be present, but at significantly too high energy.[158] The electrons are predicted to assume a lower spin state at this concentration is possibly due to the overestimation of the antibonding t_{2g} orbital energy.

5.2.2. Zinc Dissolved in NiO (Zn:NiO)

Structural Analysis

In the limit of low concentrations, (0.78%), the presence of the zinc ion within the NiO structure has a very slight repulsive effect on the surrounding oxygen ions, extending their bond lengths by about 0.3%. The bonds parallel with the c-axis are further distorted, but that is likely due to the structure considered. The c-parameter is shorter than the a- and b-parameters, as a 4x4x2 supercell structure is utilized, so the zinc "concentration" is higher along the c-axis by a factor of two, resulting in a greater effect on the structure.

In the immediate surroundings of the zinc ion, the rhombohedral distortion of the magnetostrictive effects observed in NiO are counteracted to some extent, so the Zn-O bond angles are closer to right angles than the Ni-O angles with the disruption being reduced by about 42% in the ab-plane, and by 66% in the bc-plane. This effect is reflected in the supercell lattice angles, which approach closer to an ideal cubic arrangement with zinc ion concentration.

Same as the case for Ni:ZnO, at low concentrations, the presence of the zinc ions reduces the volume of the mixed supercell. The effect is lesser in magnitude however, with the volume of the system being reduced by about 0.05%, at the most. The proportion of zinc ions in the NiO structure at the point of this minima appears to be about the same as in the Ni:ZnO structure, but due to lacking resolution of concentration, nothing more specific may be established here. The increase in the lattice parameters is underestimated compared to experimental value of 0.7% at 30% zinc concentration, with an increase of slightly more then 0.4%, but overall good agreement is obtained.[117]

The Ni:ZnO structure is predicted to retain the native antiferromagnetic structure of NiO throughout the concentration range, in accordance with experimental observations. The predicted magnitude of the individual magnetic moments, however behave contrary to the results of the same study, and rather increase by about 0.8% at 31% zinc ion concentration.[120]

Thermodynamic Analysis

The total energy change with zinc ion concentration displays a trend opposite to that of Ni:ZnO. For low concentrations of zinc, the total energy change is negative, predicting the formation of the mixed phase to be thermodynamically favorable. At greater concentrations, however, the total energy change with concentration shifts and becomes positive.

Consequently, mixing of small concentrations of zinc ions into the NiO structure is predicted to be thermodynamically favorable at all temperatures, but is kinetically hindered from occurring at any appreciable rate below an appropriate temperature threshold. For higher concentrations than about 1%, the process becomes endothermic, and hence entropy driven.

Electronic Structure Analysis

The effect of mixing zinc ions into the NiO structure depends on the concentration. The relative VBM level with concentration is shown in Figure 5-7:

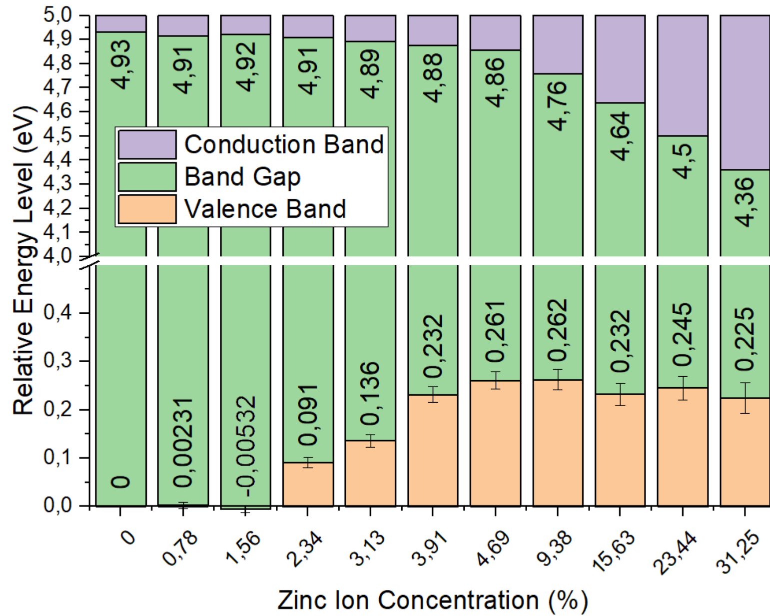

Figure 5-7 Relative band edge levels of the Zn:NiO mixed phase system with concentration of zinc ions. Energy scale of VBM values relative to the band edge of pure NiO, calibrated against the average core orbital level energy of nickel. The error bars at the top of the columns represent the standard deviation of the reference core level energies.

The VBM behavior of the Zn:NiO mixed phase system may be divided into three separate concentration regions: 0-1.56%, 1.56-4.69% and 4.69-31.25%, for regions one to three, respectively. The CBM change also displays some dependence on the concentration, but apart from concentration region one, displays linear dependence throughout within the error margin of the core levels.

At the lower limit concentrations of region one, the VBM level fluctuates, but is largely constant, remaining near the pure NiO level. The reason for the differing behavior compared to the other regions is likely to involve the volume change, as it only decreases in this region. Region two exhibits a nearly linear increase in the VBM level. This region acts as an ideal region with respect to the VBM change, as the volume change no longer interferes with the shift. Region three contains the VBM maximum for the mixed phase system and corresponds to a saturation region with respect to the effect of zinc ion concentration on the VBM level. At higher concentrations than 9.38%, a gradual decrease in the VBM level occurs. It is likely not a physical effect, but rather an error within the methodology used to determine the relative VBM levels, caused by the shift in the reference core levels. As the shift is relatively small, within the core

level error range, the error introduced to the VBM values by the employed approximate methodology may be considered to most likely lie within an acceptable margin. The VBM maximum may be somewhat underestimated due to this effect, however.

Apart from region one, where the volume change is likely to be the dominant factor, the VBM shift may be attributed to the formation of weaker Zn-O-like bonds within the NiO structure. The evidence to this view is the valence band edge composition linearly approaching that of cubic phase ZnO with increasing zinc ion concentration. The endothermic enthalpy of mixing observed beyond the lowest concentration for the Zn:NiO system, as well as the longer Zn-O bonds, compared to the Ni-O bonds, also support this conclusion.

The continuous drop of the CBM is due to the formation of a conduction band state at a lower energy than the CBM of pure NiO. At higher zinc concentrations, the composition of this band is primarily O-2s states, with Zn-4s and Ni-4s states mixed in in proportion, the Zn-4s states increasing with concentration of zinc ions, while Ni-4s diminishes. The CBM shift may be considered a linear change of the nature of the conduction band from that of pure NiO to the composition of bulk cubic ZnO. From the observed behavior, the CBM shift would likely remain linear with concentration change at higher concentrations than experimentally observed. The same drift in the energy level observed for the VBM levels would likely also affect the CBM, but due to the greater shifts in the CBM level the relative error is less relevant.

The behavior of zinc ions in NiO may be considered akin to a diluent of nickel ion concentration. As increasing the zinc concentration changes the electronic structure linearly towards that of cubic ZnO, the initial overestimation of the NiO band gap would cause the obtained CBM change with zinc concentration to be significantly overestimated as well. The cubic ZnO band gap calculated with PBE0 is 3.44 eV, so a CBM drop of 0.8 eV at 31% zinc concentration would indicate the CBM level change would saturate prior to complete substitution of the cation lattice sites with zinc.

5.3. Surface Calculations

The main focus of this project is the interfaces between NiO and ZnO surfaces. A natural point to start for such an investigation, is the properties of the individual material surfaces in a vacuum, within a surface cell that allows the bulk of the surface to be free of strain.

5.3.1. NiO Surfaces

Nonpolar NiO $\langle 100 \rangle$ *Surface*

The ideal $\langle 100 \rangle$ surface, without reconstruction, has a completely planar surface as shown in Figure 5-8.

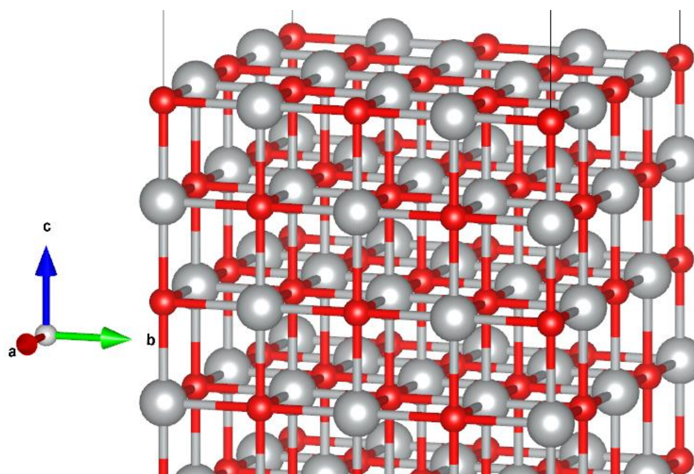

Figure 5-8 The structure of the NiO $\langle 100 \rangle$ *surface.*

Relaxation of the surface causes little surface rearrangement, with the outermost layer of ions only departing the perfect crystal plane arrangement by less than $\pm$ 0.01 Å from the perfect plane, relative to one another, where the oxygen ions extrude slightly, and the nickel ions retract back into the bulk of the slab.

The surface structure itself is very simple, however the complex magnetic rearrangements necessary for the correct formation of this interface, are a cause of considerable difficulty. For many calculation settings, the calculations of the magnetic structure collapses entirely, with the

system converging to an entirely diamagnetic arrangement. The magnetic structure of NiO is integral to its structural integrity in a slab, so assumption of this diamagnetic structure causes the ionic structure to crumple entirely, collapsing in on itself.

Both the GGA+U and hybrid functional calculations predict the magnetic moments to arrange themselves in a layered structure, where the ions closer to the surface have greater magnitude magnetic moments, both for the nickel and the oxygen ions. Furthermore, the oxygen ions form their own magnetic structure, shown in Figure 5-9. This magnetic structure briefly strengthens in magnitude at the first subsurface layer, before it decays rapidly towards the bulk of the slab. By the third layer, the magnetic moment has nearly vanished.

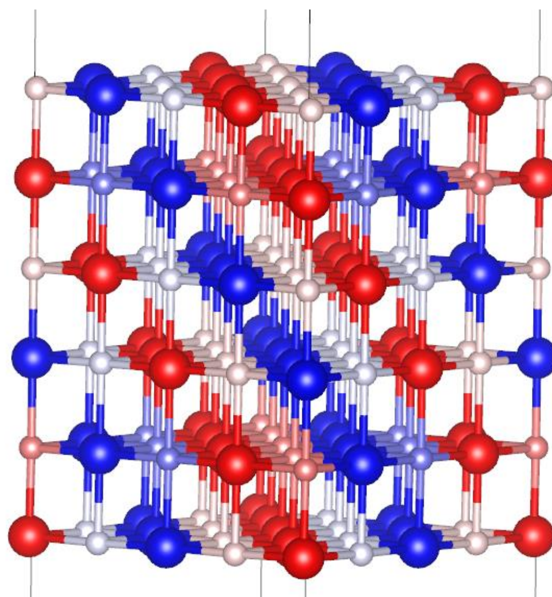

Figure 5-9 The magnetic structure assumed with the NiO ⟨100⟩ surface formation, calculated by hybrid functional. The larger spheres represent nickel ions; Red and blue represents positive and negative magnetic moments, respectively. The smaller spheres represent oxygen ions. The reddish and blueish colors still represent positive and negative magnetic moment, but the magnitude of the moment is indicated by the specific color. The deeper the color, the greater the magnitude of the moment.

The spatially resolved DOS structures display the effect of the presence of the vacuum region on the electronic structure of the slab, shown in Figure 5-10.

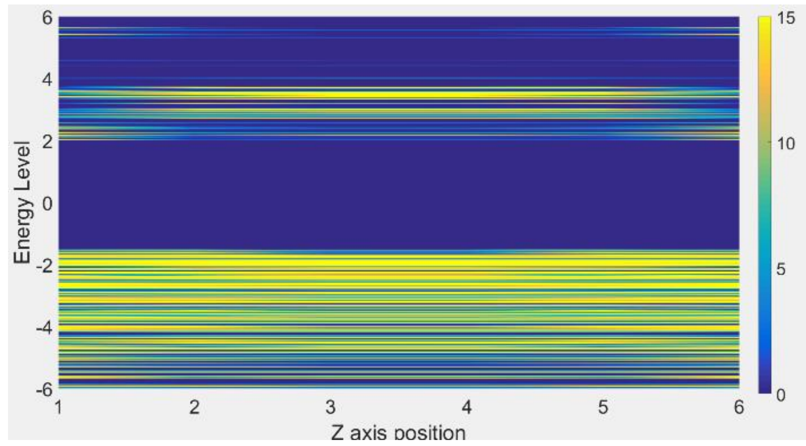

Figure 5-10 Spatially resolved DOS structure of the NiO ⟨100⟩ surface, calculated with hybrid functional with suitably adapted exact exchange proportion.

The hybrid spatially resolved DOS structure displays no mid gap defect states of note, and no reduction in the overall band gap. The most important feature is the increase in the density for the conduction band states around energy level two at z-axis one and six. The increased density corresponds to surface states of NiO, similar states which are observed for all terminations of NiO consideration in this project. The interface states are constructed from almost only Ni-$3d_{eg}$ orbitals. The surface state energies are predicted to be shifted down into the band gap for both hybrid and GGA+U functionals. In the latter case, a total band gap reduction of about 0.5 eV is observed due to surface states.

Nonpolar NiO ⟨110⟩ *Surface*

The NiO ⟨110⟩ surface has, prior to relaxation, parallel ridges along one axis; either the a- or b-axis depending on orientation, but the isolated structures are equivalent. The structure of the surface is shown in Figure 5-11.

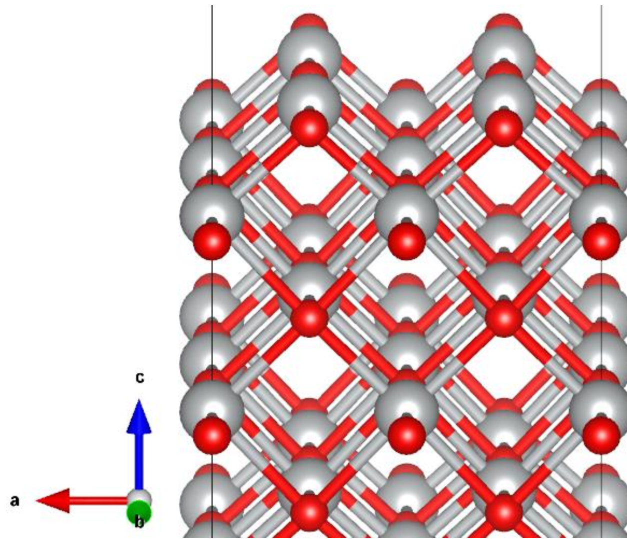

Figure 5-11 Structure of the NiO ⟨110⟩ surface.

The relaxed structure is somewhat widened, and the oxygen atoms extrude slightly towards the vacuum layer. The arrangement of magnetic moments retains the anti-ferromagnetic structure of the bulk structure. Overall, structural rearrangement with ionic relaxation is relatively minor.

The hybrid DOS of the surface, Figure 5-12 (left image), shows that the surface introduces significant mid-gap states, considerably reducing the overall band gap.

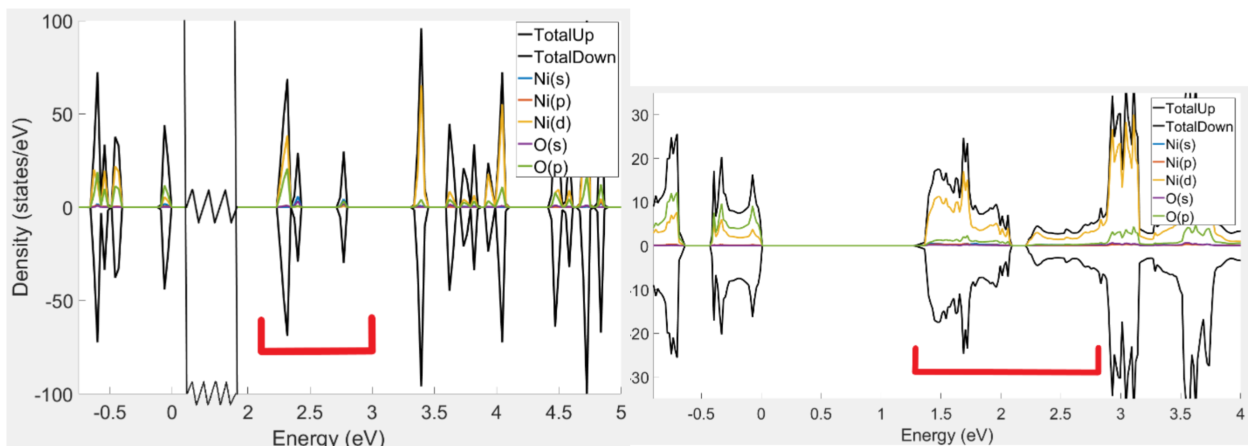

Figure 5-12 Left image: DOS of the NiO-⟨110⟩ surface, calculated by the PBE0 functional, using 18.5% exact exchange. Right image: DOS of the NiO-⟨110⟩ surface, calculated with GGA+U. Y-axis of both figures have the same title and units. The conduction band surface states are marked by the red section.

The hybrid DOS valence band composition is unchanged from the bulk material. The introduction of surface states to the DOS creates mid-gap states composed primarily of Ni-3d

orbitals, with O-2p states mixed in, reducing the effective band gap of the material by half. The increase in the O-2p orbital contribution is likely mostly a consequence of the gamma-point only calculation, as the same behavior is observed in bulk calculations. More gap states present at higher energies, composed of a mix of multiple different states. The difference in the composition of the lowest energy mid-gap state compared to the ⟨100⟩ surface is likely due to the introduction of oxygen ions with two missing bonds, as opposed to one.

The GGA+U DOS, Figure 5-12 (right image), shows similar overall traits, but with distinct differences. Unlike the hybrid calculation, the mid-gap states are predicted to be composed primarily of Ni-3d orbitals, with a much smaller mixing of O-2p states. The GGA+U functional significantly underestimates the contribution of oxygen to the surface states, a point which must be noted for consideration of interfaces in section 5.4. The valence band is also affected, forming a gap in the states not present in the bulk material about 0.4 eV below the VBM. The mid-gap states are due to the formation of weakly bound electron states forming in continuous bands along the surfaces, as shown in Figure 5-13.

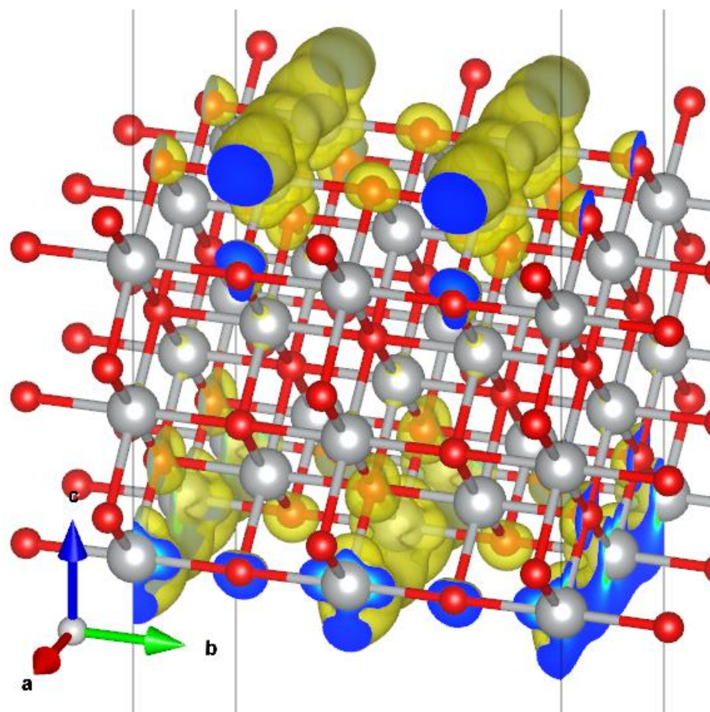

Figure 5-13 Partial electron density composition of the NiO-⟨110⟩ surface, calculated with GGA+U. The states shown in the image correspond to the gap states in Figure 5-12 (right image). The contour density is 0.005. Further density is introduced into these surface states at higher energy.

The presence of such delocalized electron densities, and the mid-gap states they constitute, may have a considerable effect on a heterojunction. The orbitals producing these contours correspond to the mid-gap states in Figure 5-12 (right image) and determine the overall conduction band level for the structure. At practical temperatures they serve to introduce localized charge density to the vacuum region immediately adjacent the surface, with greater spatial expansion along the c-axis than the bulk states permit.

The geometry of the contours displays repulsion from the negatively charged oxygen ions, with indentations in the regions closest. The overall structure is thus likely due to sum repulsion of the nickel states from the oxygen ions closer to the bulk of the structure.

It is likely that only a $\langle 110 \rangle$ surface without significant structural defects would form continuous states. A reconstructed surface with ridge peaks two or more ionic layers apart (along the a-axis in this case), would likely exhibit more localized surface states around each ridge peak nickel ion. Hence, restructuration of the $\langle 110 \rangle$ surface to form more spaced out ridges may present a viable pathway for the reduction of NiO surface states.

The delocalized surface states may also have a notable effect on conductivity across a junction, due to their coherent shape and effect of introducing electron density into an otherwise isolating region of space. It is also possible that the relative orientation of the $\langle 110 \rangle$ surface may play a role as well, due to the directional distribution of electron density, but this depends on the ab-plane symmetry of the paired surface.

Polar NiO $\langle 111 \rangle$ *Surface*

The NiO $\langle 111 \rangle$ surface is the simplest polar surface of NiO. As previously mentioned in section 3.1.4, two opposite nickel and oxygen ion terminations are coupled together. The separate terminations exhibit different features and must be considered individually.

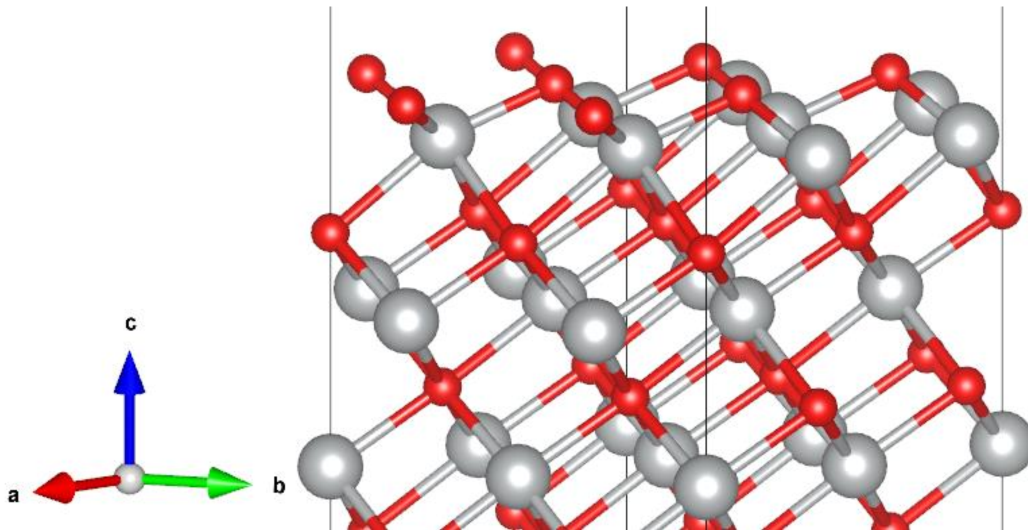

Figure 5-14 Relaxed oxygen termination surface of the NiO ⟨111⟩ *surface.*

In the relaxed structure, the surface ions are retracted directly towards the bulk of the slab, with no shift in the ab-plane coordinates. The terminating nickel ion structure is only slightly altered, while the adjacent oxygen layer is altered from the bulk structure to a negligible degree. The terminating oxygen ions relax to a considerably greater extent, where the first sub-surface nickel ion layer is altered to a greater degree than the terminating nickel ions. The relaxation behavior indicates the oxygen termination to less stable than the opposite nickel termination with respect to the presence of a vacuum.

The presence of the internal dipole moment of the polar surface slab has significant effects on the electronic structure. The GGA+U total DOS, shown in Figure 5-2, is distorted to the extent that the location of the band gap is difficult to ascertain.

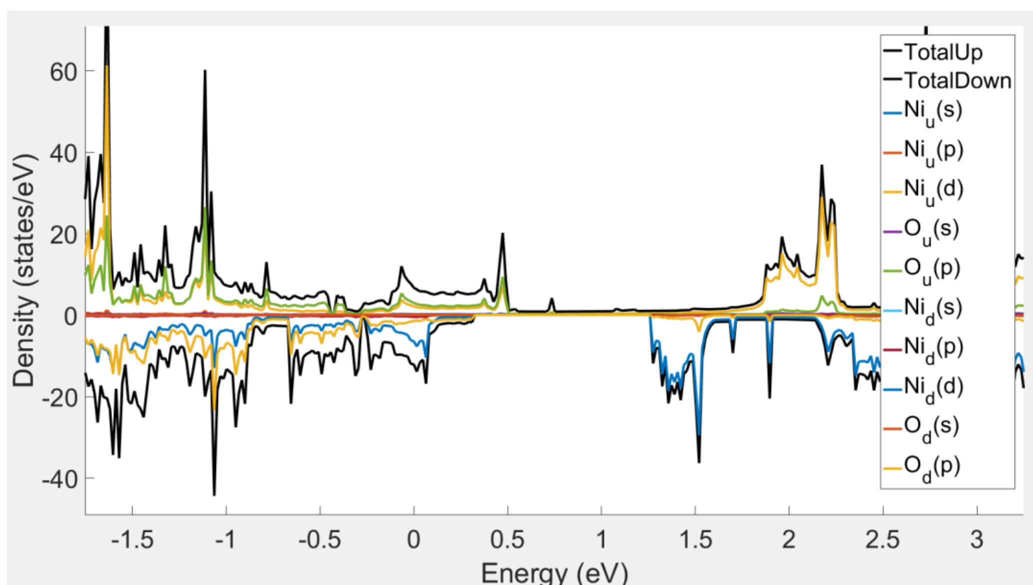

Figure 5-15 DOS of the NiO-⟨111⟩ surface, calculated with GGA+U. The Fermi energy is located at Energy = 0. Subscripts u and d refer to spin up and down, respectively.

The separate spin states are displaced from energetic degeneracy due to the internal dipole of the surface slab. The up-spin bulk band edge compositions are observed at 0.5 and 1.25 eV, which may be considered the total band gap. Between the VBM and CBM, the entire gap is covered in states, primarily composed of Ni-3d orbitals. The DOS energy shift through the slab may be observed from the spatially resolved DOS structure, shown in Figure 5-16.

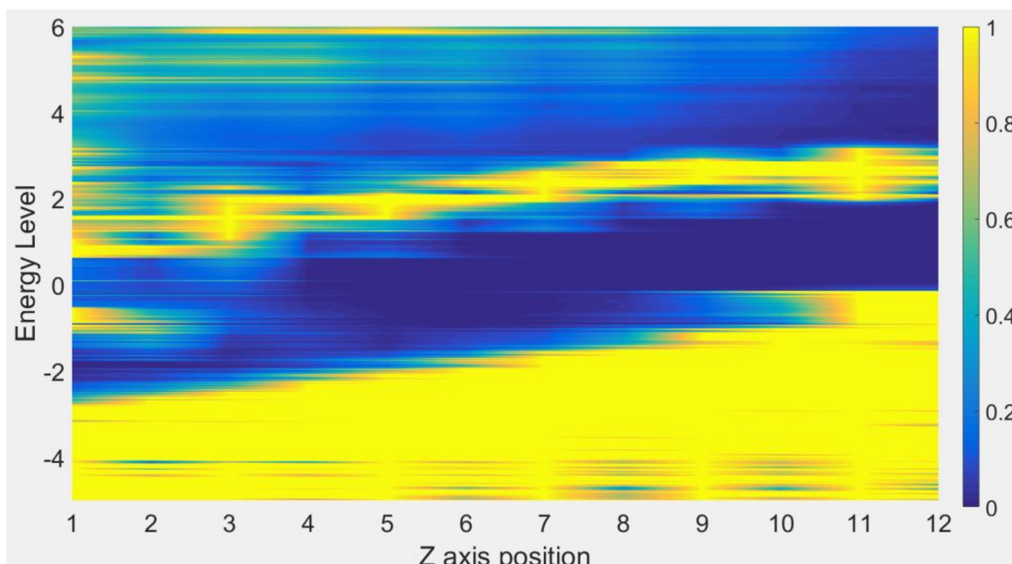

Figure 5-16 Spatially resolved DOS of NiO-⟨111⟩ surface, calculated with the GGA+U functional. The left of the plot corresponds to the nickel termination, while the right side corresponds with the oxygen termination.

The oxygen termination exhibits the most prevalent valence band surface states of the NiO surfaces due to the extent of the oxygen surface relaxation, observed at z-axis 11 to 12. The nickel termination of the surface slab is dominated by mid-gap surface states. The density of states at the surface are continuously non-zero across the band gap, forming akin to a metallic DOS structure in this region.

The gap states at the nickel termination were in Figure 5-15 observed to be primarily composed of Ni-3d states. Same as the ⟨110⟩ surface, the states are conduction band states that have shifted down in energy due to decreased electrostatic repulsion from surrounding negatively charged oxygen ions. A notable difference between the polar and non-polar surfaces, is that the ⟨110⟩ states are confined to a specific region of energy, while the ⟨111⟩ states are continuous throughout the band gap, because of the spatial expansion of the surface states. As shown in Figure 5-13, the surface states are restricted from freely expanding by the ionic arrangement. The ⟨111⟩ surface does not have this restriction, as only nickel ions are present at the surface, forming a continuous density distribution along the surface.

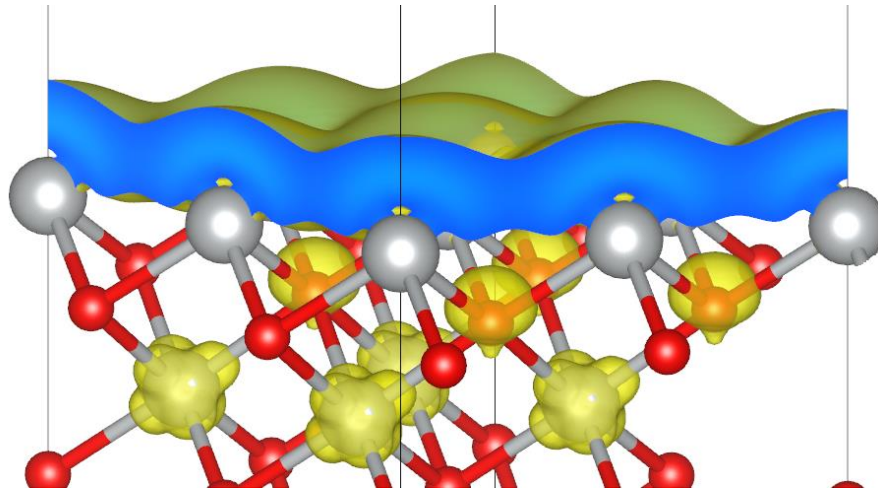

Figure 5-17 Partial charge density of the NiO-⟨111⟩ nickel termination surface, with an energy range corresponding to the mid-gap region of Figure 5-15. Isosurface level is 0.0006.

As observed in the ⟨110⟩ surface structure, the cause of the surface states is due to the asymmetry of the structure at the surface. The same principles apply for the ⟨111⟩ surface. As there are no oxygen ions at the surface, so the surface states assume a continuous charge density region.

NiO Surfaces: Surface Energy and Band Edges

The formation of a surface causes a change in the total energy of the structure to change compared to the bulk material. These surface energies, and the changes observed, thus serve as an indicator to the relative stability and favorability of different surfaces and conditions. The surface energies of the NiO terminations are given in Table 5-5.

Table 5-5 Surface energies of the NiO terminations, calculated with GGA+U.

Termination	Surface Energy (J/m^2)	Prior Literature (J/m^2)
$\langle 100 \rangle$	0.84	1.15[67]
$\langle 110 \rangle$	2.70	2.77[67]
$\langle 111 \rangle$	5.01	4.5[49]

The calculated surface energy of the $\langle 110 \rangle$ surface shows good agreement with previous literature, but the values for the $\langle 100 \rangle$ and $\langle 111 \rangle$ surfaces under- and overestimates the surface energy, respectively, considerably. The results are, however, in qualitative agreement on the relative stability of the surfaces.

The calculated band edge energy levels of NiO relative to the vacuum level are not identical between separate surfaces; a considerable degree of difference may occur as a consequence of the surface properties. The band edge levels of the various surface terminations calculated with the GGA+U and hybrid functionals are shown in Figure 5-18.

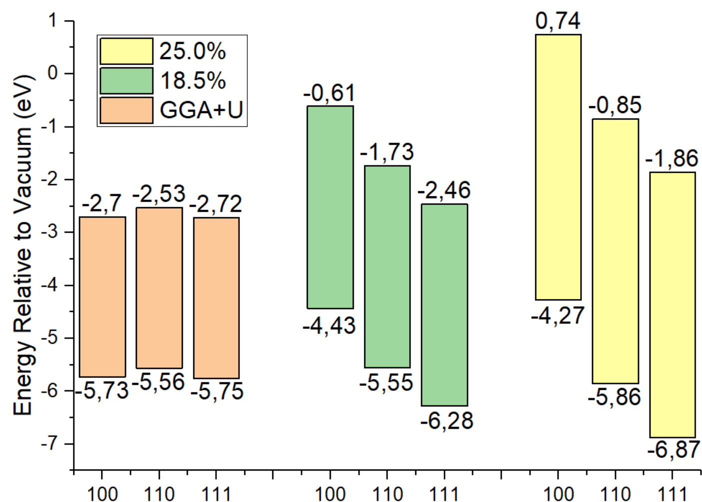

Figure 5-18 Band edge energy of the NiO surfaces relative to the vacuum level, calculated with the various functionals.

The GGA+U functional gives the most consistent results between the surfaces. The calculated VBM energy levels are too low but show overall good agreement with experimental evidence, which places the VBM at about -5.4 eV.[1] Due to the underestimated band gap, the CBM level is significantly too low.

The 18.5% hybrid functionals obtain a better estimate of the band gap, however the lower consistency of the absolute values of the VBM levels indicates the GGA+U method may be the better choice for determining the relative levels of the band gaps. Utilizing the standard exact exchange of 25%, the VBM values are not changed much, but they are overall shifted away from the experimental values for the band edge levels, resulting in worse agreement overall.

Final Considerations for the NiO Surfaces

The NiO surfaces all tend to form surface states corresponding to the mid-gap energy range, although the extent varies between different surfaces. The surface states are predominantly shifted conduction band states, and primarily occupy the spatial region in the vacuum outside the slab itself. Generally, these conduction band states form between the closest neighbor nickel ions, and link together into continuous surface bands, while not forming in the regions immediately adjacent the negatively charged oxygen ions. Consequently, the bands expand space

with the same ab-plane symmetry as the surface itself, resulting in anisotropic band density for surfaces with lower symmetry such as $\langle 110 \rangle$.

5.3.2. ZnO Surfaces

Nonpolar ZnO $\langle 10\bar{1}0 \rangle$ *Surface*

ZnO, due to the lower ionic coordination number of the wurtzite structure, exhibits more extensive relaxation at the surfaces compared to NiO. In the relaxed $\langle 10\bar{1}0 \rangle$ surface, Figure 5-19 (right image), the oxygen ions extrude towards the vacuum layer and the zinc ions are displaced towards the bulk. The bond lengths remain largely unchanged, in agreement with experimentally observed behavior.[74]

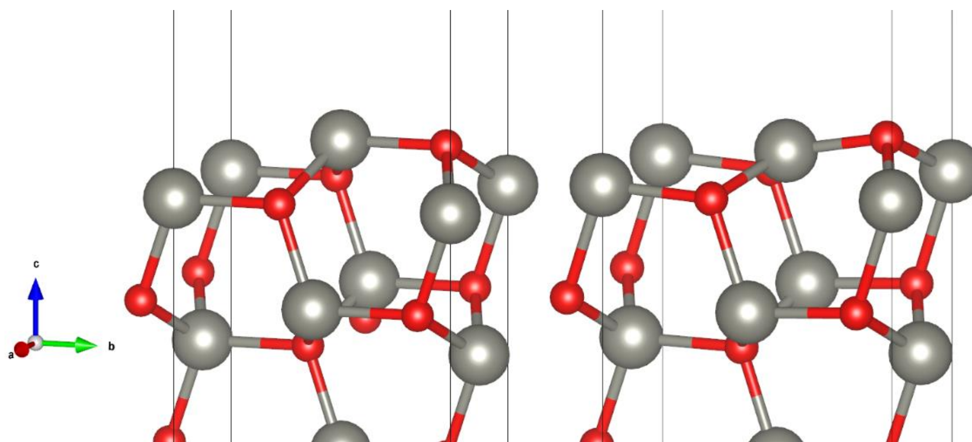

Figure 5-19 Nonpolar ZnO $\langle 10\bar{1}0 \rangle$ *surface. Bulk and relaxed structures to the left and right, respectively.*

The PBE0 DOS structure shows no presence of gap states within the band gap, but the width of the band gap is somewhat narrowed. The GGA+U DOS gives similar results; The general structure of the DOS is unchanged from the bulk calculations, and no gap states have been introduced. The band gap has, however, been reduced by about 0.1-0.2 eV.

The reduction in the band gap is primarily due to shifted valence band states in the vicinity of the surface, as they may be observed to have increased in density near the surfaces in the spatial DOS, shown in Figure 5-20:

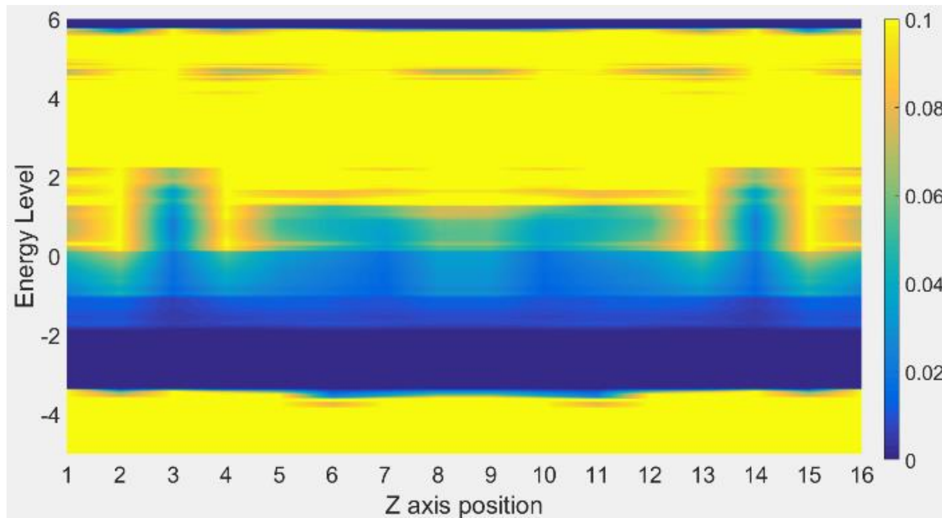

Figure 5-20 Spatially resolved DOS of the ZnO $\langle 10\bar{1}0 \rangle$ *surface calculated with the GGA+U functional.*

The spatial DOS shows the surface to display a relatively clean density structure. The surface states largely only occur within the bulk conduction band and would not influence the properties of the material considerably. The slight decrease in band gap appears to be due to a shift up in the energy of the valence band states, likely due to the surface relaxation. The effects of the more extensive surface relaxation on the DOS may be observed in the conduction band density at z-axis 2/15 and 4/13: The relaxation affects the subsurface layers to a significant degree, resulting in two layers of surface states in the DOS structure. This same trait is also observed for the $\langle 11\bar{2}0 \rangle$ surface.

The surface states of the ZnO nonpolar surfaces form continuous bonds between adjacent zinc ions in a similar manner as NiO, forming a similar anisotropic charge density distribution for the conduction bands. The main difference from the NiO surface states, is that the oxygen ions contribute significantly to these surface states from O-2p orbitals, rather than inhibit them.

Nonpolar ZnO $\langle 11\bar{2}0 \rangle$ *Surface*

The $\langle 11\bar{2}0 \rangle$ surface relaxation is similar to the $\langle 10\bar{1}0 \rangle$ surface: The zinc ions are displaced towards the bulk of the structure, and the oxygen ions towards the vacuum layer. Additionally, the relaxed $\langle 11\bar{2}0 \rangle$ surface displays akin to a torsional twist on the outer layer, parallel to the ab-

plane, rather than a straight move into or out of the slab. The bulk and relaxed surface structures are shown in Figure 5-21:

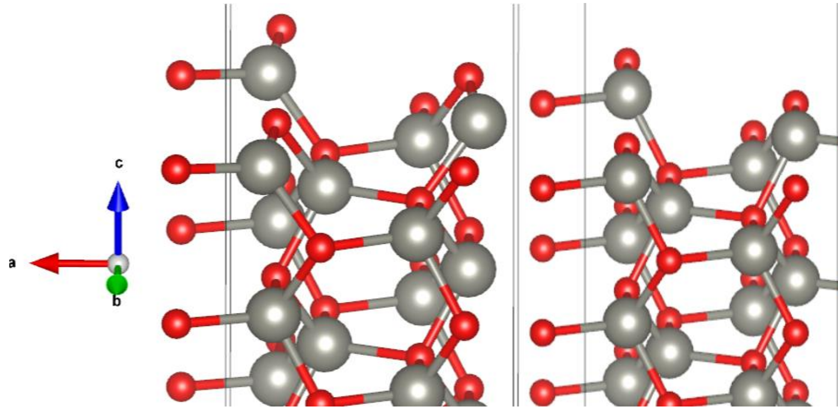

Figure 5-21 ZnO $\langle 11\bar{2}0 \rangle$ *surface termination, before and after relaxation to the right and left, respectively.*

Different from the $\langle 10\bar{1}0 \rangle$ surface, the band gap increases compared to the bulk, by about ~0.1-0.2 eV. The $\langle 11\bar{2}0 \rangle$ surface is the only surface to display a fully constant band gap throughout the surface slab, with no mid-gap states.

Polar ZnO $\langle 0001 \rangle$ *Surface*

In the relaxed polar ZnO $\langle 0001 \rangle$ surface, the termination ions are retracted directly towards the bulk of the slab. The surface arrangement approaches a planar trigonal arrangement of the surface- and subsurface- ionic layers, minimizing the dipole moment. The bulk structure termination is shown in Figure 5-22.

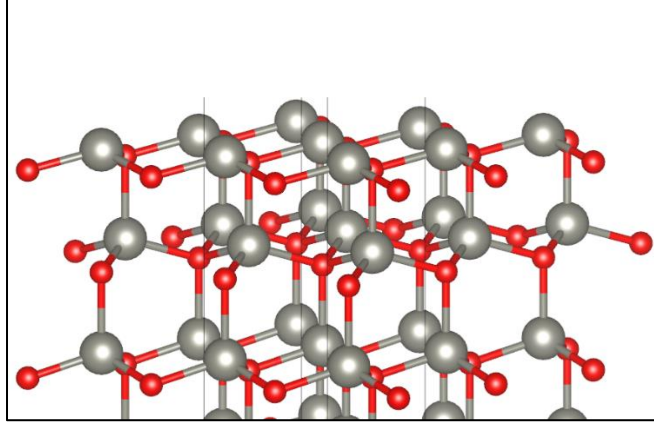

Figure 5-22 Static structure of the ZnO ⟨0001⟩ surface termination. The image displays the cation termination; the oxygen termination is equivalent, with the oxygen and zinc ion lattice sites reversed.

The spatially resolved DOS, shown in Figure 5-23 (left image), shows that the DOS energy level of the surfaces is considerably affected by the internal dipole of the slab, causing a constant shift in energy levels throughout the surface slab.

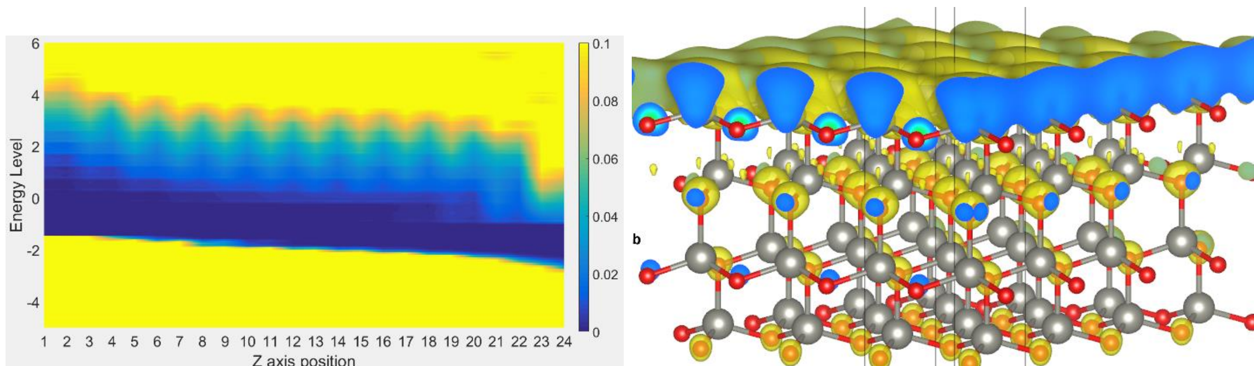

Figure 5-23 Left image: Spatially resolved DOS of the ZnO ⟨0001⟩ surface. The left side of the image corresponds with the oxygen termination. Right image: Partial charge density of the ZnO ⟨0001⟩ surface, corresponding to the surface state energies of the zinc terminal ions in the left image. Isosurface density is 0.0005.

The sudden decrease in the energy level of the conduction band is due to surface states occurring at the metal ion termination, as may be seen from a partial electron density distribution.

The cation termination surface states are composed entirely of Zn-4s states. The less uniform charge density compared to the polar NiO surface is likely due to the smaller distance between the surface and first sub-surface layers, with the repulsive effect of the oxygen ions affecting the surface states, as well as the more localized nature of the 4s orbital.

Polar ZnO $\langle 000\frac{1}{2}\rangle$ *Surface*

This surface relaxes in a manner analogous with the $\langle 0001\rangle$ surface from the second ionic layer from the surface. However, the termination ions are highly structurally unstable under physical conditions. They only maintain their shape due to the periodic boundary conditions, and the perfect lattice of equivalent ions that form their surroundings because of it and hence do not relax in a typical manner.

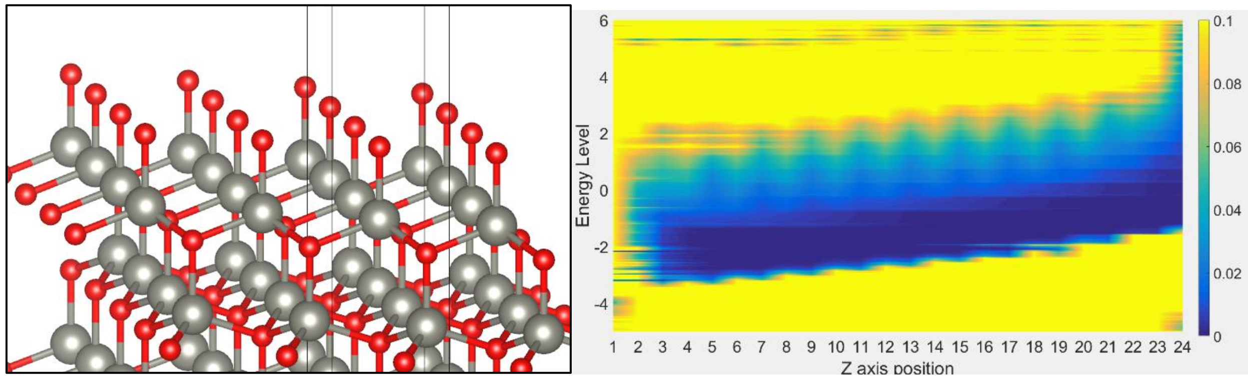

Figure 5-24 Left image: ZnO $\langle 000\frac{1}{2}\rangle$ *oxygen termination surface. The zinc termination is equivalent, but with the oxygen and zinc lattice sites swapped. Right image: Spatially resolved DOS of the ZnO* $\langle 000\frac{1}{2}\rangle$ *surface. The left side of the image correspond with the nickel termination, and the right side with the oxygen termination.*

The $\langle 000\frac{1}{2}\rangle$ surface is identical in structure to the $\langle 0001\rangle$ surface, apart from the termination ions, and produces a similar spatially resolved DOS structure, shown in Figure 5-24 (right image). The entire band gap is filled with states at the nickel termination, of similar nature to the $\langle 0001\rangle$ surface states. The zinc ions are further distanced from the oxygen ions of the first sub surface layer compared to $\langle 0001\rangle$, producing surface states that, similarly to NiO-$\langle 111\rangle$, are much less spatially restricted than the nonpolar and less polar surfaces. The surface states essentially form a metallic band state, with no energy gap.

ZnO Surfaces; Surface Energy and Band Edges

The surface energies of the clean ZnO surfaces are given in Table 5-6:

Table 5-6 Surface energies of clean ZnO surfaces, calculated with the GGA+U functional.

Termination	Surface Energy (J/m^2)	Earlier Literature (J/m^2)
$\langle 10\bar{1}0 \rangle$	0.95	1.6[97]
$\langle 11\bar{2}0 \rangle$	0.99	1.7[97]
$\langle 0001 \rangle$	1.88	3.31-3.4[95,97]
$\langle 000\frac{1}{2} \rangle$	5.64	Not Available

The nonpolar surfaces are predicted to be roughly equally stable, with the polar $\langle 0001 \rangle$ surface exhibiting twice as high surface energy. While the absolute surface energies significantly underestimate the literature values, the relative values agree with the respective ratios lying within a 5% margin of error. The surface energy of the $\langle 0001 \rangle$ polar surface is relatively low compared to the other polar surfaces under consideration, ZnO-$\langle 000\frac{1}{2} \rangle$ and NiO-$\langle 111 \rangle$.

The $\langle 000\frac{1}{2} \rangle$ surface energy is very high, close to the NiO-$\langle 111 \rangle$ surface energy. Consequently, like the latter, it is unlikely that the $\langle 000\frac{1}{2} \rangle$ surface could exist in a stable manner without reconstruction, especially since its form is also structurally unstable.

The band edge levels calculated with the GGA+U and hybrid functionals are shown in Figure 5-25:

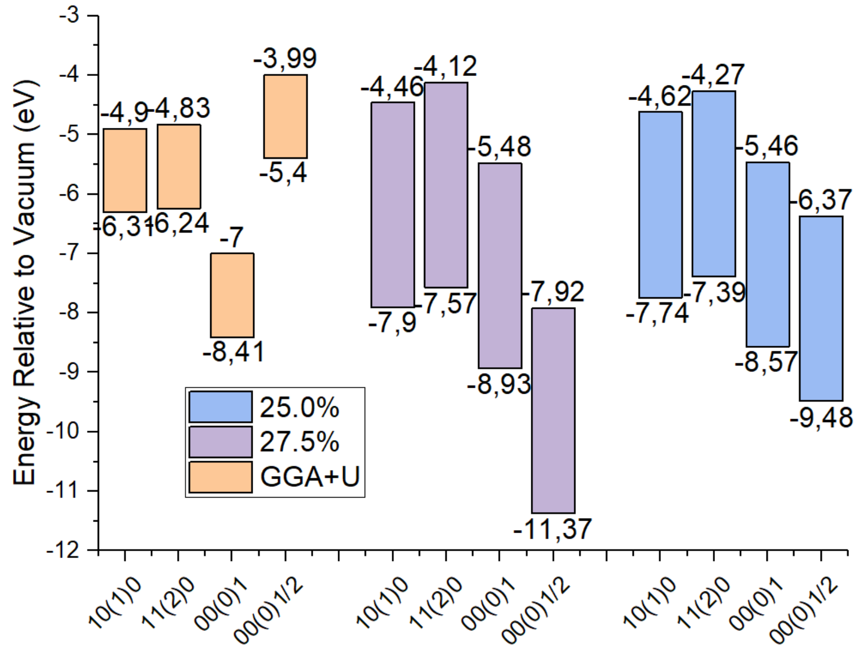

Figure 5-25 Valence and conduction band edge levels of ZnO surfaces, calculated with the GGA+U and hybrid functionals.

The VBM values of the nonpolar surfaces are largely consistent with one another with the same functional, while the polar surfaces vary quite considerably due to the dipole moments. The VBM levels of the nonpolar surfaces are, however, compared to prior literature and experimental evidence, considerably high.[159,160] These results typically place the VBM of ZnO around the -7.0 eV to -7.5 eV level. As the high VBM of ZnO from GGA+U would produce strange interface band offsets in later sections, a correction scheme will be employed:

The GGA+U misplacement of the VBM on an absolute scale could be considered as primarily an issue related to the placement of the VBM relative to the reference potential within a bulk potential. Comparing the reference potential levels of the nonpolar interfaces between hybrid with fitted exact exchange and GGA+U, they are found to be relatively similar. The polar interfaces differ significantly, primarily due to a difference in the charge distributions with the dipole field. The relative VBM calculations, predict a significant difference of about 1.5 eV between the functionals. If the hybrid relative VBM value is utilized, rather than the GGA+U derived, the results are considerably improved:

Table 5-7 Absolute band edge levels utilizing local potential of GGA+U with Hybrid functional relative VBM.

Termination	VBM Relative to Vacuum	CBM Relative to Vacuum
$\langle 10\overline{1}0\rangle$	-7.73	-4.28
$\langle 11\overline{2}0\rangle$	-7.66	-4.21
$\langle 0001\rangle$	-9.83	-6.38
$\langle 000\frac{1}{2}\rangle$	-6.82	-3.37

With this arrangement, the $\langle 10\overline{1}0\rangle$, $\langle 11\overline{2}0\rangle$ and $\langle 000\frac{1}{2}\rangle$ absolute band edges are considerably improved, to roughly on par with the hybrid methodology. This is important due to the inability to run proper hybrid calculations of most interfaces. While this is an ad hoc process, the main utility of the band edge levels is for the determination of band offsets, where the actual shape of the DOS apart from the edges is not important. Where this method is used, it will be referred to as "mixed" band edges. This correction scheme has no physical basis and will necessarily introduce a degree of error and uncertainty to the results. However, as the value utilized from the hybrid calculation is a constant to be applied to variables from GGA+U equivalently, the procedure may also be considered as a simple ad hoc shift of the ZnO VBM by about -1.5 eV to produce more useful results; Comparison between different interfaces, would produce the same relative differences in band offset, hence reducing the severity of the introduced errors.

The 27.5% exchange fraction hybrid functional results are less stable for the individual surfaces, and do not agree with the VBM levels of the GGA+U results for any of the surfaces. Compared to experimental results, the obtained VBM levels are closer to the real values for the nonpolar surfaces, but the dipole effects once more interfere with the values obtained for the polar surfaces. The standard exact exchange fraction increases the VBM energy levels for all the surfaces compared to the specifically chosen value. As the specifically chosen value tended to place the energy levels too low, the standard exchange generally improves the result. For the nonpolar surfaces, the VBM value agrees quite well with experimental results, but the polar surfaces are still placed considerably too low.

Final Considerations for the ZnO Surfaces

The nonpolar ZnO surfaces behave similarly with respect to structure, stability and electronic structure. They are both the most stable of the ZnO surfaces. While the surface states primarily have the character of the conduction band, the energy level lies mostly outside the band gap (within the scope of the underestimated band gap) and would not likely cause mid-gap interface states. Due to the surface ionic structures, the conduction band surface states exhibit anisotropic expansion similar to the NiO-$\langle 110 \rangle$ structure, but less spatially constrained as the oxygen orbitals contribute to the states, rather than repel them.

The polar surfaces display the opposite traits, exhibiting considerable surface states and relatively unstable surface energies. The $\langle 0001 \rangle$ surface states display traits akin to an intermediate between NiO-$\langle 110 \rangle$ and NiO-$\langle 111 \rangle$ surface states, while the $\langle 000\frac{1}{2} \rangle$ surface behaves similarly to the NiO-$\langle 111 \rangle$ surface.

Final Considerations for Surface Calculations

The agreement between the results obtained in this section and prior literature is varying, with some results approaching very close, and other results having considerable error. Qualitative agreement is obtained for most values, however.

There are several differences between the properties of the NiO and ZnO surfaces. The most important difference for later considerations of interface electronic structure, however, is the origin of the respective surface states: In non-polar NiO surfaces, the surface states occur almost entirely at the surface itself, originating predominantly from the termination nickel ions. In the non-polar ZnO surfaces, however, the surface states are closer to bulk states that extend out from the surface slab, into the surrounding vacuum region. A possible consequence of this difference in an interface, is that the NiO states would act as electron traps, while the ZnO states would act closer to a conducting region. Similar traits are also observed for the ZnO-$\langle 0001 \rangle$ surface, the small difference between the ionic planes at the surface facilitates a considerable contribution from the sub-surface layers to the surface states, a property not observed in NiO.

5.4. NiO-ZnO Heterojunction Interfaces

Within the bounds of a computational investigation, unless there is a perfect match between the lattice parameters of the components of a junction, strain must be applied to the system to accommodate both components within the same surface cell. For a heterojunction, the strain may be either compressive, tensile or shear, each affecting the properties of the materials differently. Experimental investigations of strain effects for heterojunctions show that electronic properties such as band alignment depend considerably on the strain distribution.[161,162] A choice must thus be made in how to distribute the strain between the surfaces. In this case, only one of the surface slabs are strained, to replicate the conditions of a deposition process of one material on a strain free second phase. Another approach would be to distribute the strain equally between the surfaces, or in proportions decided by the elastic moduli of the respective materials. This latter approach would represent the closest approximation to the strain distribution one would expect within a nanocomposite, or simultaneous precipitation of multiple phases from a single supersaturated phase. In these cases, depending on the system, multiple forms of strain would be present, for instance in the form of compressive strain on one material, and tensile strain on the opposite.

As previously mentioned in section 3.3.1, the interface optimization process follows a multi-step procedure. To shortly summarize:

1. Optimization of relative arrangement in ab-plane.
2. Optimization of interface width (distance between surfaces along the c-axis).
3. Optimization of ionic positions.

The strain applied to each interface system is given in Table 5-8:

Table 5-8 Strain imposed on the system to fit the NiO and ZnO surfaces together.

Interface NiO Surface – ZnO Surface	Strain (% Distortion from bulk structure)
$\langle 100\rangle$ - $\langle 10\bar{1}0\rangle$	11.86
$\langle 100\rangle$ - $\langle 11\bar{2}0\rangle$	8.15
$\langle 110\rangle$ - $\langle 10\bar{1}0\rangle$	2.51
$\langle 110\rangle$ – $\langle 11\bar{2}0\rangle$	4.57
$\langle 111\rangle$ - $\langle 0001\rangle$ / $\langle 111\rangle$ - $\langle 000\frac{1}{2}\rangle$	5.68
$\langle 111\rangle$ - $\langle 10\bar{1}0\rangle$	2.60
$\langle 111\rangle$ - $\langle 11\bar{2}0\rangle$	0.70

The $\langle 100\rangle$ surfaces are both considerably strained, but a lower strain was not applicable within a reasonable system size. The $\langle 111\rangle$ - $\langle 11\bar{2}0\rangle$ interfaces show the best fit between the respective surface structures.

5.4.1. Interface Optimizations

Relative Interface Configurations

A note on notation: For interfaces involving a polar surface, the interface arrangement of surfaces is followed by either Ni-O or Zn-O, to indicate which surface supplies which termination to the interface. The former means that the NiO surface supplies the cation termination, and the latter means NiO supplies the oxygen termination. This notation is employed both for polar-polar and polar-nonpolar interfaces.

The relative energies of the interface structure conformations display relatively small variation. Comparing the total energy of the various conformations, several surfaces displayed a standard deviation of less than 0.1 eV, including all polar-polar, and several nonpolar-nonpolar interfaces. The polar-polar interfaces all display low variance in energy, likely due to the interface interaction energy being dominated by the electrostatic interaction of the oppositely charged termination ions.

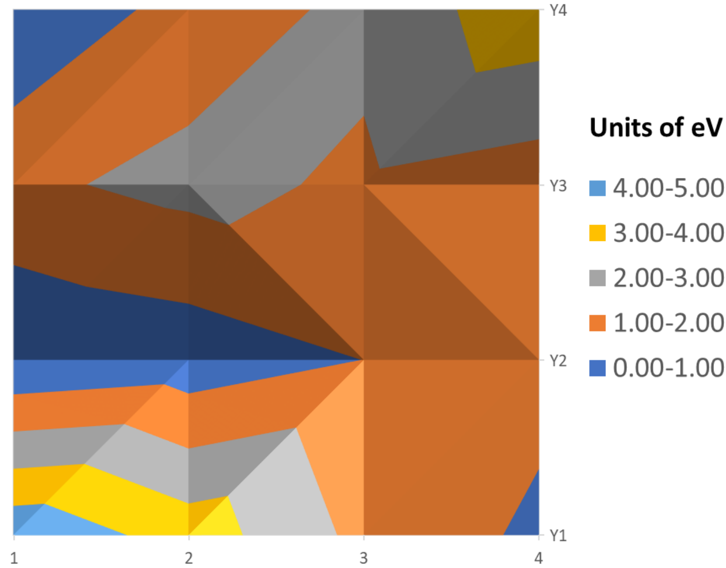

Figure 5-26 Conformational energy surface for the strained ZnO 111-1010 interface.

The behavior of the interface structure energies with respect to differing interface width (without spin polarization) for the most part display a continuous curve characteristic of atomic interactions. Early attempts at optimizing the width with spin polarization enabled, showed that, for certain interfaces, the magnetic structure would create an energy barrier, preventing the system from assuming the minima region for non-spin polarized region. This new magnetic state would also create a new local energy minimum for the interface width, rather than being purely repulsive, see Figure 5-27. Consequently, certain interfaces may be in local minima conformations with respect to interface widths, as the subsequent relaxation process started from the minima of the non-spin polarized energy surfaces.

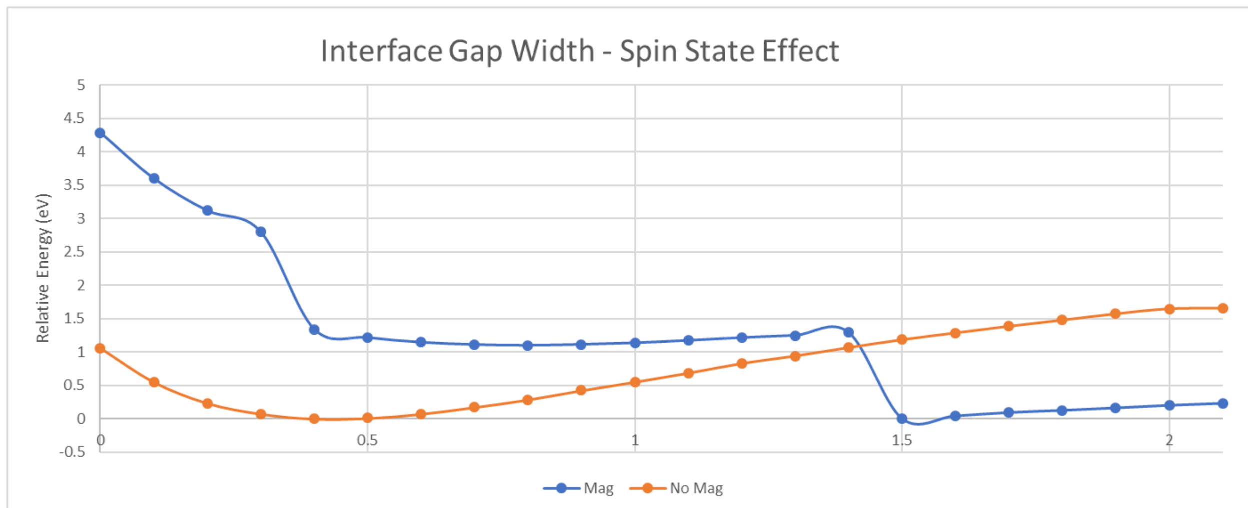

Figure 5-27 A comparison of the energy landscape with and without spin polarization. The absolute axis scales are arbitrary. Moving in the positive direction along the x-axis corresponds to a wider interface gap.

5.4.2. Relaxed Structure Interfaces

Upon initial construction, the interface structures utilize the bulk parameters of the surface materials, albeit strained. The interface environment requires the ionic structures to rearrange to assume the new minimum-energy conformation. These rearrangements affect the properties of the interface, which, in a heterojunction, this is of special importance as the bonding across the interface is unique to every surface pair. Of the two arrangements of strain distribution considered, however, only the structures with strained ZnO slabs have all been fully relaxed. In section 5.4.2, all results and discussion will refer to the relaxed interfaces with strained ZnO structures.

Interface Formation Energies

The interface formation energy provides information on the relative favorability of the formation of the various interfaces. The interface formation energies of the relaxed interfaces with strained ZnO is shown in Figure 5-28:

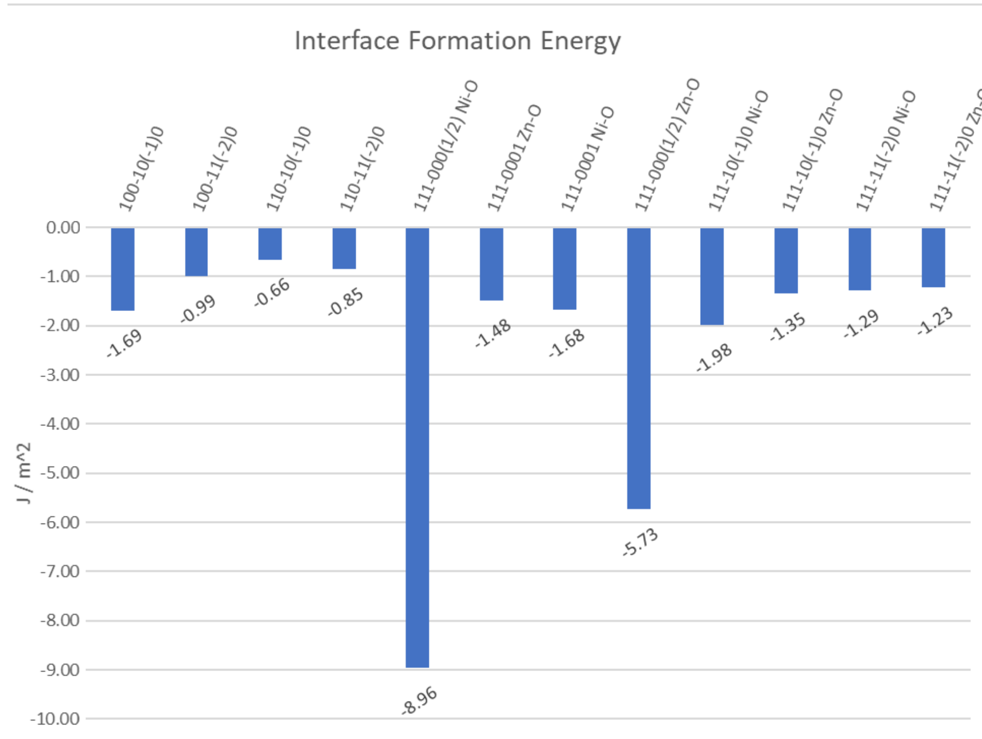

Figure 5-28 Interface formation energies of the NiO-ZnO interfaces, with strained ZnO. The Ni-O and Zn-O labels indicate what ions are contributed to the interface by the polar NiO surface slab, referring to the nickel- and oxygen terminations of the NiO surface, respectively.

The two arrangements of the polar-polar surfaces $\langle 111 \rangle - \langle 000\frac{1}{2} \rangle$ are the most favorable of the interfaces. The reason is partly due to the polar-polar attraction between the surfaces, but also the unstable structure of the ZnO-$\langle 000\frac{1}{2} \rangle$ surface, and the stabilization of this by incorporation of the charged ZnO surface ions into the lattice of the opposite NiO surface. These interfaces may alternatively be considered akin to a $\langle 111 \rangle - \langle 0001 \rangle$ interface with a partially saturated monolayer incorporated into the structure at the interface to improve bonding between the separate crystal structures.

For all surfaces either polar-polar or polar-nonpolar, any interface that incorporates the polar nickel termination is always more favorable than the reverse case. Except for the $\langle 100 \rangle$ - $\langle 10\bar{1}0 \rangle$ interface, the polar NiO surface is the most favorable pairing with all ZnO surfaces.

The strain distribution of this system approaches the conditions of ZnO deposited on NiO. Under these conditions, by the energy minimization principles of Wulff construction, it may be predicted that, for the NiO-$\langle 100 \rangle$ and NiO-$\langle 110 \rangle$ interfaces, the ZnO-$\langle 10\bar{1}0 \rangle$ and ZnO-$\langle 11\bar{2}0 \rangle$ arrangements of the ZnO structure, respectively, would preferentially form. For the NiO-$\langle 111 \rangle$ surface, the $\langle 111 \rangle - \langle 000\frac{1}{2} \rangle$ Ni-O and Zn-O interfaces are predicted to predominantly form, in agreement with experimental evidence.[163]

Nonpolar-Nonpolar Interfaces

Of the four nonpolar-nonpolar interfaces, three of them are the least energetically favorable overall. The interfaces exhibit the greatest dependence on the relative alignment of the respective surfaces on structural relaxation and interface states, and exhibit behaviors not observed in the interfaces involving at least one polar surface.

$\langle 100 \rangle$ *Interfaces*

The two nonpolar-nonpolar interfaces that include the NiO-$\langle 100 \rangle$ surface exhibit relatively similar traits. The relaxed structures of the $\langle 100 \rangle$ - $\langle 10\bar{1}0 \rangle$ and $\langle 100 \rangle$ - $\langle 11\bar{2}0 \rangle$ interfaces are shown in Figure 5-29:

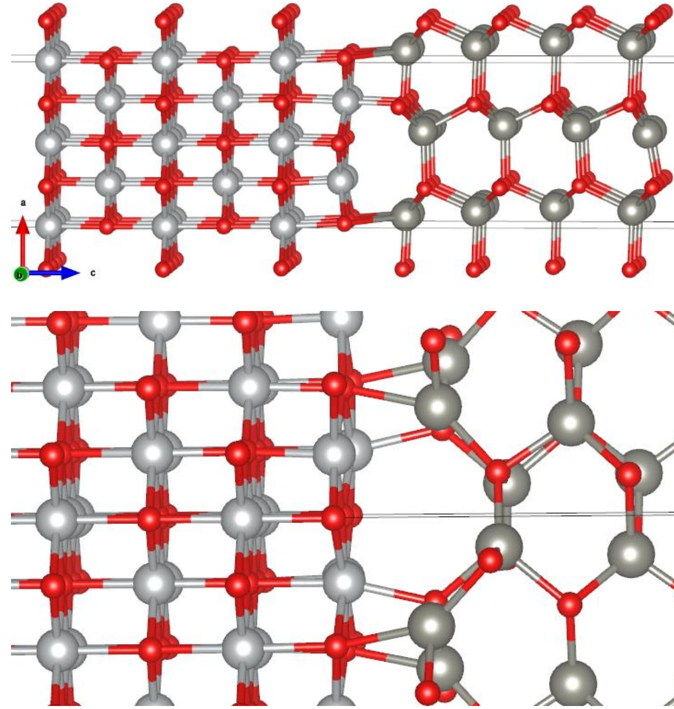

Figure 5-29 Top: Relaxed structure of the $\langle 100 \rangle$ - $\langle 10\bar{1}0 \rangle$ interface. Bottom: Relaxed structure of the $\langle 100 \rangle$ - $\langle 11\bar{2}0 \rangle$ interface. The structure of NiO and ZnO are to the left and right respectively, for both images.

The $\langle 100 \rangle$ - $\langle 10\bar{1}0 \rangle$ structure aligns itself such that the cat- and anion rows of the surface layer are completely parallel and the oxygen ions of the ZnO structure are arranged directly across the interface from the nickel ions, with a bond length of 2.05 Å. The terminal zinc ions bond with their own row of oxygen ions within the NiO structure, but the alignment across the junction is staggered, so the bonding strength is lower. The bond lengths are 2.61Å, beyond what would normally be considered bonded, but the relaxed structure clearly indicates attraction. The ions that are involved in the cross-junction bonding extend out from the bulk of their respective surfaces, and towards the opposite surface.

The $\langle 100 \rangle$ - $\langle 11\bar{2}0 \rangle$ interface arranges in a similar manner to the $\langle 100 \rangle$ - $\langle 10\bar{1}0 \rangle$ interface. The ab-plane positions of the bonding ions do not line up across the junction, however, so the bonds are all angled, causing the $\langle 11\bar{2}0 \rangle$ surface to be further distorted from the bulk structure than observed in other interfaces, although the applied strain also plays a role. The bonds across the interface bonds have lengths of 2.13 Å and 2.24 Å, for the Ni-O and Zn-O bonds, respectively.

The spatially resolved hybrid DOS of the ⟨100⟩ - ⟨10$\bar{1}$0⟩ and ⟨100⟩ - ⟨11$\bar{2}$0⟩ interfaces exhibit similar traits for the electronic structure throughout the structure, as may be observed in Figure 5-30.

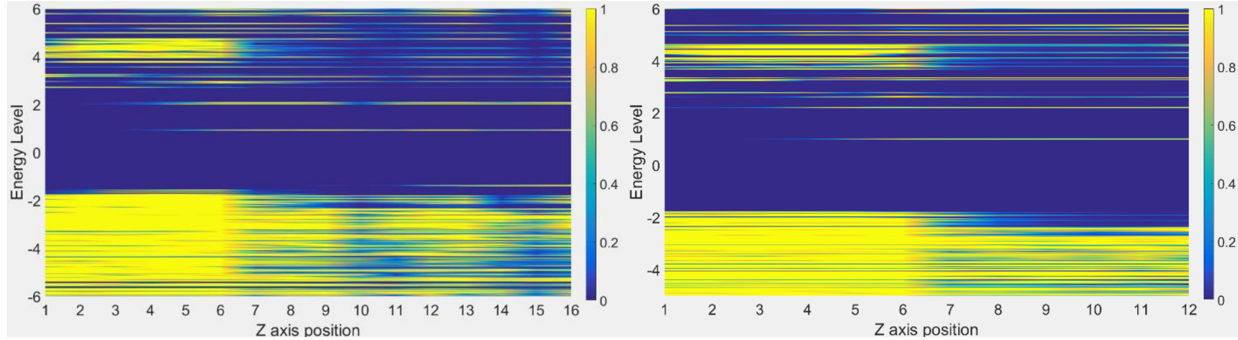

Figure 5-30 Left image: Spatially resolved DOS of the ⟨100⟩ - ⟨10$\bar{1}$0⟩ interface. Right image: Spatially resolved DOS of the ⟨100⟩ - ⟨11$\bar{2}$0⟩ interface. Both calculated with the hybrid functional utilizing 25% exact exchange. NiO is on the left side, ZnO is on the right side. The interface transition occurs along c-axis 6-7.

A particular trait is observed in both structures, which henceforth will be referred to as invasive states. At energies corresponding to about 1 and 2 eV in both images, states that are present throughout the ZnO slab continue several ionic layers into the NiO surface. These states diminish the further into the opposite slab, and with distance from the interface, so they are not native to the NiO DOS structure, yet they appear within the structure regardless.

The presence of invasive states shows the ZnO material to have a considerable influence on its electronic structure in the immediate vicinity of the interface. The presence of invasive states in this interface acts as mid-gap states within the NiO band structure, reducing the effective band gap around the immediate interface region. In applications such as solar cells, these states would act as charge carrier traps and recombination facilitators, lowering overall efficiency.

The GGA+U functional DOS exhibits different features; however, the overall structure of the interface agrees with the hybrid results.

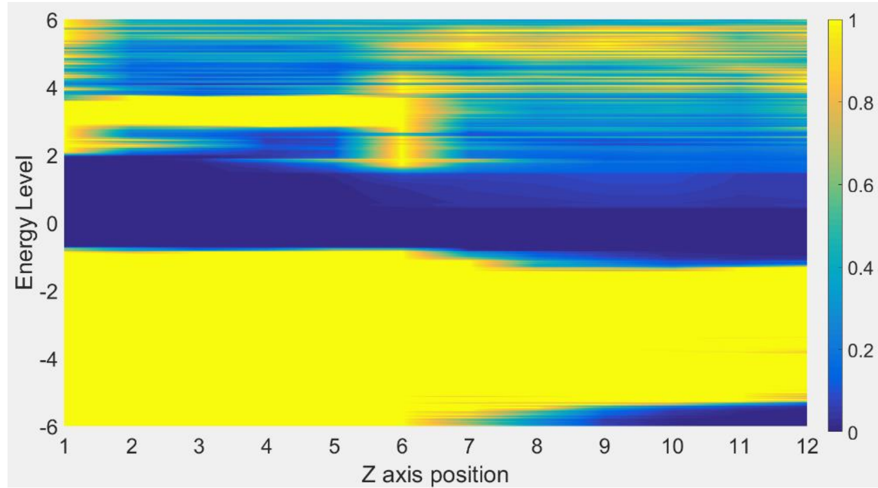

Figure 5-31 Spatially resolved DOS of the ⟨100⟩ - ⟨11$\bar{2}$0⟩ *interface, calculated with the GGA+U. NiO is on the left side, ZnO is on the right side. The interface transition occurs along z-axis position 6-7.*

The main difference, apart from the underestimation of the band gaps, is the appearance of interface states at the NiO surface. These appear for most NiO surfaces, however for the ⟨100⟩ interfaces, the energy level of the NiO interface states is higher than the predicted CBM of ZnO, so the states of the latter dominate the effective CBM at the interface.

⟨110⟩ - ⟨10$\bar{1}$0⟩ *Interface*

The ridged structure of the NiO-⟨110⟩ surface results in more extensive differences in interface bonding and electronic structure between separate interfaces, hence the ⟨110⟩ - ⟨10$\bar{1}$0⟩ and ⟨110⟩ - ⟨11$\bar{2}$0⟩ interfaces are explained separately. The relaxed structure of the ⟨110⟩ - ⟨10$\bar{1}$0⟩ interface is shown in Figure 5-32:

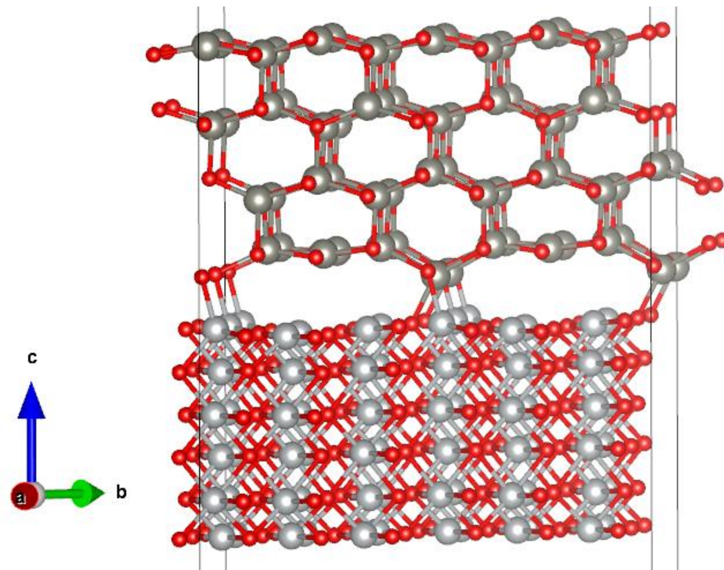

Figure 5-32 The relaxed structure of the ⟨110⟩ - ⟨10$\bar{1}$0⟩ interface. The structure of NiO and ZnO are to the bottom and top respectively.

The cross-interface bonding has a different effect on the NiO and ZnO structures: The ZnO structure approaches closer to the bulk arrangement in the bonded regions, while the NiO structure is distorted. Upon the formation of the interface bonds, the ZnO ions are bonded to two adjacent ions at the NiO surface ridge peaks, with the NiO ions approaching closer to the ZnO lattice positions than NiO. The Ni-O and Zn-O bond lengths are nearly equivalent, with a bond length around 1.99 Å. The cross-interface bonds are notably stronger than the Ni-O bonds along the NiO surface ridges.

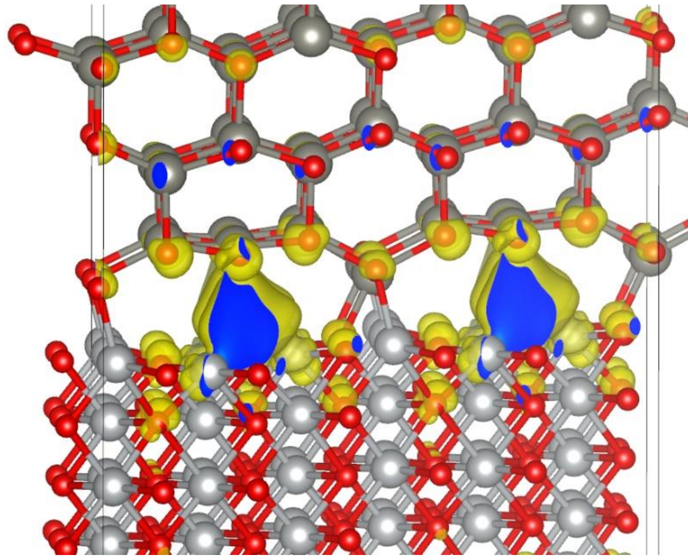

Figure 5-33 Partial charge density of the $\langle 110 \rangle$ - $\langle 10\bar{1}0 \rangle$ *interface, corresponding to the CBM energy. Isosurface density level at 0.001.*

As seen in Figure 5-33, the vacuum regions do not act as an insulating layer, but rather as an electron trap region, providing the lowest energy conduction band across the interface. Conversely, the highest energy valence bands in the ZnO structure are located at the cross interface bonded regions, forming a structure where electrons and holes are trapped in separate regions of the interface. Rather than the specific structure of the orbitals, the more important point to note is rather the effect of the cross-interface bonding, and alternately the lack thereof, on the electronic structure. This is also demonstrated by the spatially resolved DOS of the $\langle 110 \rangle$-$\langle 10\bar{1}0 \rangle$ interface, shown in Figure 5-34:

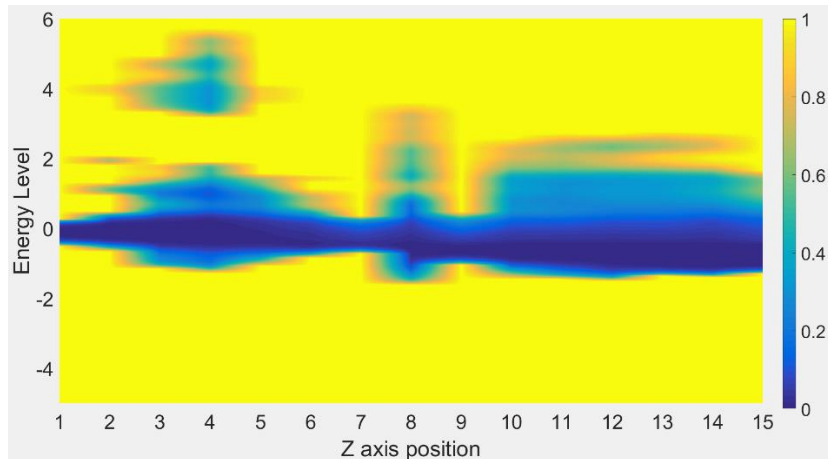

Figure 5-34 Spatially resolved DOS of the ⟨110⟩ - ⟨10$\bar{1}$0⟩ *interface, calculated with the GGA+U functional. NiO is on the left side, ZnO is on the right side. The interface transition occurs along z-axis position 7-8. The "resolution" is somewhat lower than other GGA+U DOS images due to computer hardware constraints.*

The ⟨110⟩ slab displays considerable surface states, both towards the vacuum surface and the interface, reducing the effective band gap to about 0.7 eV on the surface, and 1.0 eV at the interface. At z-axis value 8 in the figure, the DOS of the bonding ZnO ions are isolated from the rest of the ZnO slab states. These bonding interface ions assume an electronic state closer to ZnO bulk, compared to the non-bonding surface ions.

Considering Figure 5-33 and Figure 5-34 together, the interface width, as well as the extent and density of the interface bonding, may be considered among the determining factors in formation of interface states in the NiO – ZnO interface.

⟨110⟩ - ⟨11$\bar{2}$0⟩ *Interface*

The ⟨110⟩ - ⟨11$\bar{2}$0⟩ interface structure, shown in Figure 5-35, follows the general bonding arrangement of the nonpolar-nonpolar interfaces. It may be observed, however, that the non-bonding interface ions are significantly repelled by the electrostatic interactions, as the ions directly adjacent the bonding ions in the ZnO structure line up with equally charged ions.

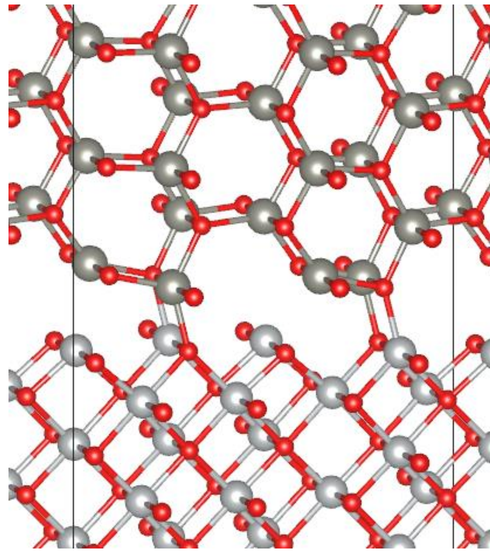

Figure 5-35 The relaxed structure of the ⟨110⟩ - ⟨11$\bar{2}$0⟩ interface. The structure of NiO and ZnO are at the bottom and top respectively.

The bonds that do form are relatively strong, sufficient to make the interface formation energy favorable despite the lineup of equally charged ions. The cross-interface bond length is 2.00 Å, an intermediate between ZnO and NiO. The applied strain on this surface requires special mention, as the original tetrahedral coordination of the ions in the wurtzite structure has been warped into a trigonal bipyramidal arrangement. Despite the considerable rearrangement, the structure of the relaxed slab is intact, with no bond failures or local distortions.

The spatially resolved DOS of the ⟨110⟩ - ⟨11$\bar{2}$0⟩ interface is shown in Figure 5-36:

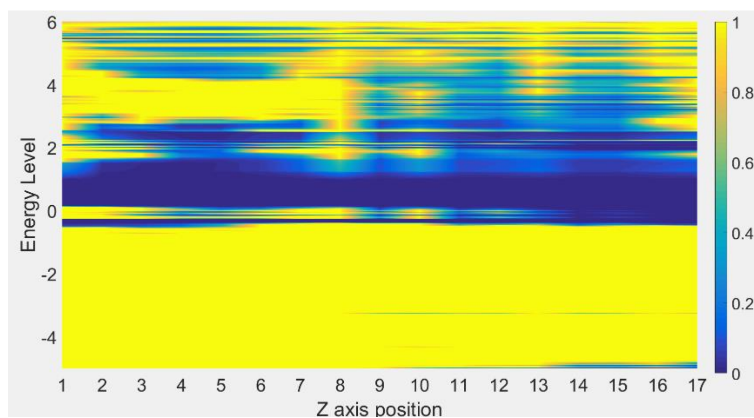

Figure 5-36 Spatially resolved DOS of the ⟨110⟩ - ⟨11$\bar{2}$0⟩ interface, calculated with the GGA+U functional. NiO is on the left side, ZnO is on the right side. The interface transition occurs along z-axis position 8-9.

Located around energy level zero, the opposite case of the invasive states of the ⟨100⟩ interfaces are observed, with the valence band states of NiO continuing extensively into the ZnO slab. The states persist to the ZnO vacuum surface layer. These valence band states are unique to the ⟨110⟩ surface and are also observed for the isolated surface.

The interface states at the valence band are composed of oxygen dangling bonds at the interface, both from the NiO and the ZnO interface ions, while the conduction band interface states is due to the same surface state orbitals of nickel that are observed in the clean NiO-⟨110⟩ surface. The spatial expansion of the surface states are somewhat distorted, as the nickel ions that are bonded with oxygen ions in the ZnO surface and do not form surface states, or have them shifted to a higher energy.

It should be noted that neither of the surfaces in this interface are equivalent along the a- and b-axes, so an interface formed by rotating either surface by 90 degrees would exhibit significantly different bonding patterns, and possibly different interface states.

Polar-Polar Interfaces

Compared to the nonpolar-nonpolar interfaces, where the optimal relative conformation is dominated by alignment of oppositely charged individual ions, the interfaces that involve two polar surfaces bond in a manner primarily dominated by the electrostatic interactions of the surfaces as entireties. Consequently, the specific conformations are less important to the energetic favorability of the interfaces.

⟨111⟩ - ⟨0001⟩ *Interfaces*

The ⟨111⟩ - ⟨0001⟩ interfaces are technically polar-polar, but due to the surface relaxation and the applied strain, the ZnO surface approaches a non-polar structure. This is also observed in the interface formation energy, where the ⟨111⟩ - ⟨0001⟩ formation energies matches the polar-nonpolar interface energies closed than the polar-polar. The relaxed structures of the ⟨111⟩ - ⟨0001⟩ interfaces are shown in Figure 5-37:

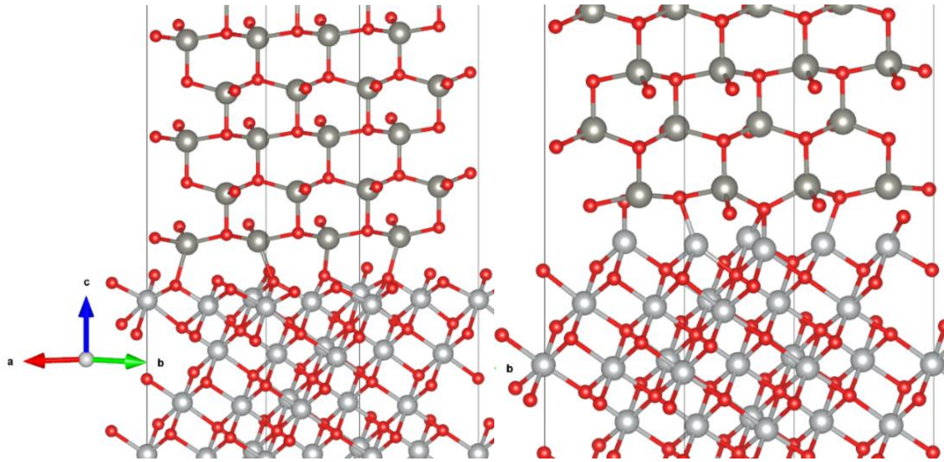

Figure 5-37 The relaxed structure of the ⟨111⟩ - ⟨0001⟩ interfaces. The structure of NiO and ZnO are at the bottom and top respectively.

The relaxed configuration of the ZnO termination ions generally approaches a planar surface, however the closer the ionic position in the ab-plane is a lattice position of the opposite NiO structure, the greater the bond strength with the NiO lattice, and the more extensive the interface modification to the ZnO.

Due to the presence of the two oppositely arranged internal dipoles of the slabs, the spatially resolved DOS structure of the ⟨111⟩ - ⟨0001⟩ interfaces, shown in Figure 5-38, display significant energy shifts.

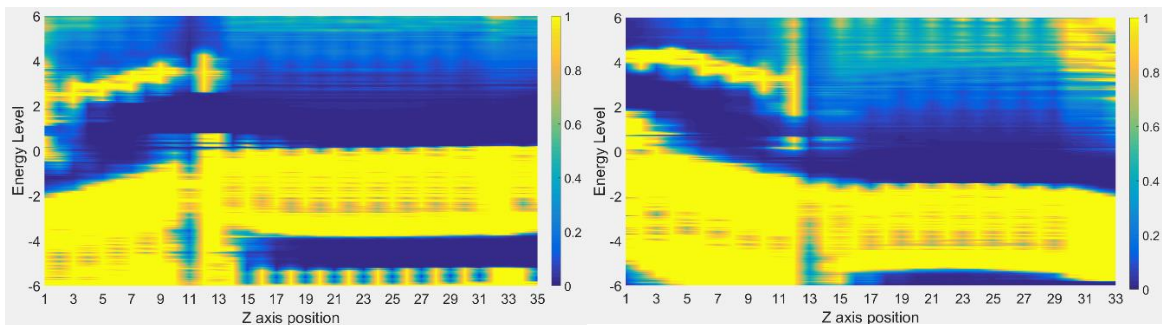

Figure 5-38 Spatially resolved DOS of the ⟨111⟩ - ⟨0001⟩ interfaces, calculated with the GGA+U functional. NiO is on the left side, ZnO is on the right side. Left image: Zn-O interface. Right image: Ni-O interface. The interface transition occurs along z-axis position 10-11 for the left image, and 12-13 for the right.

Both combinations of interface surfaces similarly display considerable interface states in the band gap. Between the two different terminations, the origin of the mid-gap states differs: The Zn-O interface predominantly displays valence band mid-gap states, while only conduction band

mid-gap states occur at the Ni-O interfaces. The Zn-O interface states are dominated by O-2p states of the first sub-surface layer oxygen ions. As the valence band surface states are not observed in the isolated surfaces (Figure 5-23), they appear to be a consequence of the presence of the NiO slab and the applied strain.

The mid-gap states at the Ni-O interface are the same surface states observed on the nickel termination surface both in isolated surfaces and at the nickel termination surface in the Zn – O interface. Compared to at the vacuum surface, the interface nickel mid-gap states energy range is considerably smaller, the reason for which is explained in the subsequent section.

$\langle 111\rangle$ - $\langle 000\frac{1}{2}\rangle$ *Interfaces*

Compared with the $\langle 111\rangle$ - $\langle 0001\rangle$ interfaces, the $\langle 111\rangle$ - $\langle 000\frac{1}{2}\rangle$ interfaces are very similar. Beyond the monolayer of the more exposed termination ions, the ZnO surface slab is, prior to ionic relaxation, identical to the $\langle 0001\rangle$ surface. This difference still causes significant alterations in the structure, both electronic and ionic, at the interface. The relaxed structure of the $\langle 111\rangle$ - $\langle 000\frac{1}{2}\rangle$ interfaces are shown in Figure 5-39:

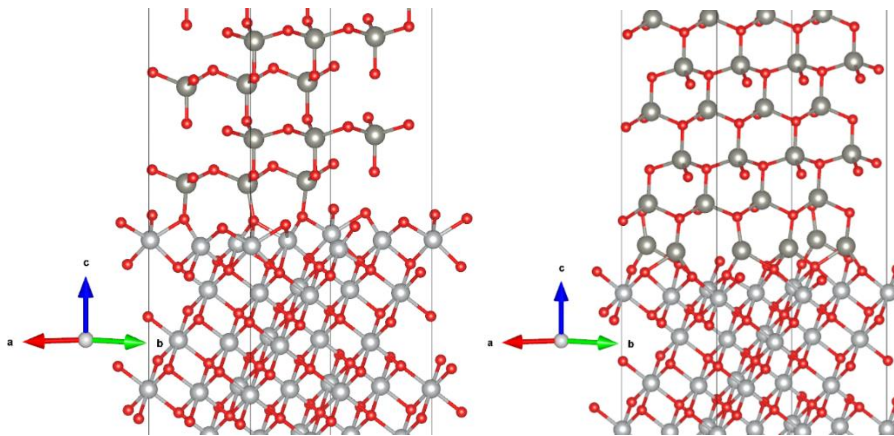

Figure 5-39 The relaxed structure of the $\langle 111\rangle$ - $\langle 000\frac{1}{2}\rangle$ interfaces. Left image: Ni-O. Right image: Zn-O. The structure of NiO and ZnO are at the bottom and top respectively.

The termination ions of the ZnO structure are displaced in separate directions, assuming lattice positions at the NiO surface. These interfaces thus assume a tightly bonded interface between the

different materials. Due to a difference in the density of lattice sites in the ab-plane, a fraction of the NiO lattice sites remains unoccupied, resulting in a partially occupied intermediate layer between the surfaces.

The spatial DOS structures are similar to the $\langle 111 \rangle$ - $\langle 0001 \rangle$ interfaces, but with few significant differences at the interface itself. The spatially resolved DOS of the $\langle 111 \rangle$ - $\langle 000\frac{1}{2} \rangle$ interfaces are shown in Figure 5-40:

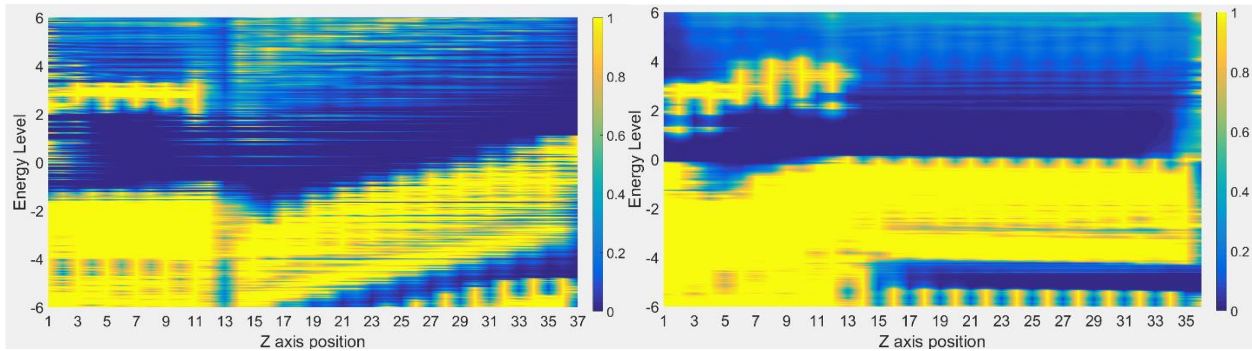

Figure 5-40 Spatially resolved DOS of the $\langle 111 \rangle$ - $\langle 000\frac{1}{2} \rangle$ interfaces, calculated with the GGA+U functional. NiO is on the left side, ZnO is on the right side. Left image: Zn-O interface. Right image: Ni-O interface. The interface transition occurs along z-axis position 12-14 for the left image, and 11-12 for the right. Due to computer hardware limitations, the left DOS has a lower "resolution".

The cation surface of the Ni-O interface displays some gap states near the conduction band, but the ZnO interface layer has a completely clean gap. It is notable that the nickel termination surface states that that are common for the both the clean surface and several interfaces are nearly completely non-existent in this interface. It is likely that, due to the relatively unique structure of the ZnO slab with terminal oxygen ions highly exposed, and the unique bonding at the $\langle 111 \rangle$ - $\langle 000\frac{1}{2} \rangle$ interfaces, that the interaction with the ZnO surface alters the electronic structure of the NiO surface sufficiently close to either the bulk or the oxygen termination surface structure, that the NiO surface states don't form throughout the gap. It is a recurring observation that nickel surface ions involved in cross-interface bonding does not form surface states; this interface would appear to be the most extensive case, where the termination ions are all at least partially bonded. The same effect is likely the cause of the restricted energy range of the $\langle 111 \rangle$ - $\langle 0001 \rangle$ Ni-O interface states, although to a lesser extent due to the weaker cross interface bonding.

Between Figure 5-38 and Figure 5-40, the results indicate that, for the polar-polar interfaces, the interface states present in a physical junction may be manipulated, both by selection of which slab contributes which ion termination, but also by the specific bonding arrangements at the interface.

Polar-Nonpolar Interfaces

The polar-nonpolar interfaces display a mix of traits of both the polar-polar and nonpolar-nonpolar interfaces. Between the two component surfaces, however, the polar NiO surface dominates the general behavior. The $\langle 111 \rangle$ - $\langle 10\bar{1}0 \rangle$ and $\langle 111 \rangle$ - $\langle 11\bar{2}0 \rangle$ interfaces act in similar manners, so both will be addressed together. The relaxed structure of the $\langle 111 \rangle$ - $\langle 10\bar{1}0 \rangle$ interfaces are shown in Figure 5-41.

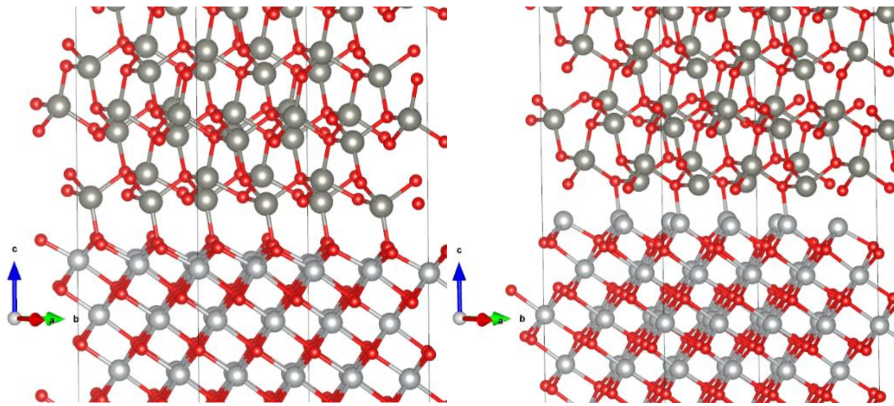

Figure 5-41 The relaxed structure of the $\langle 111 \rangle$ - $\langle 10\bar{1}0 \rangle$ interfaces. The structure of NiO and ZnO are at the bottom and top respectively.

The relaxed structures remain close to the bulk structure. The structures align in the ab-plane such that the bonding ions form an intermediate position between the ideal bonding angle of NiO, and a maximal interface width. Between the two interface arrangements, there is a slight difference in the interface width, at 1.95 Å and 1.92 Å for the nickel- and oxygen polar interfaces, respectively.

The $\langle 111 \rangle$ - $\langle 11\bar{2}0 \rangle$ interfaces act in a similar manner. The main difference is observed in the Ni-O interface, where the ZnO surface oxygen ions that are sufficiently close to the NiO oxygen

lattice sites are displaced significantly further towards the NiO surface and assuming a bonding structure closer to NiO than ZnO. This would likely also occur in the ⟨111⟩ - ⟨10$\bar{1}$0⟩ interfaces, but the surface structures match up with the same number of ions in this case, so the effect is not observed.

The polar-nonpolar interfaces display the greatest difference in interface state density between the different ion termination arrangements. The spatially resolved DOS is shown in Figure 5-42:

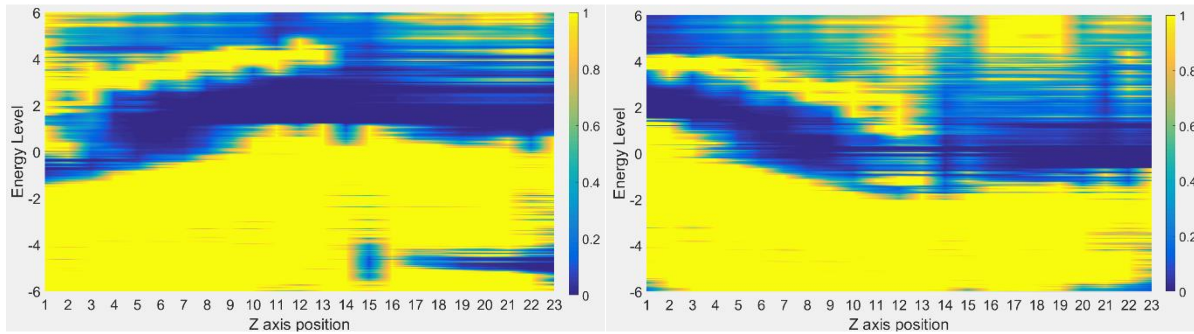

Figure 5-42 Spatially resolved DOS of the ⟨111⟩ - ⟨10$\bar{1}$0⟩ interfaces, calculated with the GGA+U functional. NiO is on the left side, ZnO is on the right side. Left image: Zn-O. Right image: Ni-O. The interface transition occurs along z-axis position 13-14 for the left image, and 12-13 for the right.

Unlike for the polar-polar interfaces, the interface effects of the polar nickel termination are not counteracted by bonding with ions on an oppositely charged polar ZnO surface. Consequently, the nickel surface states form relatively uninhabited at the Ni-O interface, forming a continuous band of states across the band gap (see Figure 5-43). For the opposite surface arrangement, the ZnO conduction band surface states cannot form due to the oxygen ions on the NiO surface, resulting in an interface free of conduction band states. Due to the low extent of interface bonding, there are significant valence band states present, however. The ⟨111⟩ - ⟨11$\bar{2}$0⟩ interfaces behave in a mostly identical manner, although the Zn-O interface valence band states lie slightly higher in energy.

The polar-nonpolar Ni-O interfaces display a particular trait of interest in the spatial expansion of the interface states, shown in Figure 5-43:

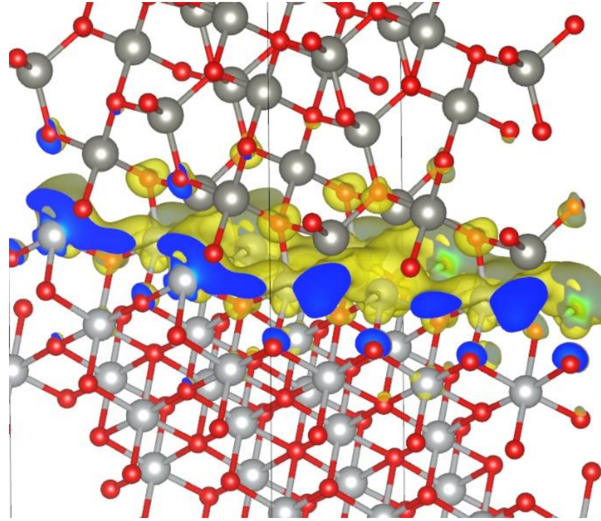

Figure 5-43 Partial charge density of the $\langle 111 \rangle$ - $\langle 10\bar{1}0 \rangle$ *Ni-O interface. The energy level corresponds to the mid-gap interface states of Figure 5-42 (right image), with an isosurface level of 0.0007.*

The conduction band states of the Ni-O interface cover the entirety of the interface in spatially continuous states. As the interface states also cover the energy range of entire band gap overlap, a consequence of this property is electronic conduction parallel to the interface. In a system where interface boundaries are prevalent throughout the structure, such as in a nanocomposite material, such states could significantly enhance conductivity, although the extent to which the polar-nonpolar Ni-O interfaces are present would be an important factor in the extent of the effect.

Overall Comparisons

Interface Charge Density

The overall charge density, in absolute and relative values compared to the surrounding slabs, as well as the induced charge density are given in Table 5-9:

Table 5-9 Interface charge density values for ionically relaxed, strained ZnO interfaces. The relative interface density columns is the relative density between the mid-interface density and bulk NiO/ZnO charge minima. The relative induced interface density is the relative difference between the sum of the separate NiO and ZnO contributions, and the total interface density.

Interface	Absolute interface density (charge/Å^3)	Relative interface density NiO (%)	Relative interface density ZnO (%)	Relative induced interface density (%)
$\langle 100 \rangle$ - $\langle 10\bar{1}0 \rangle$	0.1251	67.33	77.61	5.13
$\langle 100 \rangle$ - $\langle 11\bar{2}0 \rangle$	0.1163	62.39	54.91	2.37
$\langle 110 \rangle$ - $\langle 10\bar{1}0 \rangle$	0.1137	27.24	83.91	3.44
$\langle 110 \rangle$ - $\langle 11\bar{2}0 \rangle$	0.1277	32.69	51.85	2.39
$\langle 111 \rangle$ - $\langle 0001 \rangle$ Ni-O	0.1279	24.34	104.84	-12.75
$\langle 111 \rangle$ - $\langle 0001 \rangle$ Zn-O	0.2570	50.54	213.28	4.00
$\langle 111 \rangle$ - $\langle 000\frac{1}{2} \rangle$ Ni-O	No Interface			
$\langle 111 \rangle$ - $\langle 000\frac{1}{2} \rangle$ Zn-O	No Interface			
$\langle 111 \rangle$ - $\langle 10\bar{1}0 \rangle$ Ni-O	0.1721	34.96	96.63	11.49
$\langle 111 \rangle$ - $\langle 10\bar{1}0 \rangle$ Zn-O	0.1159	22.56	67.19	32.24
$\langle 111 \rangle$ - $\langle 11\bar{2}0 \rangle$ Ni-O	0.2688	51.33	95.76	4.72
$\langle 111 \rangle$ - $\langle 11\bar{2}0 \rangle$ Zn-O	0.1134	21.85	41.98	24.88

The polar-nonpolar Zn-O interfaces exhibit the greatest relative induced charge density at the interface by a significant factor. The lack of polarity on the ZnO surfaces, and thus lack of an oppositely oriented dipole field to lead the charge away from the center, combined with the negatively charged oxygen termination of the NiO surface are likely the cause of the high relative induced charge density. It should be noted that the absolute value of the interface charge is also relatively low, so while the induced charge is comparably more important, the absolute magnitude is relatively less. Apart from the continuous interfaces, the Ni-O termination polar-nonpolar interfaces display the greatest absolute scale interface charge density.

For the $\langle 111 \rangle$ - $\langle 0001 \rangle$ interfaces, the interfacial charge density is relatively high: equal to or higher than the charge density minima within the ZnO surface. The $\langle 111 \rangle$ - $\langle 000\frac{1}{2} \rangle$ interfaces display no interface minima from the charge density distribution, but rather a continuous transition from the NiO to the ZnO surface, due to the tight bonding formed between the surfaces.

Most interfaces display a relatively disorderly planar averaged induced charge distribution. The exceptions are the NiO-$\langle 100 \rangle$ interfaces, which display a continuous induced charge density, shown in Figure 5-44:

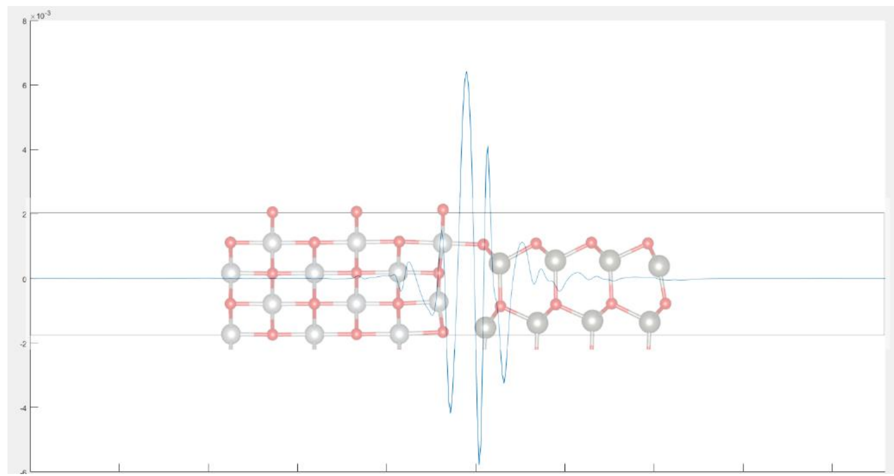

Figure 5-44 Strained ZnO $\langle 100 \rangle - \langle 10\bar{1}0 \rangle$ relaxed surface with induced charge plot. Each y-axis tick has magnitude $2*10^{-3}$.

There is a clear spike in the induced charge density around the center of the interface gap, drawn from the surface states of the NiO slab, as well as the first and second layers of the ZnO slab. Other interfaces do not display such a simple induced charge behavior and tend to display a rather chaotic curve, indicating a more complex charge rearrangement in these cases.

Interface Band Alignment

The alignment between the NiO and ZnO surfaces displays considerable variance with respect to the nature of the interface in question, as well as the strain applied to the system. An overview of the VBM offsets for the various surfaces are given in Table 5-10:

Table 5-10 Band offset between strained ZnO interfaces. Positive VBM offset corresponds to the NiO VBM level being located higher in energy than the ZnO levels.

Interface NiO Surface – ZnO Surface	VBM Offset GGA+U (eV)	VBM Offset Mixed (eV)
$\langle 100 \rangle$ - $\langle 10\bar{1}0 \rangle$	0.43	1.85
$\langle 100 \rangle$ - $\langle 11\bar{2}0 \rangle$	-0.22	1.20
$\langle 110 \rangle$ - $\langle 10\bar{1}0 \rangle$	0.31	1.73
$\langle 110 \rangle$ – $\langle 11\bar{2}0 \rangle$	0.92	2.34
$\langle 111 \rangle$ - $\langle 0001 \rangle$ Nickel - Oxygen	-0.72	0.12
$\langle 111 \rangle$ - $\langle 0001 \rangle$ Zinc - Oxygen	-0.93	0.49
$\langle 111 \rangle$ - $\langle 000\frac{1}{2} \rangle$ Nickel - Oxygen	-1.29	0.70
$\langle 111 \rangle$ - $\langle 000\frac{1}{2} \rangle$ Zinc - Oxygen	0.09	1.51
$\langle 111 \rangle$ - $\langle 10\bar{1}0 \rangle$ Nickel - Oxygen	-0.55	0.87
$\langle 111 \rangle$ - $\langle 10\bar{1}0 \rangle$ Zinc - Oxygen	0.31	1.73
$\langle 111 \rangle$ - $\langle 11\bar{2}0 \rangle$ Nickel - Oxygen	0.06	1.48
$\langle 111 \rangle$ - $\langle 11\bar{2}0 \rangle$ Zinc - Oxygen	-0.27	1.15

The nonpolar-nonpolar interfaces exhibit the greatest average offset, while the $\langle 110 \rangle$ – $\langle 11\bar{2}0 \rangle$ interface in particular displays the greatest offset overall, by a significant margin. This divergence is partly due to the shear strain applied to the zinc slab: the zinc ions at the bulk assume a trigonal bipyramidal coordination with the surrounding oxygen ions. Such a rearrangement likely causes significant changes in the environment of the ZnO bulk material properties.

The polar-polar interfaces exhibit the opposite behavior, displaying the smallest band offsets overall. Within this group, the $\langle 0001 \rangle$ and $\langle 000\frac{1}{2} \rangle$ surfaces also display distinctly different offsets, with the former displaying overall smallest offsets. This behavior of the $\langle 0001 \rangle$ interfaces is unexpected, as the relaxed ionic structures and interface formation energies are closer to those of the polar-nonpolar interfaces, which display intermediate values between the two other groups.

The results indicate that, for a thin film system of ZnO deposited on NiO of any arrangement, engineering of the band offset by the variables in these results: surface arrangement and

termination ion on the polar surfaces, are both potential options, as the calculated offset variance is considerable. The effects of strain are discussed in the section for static interfaces.

5.4.3. Static Structure Interfaces

While it varies with the surface in question and the type of the applied strain, the strained NiO structures are relatively structurally unstable, compared with the strained ZnO. Ionic relaxation in several cases causes systematic structural failure such as periodic cavities throughout the surface slabs due to bond dissociation or other modes of systematic structural distortion. Hence, the static interfaces without ionic relaxation will be considered in this section.

Interface Formation Energy

Without ionic relaxation, the interface formation energies differ from the relaxed interface values. The strained ZnO interface energies with both relaxed and static slabs are shown in Figure 5-45:

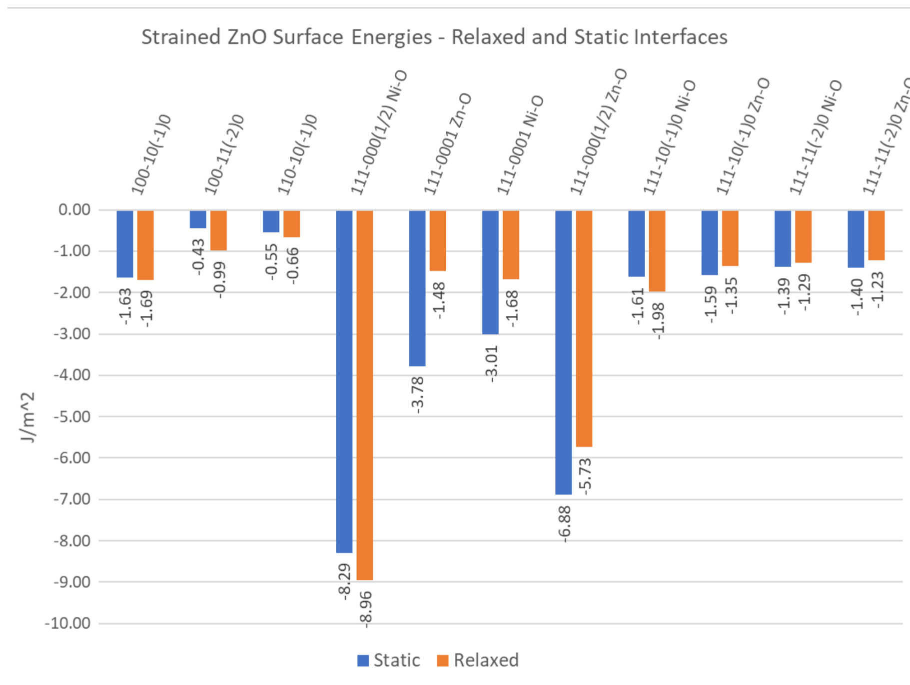

Figure 5-45 Interface energies for relaxed and static interfaces with strained ZnO slabs.

Without relaxation, the qualitative picture of the strained ZnO interfaces remain largely the same. The greatest difference is observed for the ⟨111⟩ - ⟨0001⟩ interfaces, where the interface formation energy is considerably more negative compared to the relaxed surfaces, due to the static interfaces retaining the greater polarity of the bulk arrangement.

While there are no overall patterns in the differences between the static and relaxed strained ZnO interface energies, the general qualitative agreement and relatively small differences for most interfaces evidence that the static strained NiO interface energies are sufficiently accurate to provide a qualitative view of the relative favorability of each interface. The interface formation energies are shown in Figure 5-46:

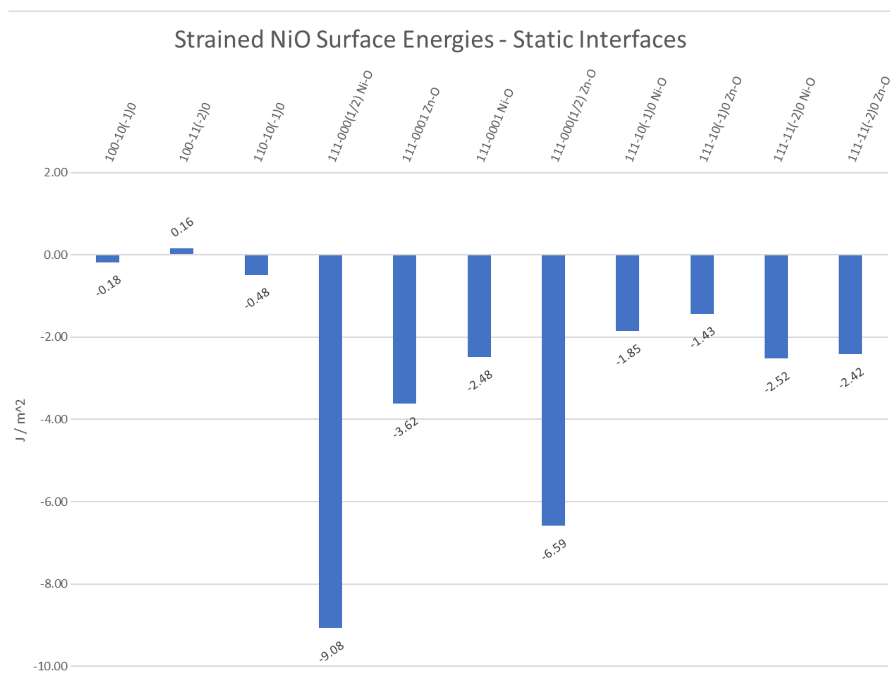

Figure 5-46 Interface formation energy for interfaces with strained NiO. The ⟨110⟩-⟨11$\bar{2}$0⟩ *surface is excluded, as the magnetic structure collapsed during electronic convergence for the static surface, giving wrong interface energies.*

Compared to the static interfaces with strained ZnO slabs, several interfaces display more positive interface formation energies. The interface formation energies with the greatest relative increase are the interfaces under the most strain. The interfaces with intermediate to low degree of strain display approximately equal formation energy, or lower. The effect on the interface energy with the strain distribution also depends on the surfaces in question.

By the energy minimization principles of Wulff construction, upon deposition of NiO on any considered ZnO surface, an interface including the ⟨111⟩ surface of NiO is predicted to form, a behavior which has also been reported experimentally.[6,134]

Interface Characteristics

Application of the strain to the NiO structure rather than the ZnO causes considerable changes both to the to the interface states, but also to the electronic structure in general. The general behavior of each group of interfaces remain generally constant with a different strain distribution, although certain significant differences are observed. The effects of the strain distribution are, however, generally consistent across the different interfaces.

While the ⟨100⟩ - ⟨10$\bar{1}$0⟩ interface is among the less energetically stable interfaces, the simplicity of the spatial DOS structures, shown in Figure 5-47, provides a clear example of the effects of changing the strain distribution.

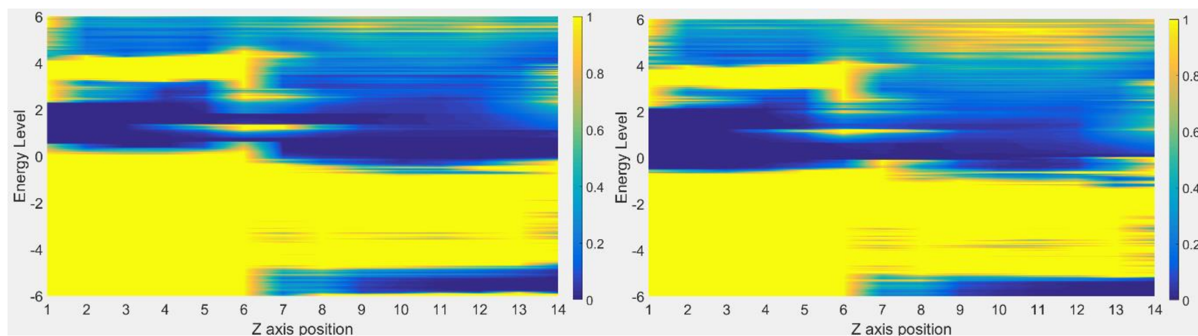

Figure 5-47 Spatially resolved DOS of the ⟨100⟩ - ⟨10$\bar{1}$0⟩ interface with strained NiO and ZnO structures, to the left and the right respectively. The states corresponding to the NiO slab are on the left side of the diagram, while the states corresponding to ZnO are to the right, with the transition being at z-axis 6-7 for both.

In the DOS for the strained NiO interface (left image), the strain free ZnO slab has a considerably wider band gap compared to the strained slab. Contrarily, the NiO band gap is reduced in width. The decrease in ZnO gap states is partly due to the lack of strain but the lack of ionic relaxation also contributes to the absence of mid-gap states in the ZnO DOS.

The strained NiO slab displays considerable surface states at the valence band near the vacuum surface. The interface states form at both the conduction and valence bands, but also in the center

of the band gap. The nature of this gap state may be seen clearly in the partial charge density structure of the interface, see Figure 5-48.

In the strained ZnO interface, the band gap of NiO is wider, while the ZnO slab displays extensive density of mid-gap states. Two separate regions of interface states are present in the strained ZnO DOS structure. Between the two DOS structures, it may be established that the interface states at the valence band are formed by both the NiO $\langle 100 \rangle$ and ZnO $\langle 10\bar{1}0 \rangle$ surfaces, but only whichever of the two is strained.

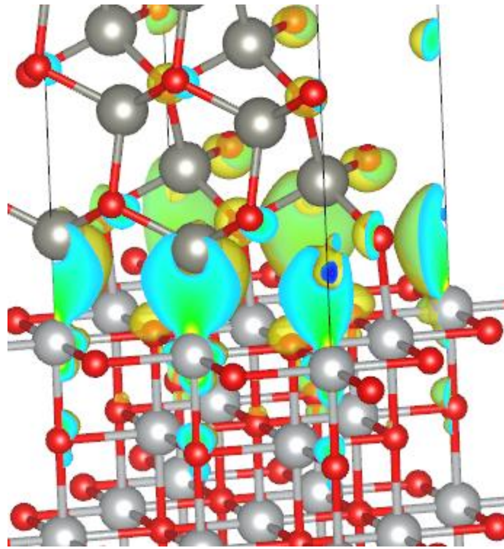

Figure 5-48 Partial charge density of the strained NiO $\langle 100 \rangle$-$\langle 10\bar{1}0 \rangle$ interface, corresponding to the mid-gap density states. Calculated with hybrid functional, utilizing standard exact exchange.

As previously noted in section 5.4.2, the strained ZnO interface lowest energy mid-gap interface states originate from ZnO structure. The strained NiO interface exhibits a different origin of the lowest energy states. The reason is likely twofold: Because the strain free ZnO structure cannot form the conduction band states perpendicular to the $[0001]$ direction of ZnO at a sufficiently low energy with the strain on the structure removed, and because the interface structure lines up the terminal zinc- and nickel ions (Figure 5-48), causing the former to attract the surface state orbitals of the nickel ion. The latter point also affects the energy level of the mid-gap states, forming lower energy states as the orbitals are bound by the positive electrostatic field in between both termination ions.

Band Alignments: Strain Distribution and Strain Corrected Values

For the static interfaces, the strain corrected values for the band offsets, otherwise known as the natural band offsets, have been calculated in addition to the strained offsets:

Table 5-11 Natural and strained valence band offsets for static interfaces.

Interface	Strained Band Offsets (GGA+U)		Strained Band Offsets (Mixed)		Natural VBM Band Offsets (GGA+U)	Natural VBM Band Offsets (Mixed)
	Strain NiO	Strain ZnO	Strain NiO	Strain ZnO		
$\langle 100\rangle$ - $\langle 10\bar{1}0\rangle$	-0.24	-0.22	1.18	1.20	0.032	1.45
$\langle 100\rangle$ - $\langle 11\bar{2}0\rangle$	-2.18	-0.98	-0.76	0.44	-0.058	1.36
$\langle 110\rangle$ - $\langle 10\bar{1}0\rangle$	-1.29	-0.49	0.13	0.93	-0.089	1.33
$\langle 110\rangle$ - $\langle 11\bar{2}0\rangle$	1.37	1.32	2.79	2.74	0.42	1.84
$\langle 111\rangle$ - $\langle 000\frac{1}{2}\rangle$ Nickel - Oxygen	-2.81	-2.70	-1.39	-1.28	-2.95	-1.53
$\langle 111\rangle$ - $\langle 0001\rangle$ Zinc - Oxygen	-1.71	-0.96	-0.29	0.46	0.023	1.44
$\langle 111\rangle$ - $\langle 0001\rangle$ Nickel - Oxygen	-2.23	-1.00	-0.81	0.42	-0.12	1.30
$\langle 111\rangle$ - $\langle 000\frac{1}{2}\rangle$ Zinc - Oxygen	0.076	0.0017	1.50	1.42	-0.32	1.10
$\langle 111\rangle$ - $\langle 10\bar{1}0\rangle$ Nickel - Oxygen	0.66	0.33	2.08	1.75	-0.61	0.81
$\langle 111\rangle$ - $\langle 10\bar{1}0\rangle$ Zinc - Oxygen	0.88	0.43	2.30	1.85	-0.69	0.73
$\langle 111\rangle$ - $\langle 11\bar{2}0\rangle$ Nickel - Oxygen	-1.24	-0.99	0.18	0.43	-0.51	0.91
$\langle 111\rangle$ - $\langle 11\bar{2}0\rangle$ Zinc - Oxygen	-0.81	-0.46	0.61	0.96	-0.12	1.30

The mixed natural offsets all predict a type II band alignment for the interface in accordance with experimental evidence.[6,7,133] The only exception is the $\langle 111\rangle$ - $\langle 000\frac{1}{2}\rangle$ Ni-O interface, caused by steric repulsion between the NiO and ZnO slabs due to the lack of relaxation of the ionic structure.

The trends observed in the relaxed interface VBO values where the $\langle 111\rangle$ - $\langle 0001\rangle$ interfaces provided the smallest band offsets, are here indicated to primarily be because of strain. The

natural band offsets for these interfaces are on average greater in magnitude compared with the polar-nonpolar.

Comparing the static and relaxed interface VBO values, most of the strained ZnO interfaces exhibit considerably different band offsets, although the general trends are largely the same. The $\langle 110 \rangle$ - $\langle 11\bar{2}0 \rangle$ strained offset values in are largely unchanged, despite the differences in structures. Uniquely, the offset is nearly the same, regardless of which slab the strain is localized on. Furthermore, comparing the strained and natural band offsets of the interface, it may be established that the origin of the divergent offset for the relaxed $\langle 110 \rangle$ - $\langle 11\bar{2}0 \rangle$ interface, as noted in the section for relaxed interface band offsets, is indeed primarily due to the strain environment, but the natural properties of the interfaces also play a role.

Experimental values for the VBO, even for just the polar-polar interfaces, are relatively varied. The natural VBO values obtained in this study for the polar-polar interfaces show good agreement with the lower experimental values, although somewhat underestimated.[133,134] The experimental observation of a greater band offset for the $\langle 111 \rangle$ - $\langle 11\bar{2}0 \rangle$ interface compared to the polar-polar, is qualitatively observed for the Zn-O surfaces, but is not reproduced with other combinations of terminations.

The overall conclusion is similar to that of the relaxed interface, the specific arrangement of interface and strain distribution may have considerable effects on the band offset of the heterojunction and may potentially be utilized to engineer the properties of the interface, although the effect of the strain would likely only manifest to a considerable degree for thin film interfaces, below the critical thickness of the materials.

6. General Discussion

6.1. Mixed Phase System

For both the Ni:ZnO and Zn:NiO systems, the concentration of the solute ionic species exhibits significant effects on the electronic properties of the mixed phase materials, beyond an initial low concentration region. Both systems exhibit saturation behavior of the VBM shift at the concentration limits, so these energy levels would be expected to remain stable around equilibrium concentrations of the mixed phase systems.

The specific effects of concentration on the electronic properties are different between the two systems, but certain similarities are present. The VBM level increases in both systems by a maximum of about 0.26 eV and 0.39 eV for the Zn:NiO and Ni:ZnO systems respectively. If any mixed phase interface effects are neglected, according to the calculated heterojunction natural VBO values, heterojunctions formed from the mixed phase materials would likely remain as type II for all interfaces, albeit with a slightly reduced VBO value.

The effects observed on the Zn:NiO CBM value are more extensive, predicting a significant drop in the system band edge of 0.57 eV. As a result, the band gap decreases by about 0.8 eV. Experimental evidence on thin film systems exhibit a reduction of 0.51 eV, indicating the band edge drop to be somewhat overestimated, likely due to the overestimated pure NiO band gap.[118] Unlike the VBM level, the CBM level does not exhibit saturation behavior at the concentration limit, indicating that the conduction band level variation would be comparatively greater with different equilibrium concentrations of the Zn:NiO system. Due to the low extent of the change of the solid solution equilibrium concentration with temperature, this would likely not cause

issues under a practical context, although mixed-phase heterojunctions would exhibit slightly different properties depending on the operational temperature.

The band gap contraction of the Ni:ZnO system has been assigned by some studies to a d-orbital splitting of impurity states.[113] The calculations show some points in agreement with this theory, but others in opposition. The decrease of the band gap at 1.8% concentration does not agree with this model, as the impurity states are only observed at higher concentrations, while to the contrary, the high-spin magnetic arrangement of the nickel ions agree. A possible explanation is that the PBE0 functional places the energy of the nickel conduction band states too high and calculates an exaggerated gap with the conduction band states, similar to how the NiO band gap is overestimated. In this case, the results of the 3.7% concentration results would align with the d-orbital impurity state splitting model.

With respect to the effect of the mixed phases on the heterojunctions, as the VBM levels of both mixed phases are predicted to increase to a similar extent, and the CBM level of Ni:ZnO exhibits a relatively small change overall, the influence on the properties of a heterojunction would likely be dominated by the change in the Zn:NiO CBM. The lowered conduction band edge would have two direct consequences on the heterojunction: Firstly, the Fermi level is moved towards the NiO valence band, increasing the built-in potential of the mixed phase p-n junction, provided no other effects dominate, according to the experimental work functions of the pure phases.[126–132] Secondly, the CBO of the heterojunction would be substantially reduced. The significance of this will be noted in section 6.2.

In conclusion for the investigation on the mixed phase materials, the calculated effects of the isovalent doping with nickel and zinc ions at the necessary concentrations to form the thermodynamically stable materials, are sufficient that accounting for the properties of the mixed phase materials, not only the initial components, of a NiO – ZnO coexistent p-n heterojunction is necessary for accurately assessing its properties.

6.2. Heterojunction Interfaces

Due to the interaction between the differing chemical properties of the two components of the heterojunctions, interface states occurring in the band gap region is a consistent trait observed for nearly all interfaces. Such states have a considerable negative impact on the efficiency of such p-n junctions for applications such as solar panels, due to the tendency of such states to capture charge carriers. The same trap assisted surface recombination may also increase the junction recombination – generation current, by the Shockley-Hall-Read process.

The interface states primarily exhibit conduction band composition, either from the ZnO or the NiO structures, and are mainly caused by the presence of cations at the interface. The states may originate from either ZnO or NiO, but nickel ions are the primary cause of the lowest energy states for most interfaces. The exceptions are the NiO-⟨100⟩ interfaces with strained ZnO (see Figure 5-30, Figure 5-31), which is also the interfaces where the formation of NiO surface states decreases the energy of these CBM states the least, due to the surface geometry.

In addition to the properties of the individual surfaces, there are several factors that decide the prevalence and energy level of the interface states for any given interface. Presence of zinc ions not in a cross-interface bonding state, and in close proximity to the nickel ion acts as an enhancing factor for the nickel conduction band surface states, attracting them further out from the NiO surface, and lowering their energy compared to the level they assume when formed towards a vacuum (see Figure 5-47, Figure 5-48). In the cases where the zinc surface states dominate, the nickel ions act as the enhancers, but to a significantly lesser degree, as the ZnO surface states originate from the bulk, and are more tightly bound (see Figure 9-2). Another determining factor, is the extent of the cross-interface bonding. Oxygen ions act as inhibitors to the formation of conduction band interface states, either by the formation of ionic bonds, or by electrostatic repulsion from the negative charges increasing the orbital energy. Hence, surfaces where all nickel ions are sufficiently strongly bonded to at least one oxygen ion, do not display conduction band interface states. As a consequence of the previous point, the width of the interface, or the distance between the NiO and ZnO surfaces at any point within an interface

structure also plays a role. The clearest example of these tendencies is seen in Figure 5-34, where both tightly and weakly bound regions are present in the same interface.

Valence band states are primarily formed due to structural rearrangement from the ideal bulk structure, and thus depend significantly on the strain distribution (see Figure 5-47). For both the NiO and ZnO surfaces, the polar oxygen termination surface adjusts the most with relaxation towards a surface, resulting in valence band states occurring to the greatest extent for these surfaces (see Figure 5-16). While it applies to all surfaces, the application of tensile strain along the ab-plane to the NiO and ZnO polar surfaces significantly increase the valence band interface state energy by increasing the extent of the surface relaxation (compare Figure 5-23, left image, and Figure 5-38, left image at the ZnO oxygen termination). By the same reason, the formation of sufficiently strong cross-interface bonds may counteract the formation of valence band interface states by maintaining the oxygen termination structure closer to the bulk arrangement (compare Figure 5-38 and Figure 5-40). Cross-interface bonds may act in the opposite manner as well, forming valence band states if the bonding is too strong, but this is only observed in the $\langle 110 \rangle$-$\langle 10\bar{1}0 \rangle$ interface (see Figure 5-34).

Most of the interfaces display extensive interface states due to the connection between surface cations and interface states. The few interfaces that do not produce mid-gap interface states, all have the common feature of having a polar oxygen termination involved, either on the NiO or the ZnO surface. Due to the specific arrangements of surfaces required for the formation of a mid-gap interface state free junction, it is very likely that it could only be achieved under conditions where only single surfaces are permitted to form interfaces. As previously noted, polar interfaces involving the polar nickel termination surface are more energetically favorable compared to the oxygen terminated counterparts. Methodologies such as utilizing pellets to form the junction, would very likely exhibit extensive interface states, of every variety observed for these interfaces. Interface trap recombination will likely occur extensively, although the contribution of the effect on generation-recombination current would depend on the specific construction and usage environment of the junction.

The natural VBO values of the various interfaces (see Table 5-11) cover a range of 0.73-1.84 eV. Using band gap values of 3.37 eV for ZnO and 3.70 eV for NiO, following the previously

established convention, the CBO values correspondingly exhibit a range of -2.17- -1.06 eV. Overall, the potential barriers across the heterojunction will be dominated by the conduction band offset. As previously noted in section 6.2, the Zn:NiO phase exhibits a considerably lowered CBM level. Consequently, the dominant heterojunction barrier will be significantly reduced. Although the calculated CBM drop is overestimated, a drop of 0.5 eV would, in the case of the lowest VBO interface, halve the conduction band offset.

6.3. Practical Considerations

6.3.1. p-n Junctions

For certain applications of p-n junctions, such as solar cells, the presence of interface states is undesirable, as they directly result in loss of efficiency by capturing charge carriers. Consequently, there is interest in knowing what interface conditions minimize the prevalence of these states.

Minimizing the prevalence of the conductance and valence band states require different considerations. Valence band states are increased by the application of strain, the extent of ionic relaxation away from the bulk structure, and the arrangement of surfaces. The conduction band states are primarily determined by the arrangement of surfaces, as well as the strength and density of the cross-interface bonding if nickel ions are present at the surface.

The only interfaces that may fulfill these requirements to a sufficient degree, are the $\langle 111 \rangle$ - $\langle 000\frac{1}{2} \rangle$ interfaces. The polar-nonpolar Zn-O interfaces are less prone forming interface states than the polar-polar, but they exhibit considerable valence band states due to the oxygen surface relaxation due to lack of cross-interface bonding.

To form interfaces with the least interface states possible, either of the structures shown in Figure 5-40 must be formed. Forming an interface state free junction could, according to the results on this study, be accomplished by fulfilling several requirements. The main point for forming an interface state free junction, is to utilize an oxygen rich environment when the junction transition is formed, in addition to utilizing a polar-polar pair of interfaces. The separate surfaces must also

form a sufficiently tightly bonded structure, with the ZnO structure terminated at the correct plane. If the cross-interface bonding is too weak or sporadic, an electronic interface structure closer to the ⟨111⟩ - ⟨0001⟩ interfaces would result (see Figure 5-38). Under practical circumstances, this matter is greatly complicated, due to the structural mismatch, and the tendencies of the NiO and ZnO polar structures to spontaneously reconstruct, creating narrow voids in.[49,70] An example of the possible results of defective states due to structural mismatch may be seen in Figure 9-1: While this interface is not the relevant polar-polar, the strain applied to the NiO interface structure increases the Ni-O bond length in the ab-plane, sufficient to produce effects akin to dislocation defects. Consequently, the entire structure is covered in defect states. The static structure does aggravate the results by maintaining the flawed structure throughout, however relaxation of an interface such a degree of flaws, results in extensive failures of the structure. ab-plane strain is much less significant for c-axis oriented NiO-⟨111⟩, but a defective NiO structure at the interface could cause defect states, depending on the extent of the defective structure.

6.3.2. Nanocomposites

A particular nanocomposite of interest for coexistent oxide, is the structure that forms upon phase separation of a metal oxide mixture corresponding to a two-phase region. Deducing the exact prevalence of interfaces in such a complex system is practically impossible. However, assuming an idealized nanocomposite structure where the internal structures are determined entirely by the interface formation energies and the principles of Wulff construction, certain deductions may be made.

Upon phase separation, the resulting interface structures between the Ni:ZnO and Zn:NiO phases will not have the strain localized on one phase, but rather distributed between the phases. The local strain distribution at the interface would be decided by the relative elastic moduli of the two phases.

Neglecting the unknown effects of the mixed phases on the interface formation energy, for the Zn:NiO structure, the interfaces involving the ⟨111⟩ surface are always the more favorable. As it

is possible to form a complete crystal surface exposing only the $\langle 111 \rangle$ surfaces, it would be predicted that the NiO crystals will preferentially approach the octahedron crystal structure of such an arrangement. Further, since the Ni-O interfaces are collectively the most favorable polar interfaces of NiO, the surfaces would preferentially exhibit a nickel ion termination at the surface.

The Ni:ZnO structure is more complicated. The polar-polar interface with the Zn:NiO structure would preferentially form, however due to the wurtzite structure, a complete crystal cannot be formed with only $\langle 0001 \rangle / \langle 000\frac{1}{2} \rangle$ surfaces. Consequently, polar-nonpolar interfaces with the $\langle 10\bar{1}0 \rangle$ and $\langle 11\bar{2}0 \rangle$ surfaces of Ni:ZnO will also be present, forming interfaces with the nickel terminated NiO crystals.

As previously noted in section 5.4.2, the Ni-O polar-nonpolar interfaces exhibit continuous conduction band states across the surface, with an energy range across the entire band gap. Consequently, the interface could be expected to exhibit enhanced conductivity. While the extent of the effect would depend on the extent to which the conducting interfaces are interconnected, a nanocomposite of the Zn:NiO – Ni:ZnO type could be expected to exhibit higher electron conductivity than the bulk materials due to this enhanced interface boundary conductivity effect.

The idealized nanocomposite case considered here is significantly simplified, however. A physical nanocomposite from a phase separation would exhibit extensive differences from the idealized case. Nonequilibrium crystal structures due to separate factors from surface energy, such as steric hindrance, would likely dominate the nanoscale crystal structure. The physical nanocomposite interface regions would still be covered in interfaces states, although not only the continuous polar-nonpolar interface states that would dominate an ideal interface.

The high concentration of zinc in the equilibrium structure is also a source of divergence from the ideal case. Even at significantly lower dopant concentrations, the zinc ions are experimentally reported to cause considerable divergence from the pure NiO crystal structures, but this is dependent on the production method of the Zn:NiO material.[112,117]

6.4. Further Work

The NiO-ZnO coexistent heterojunction system is complex, with many separate factors closely interacting. Consequently, there are necessarily several factors that are not considered within the scope of this study. In a practical interface system, doping the metal oxide semiconductors is necessary due to the low intrinsic charge carrier densities of the materials. Investigating the effect of these dopants on the interface properties is thus necessary. The matter is further complicated by the mixed phase materials present in a coexistent heterojunction, as the dopant effect on these mixed phase materials must also be considered.

This study has shown that the properties of the NiO-ZnO heterojunction depends significantly on the specific arrangement of surfaces and termination ions of the interface. Hence it is possible that the interface properties observed with mixed phase interface slabs would display significant differences from the pure phase interfaces considered in this study. Hence, there is a need to study the properties of mixed phase interfaces directly, both by experimental and theoretical means.

7. Conclusion

Utilizing DFT with the PBE0 functional, the formation of the NiO – ZnO mixed phase materials are predicted to exhibit significant effects on the electronic band edge levels. The Ni:ZnO and Zn:NiO systems exhibit an increase in VBM energy level relative to the pure materials with maximum values of 0.39 eV and 0.26 eV, caused by the formation of localized impurity states and cubic phase ZnO states, respectively. The VBM level shifts reach saturation with respect to solute ion concentration at 3.70% and 4.69%, again respectively. The band gap width of both mixed phase materials is reduced with solute ion concentration, with a limit reduction of 0.3 eV for Ni:ZnO. The Zn:NiO CBM shift has not reached saturation at the high limit zinc ion concentration of 31.25%, and exhibits a band gap reduction of 0.8 eV at this concentration. The formation of mixed phase materials is thus considered likely to significantly alter the properties of a NiO – ZnO heterojunction.

The properties of the NiO – ZnO heterojunctions are predicted to exhibit considerable dependence on the specific arrangement of the surfaces forming the interface, both on the ionic termination surfaces, and the distribution of strain between these. Properties display rough similarities between groups of nonpolar-nonpolar, polar-polar and polar-nonpolar, but the interfaces among each group exhibit considerable differences. The interface formation energy, regardless of strain distribution, favors the formation of the polar-polar interfaces.

The natural band offsets make the NiO – ZnO heterojunction a type II heterojunction, however the different interfaces display a significant range of valence band offset values, ranging from 0.73 to 1.84 eV. Interface mid-gap states, predominantly Ni-3d conduction band states, are present in nearly all interface arrangements. The results present evidence that the prevalence of these interface states, and the general properties of a NiO-ZnO heterojunction, may potentially be manipulated by selection of a suitable interface, and the growth conditions under which it is formed.

8.References

1. Ambrozic, G., Skapin, S. D., Zigon, M. & Orel, Z. C. The synthesis of zinc oxide nanoparticles from zinc acetylacetonate hydrate and 1-butanol or isobutanol. *J. Colloid Interface Sci.* **346**, 317–323 (2010).

2. Sawatzky, G. A. & Allen, J. W. Magnitude and Origin of the Band Gap in NiO. *Phys. Rev. Lett.* **53**, 2339–2342 (1984).

3. Sato, H., Minami, T., Takata, S. & Yamada, T. Transparent conducting p-type NiO thin films prepared by magnetron sputtering. *Thin Solid Films* **236**, 27–31 (1993).

4. Zhang, Z. Y. *et al.* Electrospun Nanofibers of p-Type NiO/n-Type ZnO Heterojunctions with Enhanced Photocatalytic Activity. *ACS Appl. Mater. Interfaces* **2**, 2915–2923 (2010).

5. Gaskell, K. J., Starace, A. & Langell, M. A. $Zn_xNi_{1-x}O$ rocksalt oxide surfaces: Novel environment for Zn^{2+} and its effect on the NiO band structure. *J. Phys. Chem. C* **111**, 13912–13921 (2007).

6. Ma, M. J. *et al.* Orientation dependent band alignment for p-NiO/n-ZnO heterojunctions. *J. Appl. Phys.* **113**, 4 (2013).

7. Deng, R. *et al.* X-ray photoelectron spectroscopy measurement of n-ZnO/p-NiO heterostructure valence-band offset. *Appl. Phys. Lett.* **94**, 3 (2009).

8. Gupta, R. K., Ghosh, K. & Kahol, P. K. Fabrication and characterization of NiO/ZnO p–n junctions by pulsed laser deposition. *Physica E: Low-dimensional Systems and Nanostructures* **41**, 617–620 (2009).

9. Hohenberg, P. & Kohn, W. Inhomogeneous Electron Gas. *Phys. Rev.* **136**, B864–B871 (1964).

10. Kohn, W. & Sham, L. J. Self-Consistent Equations Including Exchange and Correlation Effects. *Phys. Rev.* **140**, A1133–A1138 (1965).

11. Liechtenstein, A. I., Anisimov, V. I. & Zaanen, J. Density-functional theory and strong interactions: Orbital ordering in Mott-Hubbard insulators. *Phys. Rev. B* **52**, R5467–R5470 (1995).

12. Dudarev, S. L., Botton, G. A., Savrasov, S. Y., Humphreys, C. J. & Sutton, A. P. Electron-energy-loss spectra and the structural stability of nickel oxide: An LSDA+U study. *Phys. Rev. B* **57**, 1505–1509 (1998).

13. Erhart, P., Klein, A., \AAberg, D. & Sadigh, B. Efficacy of the DFT + U formalism for modeling hole polarons in perovskite oxides. *Phys. Rev. B* **90**, 035204 (2014).

14. Perdew, J. P., Parr, R. G., Levy, M. & Balduz, J. L. Density-Functional Theory for Fractional Particle Number: Derivative Discontinuities of the Energy. *Phys. Rev. Lett.* **49**, 1691–1694 (1982).

15. Lindman, A., Erhart, P. & Wahnström, G. Polaronic contributions to oxidation and hole conductivity in acceptor-doped $BaZrO_3$. *Phys. Rev. B* **94**, 075204 (2016).

16. P. Perdew, J., Burke, K. & Ernzerhof, M. Generalized Gradient Approximation Made Simple. *Physical review letters* **77**, 3865–3868 (1996).

17. Adamo, C. & Barone, V. Toward reliable density functional methods without adjustable parameters: The PBE0 model. *J. Chem. Phys.* **110**, (1999).

18. Kröger, F. A. & Vink, H. J. Relations between the concentrations of imperfections in crystalline solids. *Solid State Physics, 3, 307.* (1956).

19. Joyce, W. B. & Dixon, R. W. Analytic approximations for the Fermi energy of an ideal Fermi gas. *Applied Physics Letters* **31**, 354–356 (1977).

20. Muller, R. S. & Kamins, T. I. *Device Electronics for Integrated Circuits*.

21. Kasap, S. *Principles of Electronic Materials and Devices*. (2006).

22. Bozyigit, D., Lin, W. M. M., Yazdani, N., Yarema, O. & Wood, V. A quantitative model for charge carrier transport, trapping and recombination in nanocrystal-based solar cells. *Nature Communications* **6**, 6180 (2015).

23. Ortiz-Conde, A., García-Sánchez, F. & Muci, J. *Exact analytical solutions of the forward non-ideal diode equation with series and shunt parasitic resistances*. **44**, (2000).

24. Wulff, G. Zur Frage der Geschwindigkeit des Wachstums und der Auflösung der Krystallflagen. 1901;34(5/6):449-530. *Zeitschrift Fur Kristallographie.*

25. Kresse, G. & Hafner, J. Ab initio molecular dynamics for liquid metals. *Phys. Rev. B* **47**, 558–561 (1993).

26. Kresse, G. & Furthmüller, J. Efficiency of ab-initio total energy calculations for metals and semiconductors using a plane-wave basis set. *Computational Materials Science* **6**, 15–50 (1996).

27. Kresse, G. & Furthmüller, J. Efficient iterative schemes for ab initio total-energy calculations using a plane-wave basis set. *Phys. Rev. B* **54**, 11169–11186 (1996).

28. Segall, M. D. *et al.* First-principles simulation: ideas, illustrations and the CASTEP code. *Journal of Physics Condensed Matter* **14**, 2717–2744 (2002).

29. Kresse, G. & Hafner, J. Norm-conserving and ultrasoft pseudopotentials for first-row and transition elements. *Journal of Physics: Condensed Matter* **6**, 8245–8257 (1994).

30. Kresse, G. & Joubert, D. From ultrasoft pseudopotentials to the projector augmented-wave method. *Phys. Rev. B* **59**, 1758–1775 (1999).

31. Rohrbach, A., Hafner, J. & Kresse, G. Molecular adsorption on the surface of strongly correlated transition-metal oxides: A case study for CO/NiO(100). *Phys. Rev. B* **69**, 075413 (2004).

32. Baldereschi, A., Baroni, S. & Resta, R. Band Offsets in Lattice-Matched Heterojunctions: A Model and First-Principles Calculations for GaAs/AlAs. *Phys. Rev. Lett.* **61**, 734–737 (1988).

33. Dong, L. *et al.* Strain induced variations in band offsets and built-in electric fields in InGaN/GaN multiple quantum wells. *Journal of Applied Physics* **114**, 043715 (2013).

34. Hinuma, Y., Grüneis, A., Kresse, G. & Oba, F. Band alignment of semiconductors from density-functional theory and many-body perturbation theory. *Phys. Rev. B* **90**, 155405 (2014).

35. Tang, W., Sanville, E. & Henkelman, G. A grid-based Bader analysis algorithm without lattice bias. *Journal of Physics: Condensed Matter* **21**, 084204 (2009).

36. Yu, M. & Trinkle, D. R. Accurate and efficient algorithm for Bader charge integration. *The Journal of Chemical Physics* **134**, 064111 (2011).

37. Henkelman, G., Arnaldsson, A. & Jónsson, H. A fast and robust algorithm for Bader decomposition of charge density. *Computational Materials Science* **36**, 354–360 (2006).

38. Sanville, E., Kenny, S. D., Smith, R. & Henkelman, G. Improved grid-based algorithm for Bader charge allocation. *Journal of Computational Chemistry* **28**, 899–908 (2007).

39. GREENWOOD, N. N. & EARNSHAW, A. *Chemistry of the elements*. (Oxford: Pergamon Press., 1994).

40. Irwin, M. D., Buchholz, D. B., Hains, A. W., Chang, R. P. H. & Marks, T. J. p-Type semiconducting nickel oxide as an efficiency-enhancing anode interfacial layer in polymer bulk-heterojunction solar cells. *Proceedings of the National Academy of Sciences of the United States of America* **105**, 2783–2787 (2008).

41. Smart, J. S. & Greenwald, S. Crystal Structure Transitions in Antiferromagnetic Compounds at the Curie Temperature. *Phys. Rev.* **82**, 113–114 (1951).

42. Vernon, M. W. & Lovell, M. C. Anomalies in the electrical conductivity of nickel oxide above room temperature. *Journal of Physics and Chemistry of Solids* **27**, 1125–1131 (1966).

43. Rodbell, D. S. & Owen, J. Sublattice Magnetization and Lattice Distortions in MnO and NiO. *Journal of Applied Physics* **35**, 1002–1003 (1964).

44. Shull, C. G., Strauser, W. A. & Wollan, E. O. Neutron Diffraction by Paramagnetic and Antiferromagnetic Substances. *Phys. Rev.* **83**, 333–345 (1951).

45. Roth, W. L. Magnetic Structures of MnO, FeO, CoO, and NiO. *Phys. Rev.* **110**, 1333–1341 (1958).

46. Tjernberg, O. *et al.* Influence of magnetic ordering on the NiO valence band. *Phys. Rev. B* **54**, 10245–10248 (1996).

47. Ressouche, E., Kernavanois, N., Regnault, L.-P. & Henry, J.-Y. Magnetic structures of the metal monoxides NiO and CoO re-investigated by spherical neutron polarimetry. *Physica B: Condensed Matter* **385–386**, 394–397 (2006).

48. Sterrer, M. & Freund, H.-J. Properties of Oxide Surfaces. in *Surface and Interface Science* 229–278 (John Wiley & Sons, Ltd, 2014). doi:10.1002/9783527680559.ch15

49. Freund, H.-J., Kuhlenbeck, H. & Staemmler, V. Oxide surfaces. *Reports on Progress in Physics* **59**, 283 (1996).

50. Heikes, R. R. & Johnston, W. D. MECHANISM OF CONDUCTION IN LI-SUBSTITUTED TRANSITION METAL OXIDES. *J. Chem. Phys.* **26**, 582–587 (1957).

51. Houten, S. V. Semiconduction in $Li_xNi_{1-x}O$. *Journal of Physics and Chemistry of Solids* **17**, 7–17 (1960).

52. Kofstad, P. Defects and transport properties of metal oxides. *Oxidation of Metals* **44**, 3–27 (1995).

53. Pickering, I. J., George, G. N., Lewandowski, J. T. & Jacobson, A. J. Nickel K-edge x-ray absorption fine structure of lithium nickel oxides. *Journal of the American Chemical Society* **115**, 4137–4144 (1993).

54. Kuiper, P., Kruizinga, G., Ghijsen, J., Sawatzky, G. A. & Verweij, H. Character of Holes in $Li_xNi_{1-x}O$ and Their Magnetic Behavior. *Phys. Rev. Lett.* **62**, 221–224 (1989).

55. Osburn, C. M. & Vest, R. W. Defect structure and electrical properties of NiO—I. High temperature. *Journal of Physics and Chemistry of Solids* **32**, 1331–1342 (1971).

56. Heikes, R. R. & Johnston, W. D. Mechanism of Conduction in Li-Substituted Transition Metal Oxides. *The Journal of Chemical Physics* **26**, 582–587 (1957).

57. Degraix, H., Gravelle, P. C. & Teichner, S. J. Etude des solutions solides d'oxyde de lithium dans l'oxyde de nickel. II. Influence de la pression d'oxygene et mecanismes d'incorporation. *Journal of Solid State Chemistry* **18**, 79–88 (1976).

58. Popescu, I., Skoufa, Z., Heracleous, E., Lemonidou, A. & Marcu, I.-C. A study by electrical conductivity measurements of the semiconductive and redox properties of Nb-doped NiO catalysts in correlation with the oxidative dehydrogenation of ethane. *Phys. Chem. Chem. Phys.* **17**, 8138–8147 (2015).

59. Morin, F. J. Electrical Properties of NiO. *Phys. Rev.* **93**, 1199–1204 (1954).

60. Shin, W. & Murayama, N. Li-Doped Nickel Oxide as a Thermoelectric Material. *Japanese Journal of Applied Physics* **38**, L1336–L1338 (1999).

61. Antolini, E. LixNi1−xO (0<x≤0.3) solid solutions: formation, structure and transport properties. *Materials Chemistry and Physics* **82**, 937–948 (2003).

62. Anisimov, V. I., Korotin, M. A. & Kurmaev, E. Z. Band-structure description of Mott insulators (NiO, MnO, FeO, CoO). *Journal of Physics: Condensed Matter* **2**, 3973 (1990).

63. Zhang, W.-B., Yu, N., Yu, W. & Tang, B.-Y. *Stability and magnetism of vacancy in NiO: A GGA+U study*. **64**, (2008).

64. Alperin, H. A. Aspherical 3d Electron Distribution in Ni++. *Phys. Rev. Lett.* **6**, 55–57 (1961).

65. Fender, B. E. F., Jacobson, A. J. & Wedgwood, F. A. Covalency Parameters in MnO, α-MnS, and NiO. *J. Chem. Phys.* **48**, 990–994 (1968).

66. Cheetham, A. K. & Hope, D. A. O. Magnetic ordering and exchange effects in the antiferromagnetic solid solutions $Mn_xNi_{1-x}O$. *Phys. Rev. B* **27**, 6964–6967 (1983).

67. Tasker, P. W. & Duffy, D. M. The structure and properties of the stepped surfaces of MgO and NiO. *Surface Science* **137**, 91–102 (1984).

68. Anisimov, V. & Kozhevnikov, A. *Transition state method and Wannier functions*. **72**, (2005).

69. Zhang, W.-B., Hu, Y.-L., Han, K.-L. & Tang, B.-Y. Pressure dependence of exchange interactions in NiO. *Phys. Rev. B* **74**, 054421 (2006).

70. Svensson, B. G., Pearton, S. J. & Jagadish, C. *Oxide Semiconductors*. **88**,

71. Ozgur, U. *et al.* A comprehensive review of ZnO materials and devices. *J. Appl. Phys.* **98**, 103 (2005).

72. Baruah, S. & Dutta, J. Hydrothermal growth of ZnO nanostructures. *Sci. Technol. Adv. Mater.* **10**, 18 (2009).

73. Gatos, H. C. Semiconductor electronics and the birth of the modern science of surfaces. *Surface Science* **299–300**, 1–23 (1994).

74. Duke, C. B. Structure and bonding of tetrahedrally coordinated compound semiconductor cleavage faces. *Journal of Vacuum Science & Technology A* **10**, 2032–2040 (1992).

75. Dulub, O., Boatner, L. A. & Diebold, U. STM study of the geometric and electronic structure of ZnO(0 0 0 1)-Zn, (0 0 0 $\bar{1}$)-O, (1 0 $\bar{1}$ 0), and (1 1 $\bar{2}$ 0) surfaces. *Surface Science* **519**, 201–217 (2002).

76. Dulub, O., Diebold, U. & Kresse, G. Novel Stabilization Mechanism on Polar Surfaces: ZnO(0001)-Zn. *Phys. Rev. Lett.* **90**, 016102 (2003).

77. Janotti, A. & Van de Walle, C. G. Native point defects in ZnO. *Phys. Rev. B* **76**, 22 (2007).

78. Thomas, D. G. Interstitial zinc in zinc oxide. *Journal of Physics and Chemistry of Solids* **3**, 229–237 (1957).

79. Wardle, M. G., Goss, J. P. & Briddon, P. R. First-Principles Study of the Diffusion of Hydrogen in ZnO. *Phys. Rev. Lett.* **96**, 205504 (2006).

80. Janotti, A. & Van de Walle, C. G. Hydrogen multicentre bonds. *Nature Materials* **6**, 44 (2006).

81. Hutson, A. R. Electronic properties of ZnO. *Journal of Physics and Chemistry of Solids* **8**, 467–472 (1959).

82. Hahn, E. E. Some Electrical Properties of Zinc Oxide Semiconductor. *Journal of Applied Physics* **22**, 855–863 (1951).

83. Ziegler, E., Heinrich, A., Oppermann, H. & Stöver, G. Electrical properties and non-stoichiometry in ZnO single crystals. *physica status solidi (a)* **66**, 635–648 (1981).

84. Tsubota, T., Ohtaki, M., Eguchi, K. & Arai, H. Thermoelectric properties of Al-doped ZnO as a promising oxidematerial for high-temperature thermoelectric conversion.

85. Shi, G. A. *et al.* Hydrogen local modes and shallow donors in ZnO. *Phys. Rev. B* **72**, 195211 (2005).

86. Minami, T., Miyata, T. & Ohtani, Y. Optimization of aluminum-doped ZnO thin-film deposition by magnetron sputtering for liquid crystal display applications. *physica status solidi (a)* **204**, 3145–3151 (2007).

87. Chang, H. P., Wang, F. H., Wu, J. Y., Kung, C. Y. & Liu, H. W. Enhanced conductivity of aluminum doped ZnO films by hydrogen plasma treatment. *Thin Solid Films* **518**, 7445–7449 (2010).

88. Tark, S. J. *et al.* Effect of a hydrogen ratio in electrical and optical properties of hydrogenated Al-doped ZnO films. *Journal of Electroceramics* **23**, 548 (2008).

89. Lander, J. J. Reactions of Lithium as a donor and an acceptor in ZnO. *Journal of Physics and Chemistry of Solids* **15**, 324–334 (1960).

90. Fan, J. C., Sreekanth, K. M., Xie, Z., Chang, S. L. & Rao, K. V. p-Type ZnO materials: Theory, growth, properties and devices. *Progress in Materials Science* **58**, 874–985 (2013).

91. Ma, X., Wu, Y., Lv, Y. & Zhu, Y. Correlation Effects on Lattice Relaxation and Electronic Structure of ZnO within the GGA+U Formalism. *J. Phys. Chem. C* **117**, 26029–26039 (2013).

92. Afruz, F. B., Tafreshi, M. J., Mohammadizadeh, M. R. & Fazli, M. Structural and electronic properties of hydrogen doped Wurtzite ZnO. *Computational Materials Science* **143**, 232–239 (2018).

93. Bashyal, K., Pyles, C. K., Afroosheh, S., Lamichhane, A. & Zayak, A. T. Empirical optimization of DFT+U and HSE for the band structure of ZnO. *Journal of Physics: Condensed Matter* **30**, 065501 (2018).

94. Huang, G.-Y., Wang, C.-Y. & Wang, J.-T. Detailed check of the LDA+U and GGA+U corrected method for defect calculations in wurtzite ZnO. *Computer Physics Communications* **183**, 1749–1752 (2012).

95. Tang, C., Spencer, M. J. S. & Barnard, A. S. Activity of ZnO polar surfaces: An insight from surface energies. *Physical Chemistry Chemical Physics* **16**, 22139–22144 (2014).

96. Liu, P.-L. & Siao, Y.-J. Ab initio study on preferred growth of ZnO. *Scripta Materialia* **64**, 483–485 (2011).

97. Meyer, B. & Marx, D. Density-functional study of the structure and stability of ZnO surfaces. *Phys. Rev. B* **67**, 035403 (2003).

98. Jia, X. F., Hou, Q. Y., Xu, Z. C. & Qu, L. F. Effect of Ce doping on the magnetic and optical properties of ZnO by the first principle. *Journal of Magnetism and Magnetic Materials* **465**, 128–135 (2018).

99. Tyagi, M., Tomar, M. & Gupta, V. Fabrication of an efficient GLAD-assisted p-NiO nanorod/n-ZnO thin film heterojunction UV photodiode. *J. Mater. Chem. C* **2**, 2387–2393 (2014).

100. Rubio-Marcos, F. *et al.* Mechanism of Ni1–xZnxO Formation by Thermal Treatments on NiO Nanoparticles Dispersed over ZnO. *J. Phys. Chem. C* **115**, 13577–13583 (2011).

101. Kurokawa, H., Nanko, M., Kawamura, K. & Maruyama, T. *Stability and electrical properties of high temperature p-n junction of NiO-ZnO system*. **2001**, (Electrochemical Society Inc, 2002).

102. Sinn, D. S. Electrical properties of p-NiO/n-ZnO two-phase mixtures. *Solid State Ion.* **83**, 333–348 (1996).

103. Bates, C. H., White, W. B. & Roy, R. The solubility of transition metal oxides in zinc oxide and the reflectance spectra of Mn2+ and Fe2+ in tetrahedral fields. *Journal of Inorganic and Nuclear Chemistry* **28**, 397–405 (1966).

104. Dar, T. A. *et al.* Valence and conduction band offset measurements in Ni0.07Zn0.93O/ZnO heterostructure. *Current Applied Physics* **14**, 171–175 (2014).

105. Ghotbi, M. Y. Nickel doped zinc oxide nanoparticles produced by hydrothermal decomposition of nickel-doped zinc hydroxide nitrate. *Particuology* **10**, 492–496 (2012).

106. Mondal, S. *Preparation of Ni doped ZnO thin films by SILAR and their Characterization*. (2013). doi:10.1007/s12648-012-0198-8

107. Grace Masih, V., Kumar, N. & Srivastava, A. Diminution in the Optical Band Gap and Near Band Edge Emission of Nickel-Doped Zinc Oxide Thin Films Deposited by Sol-Gel Method. *Journal of Applied Spectroscopy* **84**, 1145–1152 (2018).

108. Chauhan, R., Kumar, A. & Chaudhary, R. P. Structures and optical properties of Zn1−xNixO nanoparticles by coprecipitation method. *Research on Chemical Intermediates* **38**, 1483–1493 (2012).

109. Abdel-wahab, M. S., Jilani, A., Yahia, I. S. & Al-Ghamdi, A. A. Enhanced the photocatalytic activity of Ni-doped ZnO thin films: Morphological, optical and XPS analysis. *Superlattices and Microstructures* **94**, 108–118 (2016).

110. Dewan, S. *et al.* Study of energy band discontinuity in NiZnO/ZnO heterostructure using X-ray photoelectron spectroscopy. *Applied Physics Letters* **108**, 211603 (2016).

111. Goswami, N. & Sahai, A. Structural transformation in nickel doped zinc oxide nanostructures. *Materials Research Bulletin* **48**, 346–351 (2013).

112. Abdul Fattah, Z. *Synthesis and characterization of nickel doped zinc oxide nanoparticles by sol – gel method*. **5**, (2016).

113. Singh, S., Rama, N. & Ramachandra Rao, M. S. Influence of d-d transition bands on electrical resistivity in Ni doped polycrystalline ZnO. *Applied Physics Letters* **88**, 222111 (2006).

114. Singhal, A. *et al.* Chemical Synthesis and Structural and Magnetic Properties of Dispersible Cobalt-and Nickel-Doped ZnO Nanocrystals. *The Journal of Physical Chemistry C* **114**, 3422–3430 (2010).

115. Mondal, A., Giri, N., Sarkar, S. & Ray, R. Magnetic properties of Zn1-xNixO. *AIP Conference Proceedings* **1953**, 120017 (2018).

116. Farjami, S. & Nosrati, R. *The Structural and Magnetic Properties of Diluted Magnetic Semiconductor Zn1−xNixO Nanoparticles*. **28**, (2015).

117. Peck, M. A. & Langell, M. A. Metal Structural Environment in ZnxNi1–xO Macroscale and Nanoscale Solid Solutions. *The Journal of Physical Chemistry C* **118**, 12050–12060 (2014).

118. Manouchehri, I., AlShiaa, S. A. O., Mehrparparvar, D., Hamil, M. I. & Moradian, R. Optical properties of zinc doped NiO thin films deposited by RF magnetron sputtering. *Optik* **127**, 9400–9406 (2016).

119. Hashim, F. Sh. & Sami, N. A. Effect of Zn Doping on Structural and some Optical Studies of Nano NiO Films Prepared by Sol-Gel Technique. *International Letters of Chemistry, Physics and Astronomy* **53**, 31–40 (2015).

120. Rodic, D., Spasojevic, V., Kusigerski, V., Tellgren, R. & Rundlof, H. Magnetic Ordering in Polycrystalline NixZn1—xO Solid Solutions. *physica status solidi (b)* **218**, 527–536 (2000).

121. Desissa, T. D., Haugsrud, R., Wiik, K. & Norby, T. Inter-diffusion across a direct p-n heterojunction of Li-doped NiO and Al-doped ZnO. *Solid State Ionics* **320**, 215–220 (2018).

122. Phillips, B., Hutta, J. J. & Warshaw, I. PHASE EQUILIBRIA IN THE SYSTEM NIO-AL2O3-SIO2. *J. Am. Ceram. Soc.* **46**, 579–583 (1963).

123. Kwon, U. *et al.* Solution-Processible Crystalline NiO Nanoparticles for High-Performance Planar Perovskite Photovoltaic Cells. *Sci Rep* **6**, 10 (2016).

124. Moormann, H., Kohl, D. & Heiland, G. WORK FUNCTION AND BAND BENDING ON CLEAN CLEAVED ZINC-OXIDE SURFACES. *Surf. Sci.* **80**, 261–264 (1979).

125. Desissa, T. D., Schrade, M. & Norby, T. Electrical Properties of a p–n Heterojunction of Li-Doped NiO and Al-Doped ZnO for Thermoelectrics. *Journal of Electronic Materials* **47**, 5296–5301 (2018).

126. Greiner, M. T., Helander, M. G., Wang, Z.-B., Tang, W.-M. & Lu, Z.-H. Effects of Processing Conditions on the Work Function and Energy-Level Alignment of NiO Thin Films. *J. Phys. Chem. C* **114**, 19777–19781 (2010).

127. Oey, C. C. *et al.* Nanocomposite hole injection layer for organic device applications. *Thin Solid Films* **492**, 253–258 (2005).

128. Steirer, K. X. *et al.* Solution deposited NiO thin-films as hole transport layers in organic photovoltaics. *Organic Electronics* **11**, 1414–1418 (2010).

129. Olivier, J., Servet, B., Vergnolle, M., Mosca, M. & Garry, G. Stability/instability of conductivity and work function changes of ITO thin films, UV-irradiated in air or vacuum: Measurements by the four-probe method and by Kelvin force microscopy. *Synthetic Metals* **122**, 87–89 (2001).

130. Jacobi, K., Zwicker, G. & Gutmann, A. Work function, electron affinity and band bending of zinc oxide surfaces. *Surface Science* **141**, 109–125 (1984).

131. Moormann, H., Kohl, D. & Heiland, G. Work function and band bending on clean cleaved zinc oxide surfaces. *Surface Science* **80**, 261–264 (1979).

132. Moormann, H., Kohl, D. & Heiland, G. Variations of work function and surface conductivity on clean cleaved zinc oxide surfaces by annealing and by hydrogen adsorption. *Surface Science* **100**, 302–314 (1980).

133. Yang, Z.-G. *et al.* Valence-band offset of p-NiO/n-ZnO heterojunction measured by X-ray photoelectron spectroscopy. *Physics Letters A* **375**, 1760–1763 (2011).

134. Echresh, A. *et al.* UV photo-detector based on p-NiO thin film/n-ZnO nanorods heterojunction prepared by a simple process. *Journal of Alloys and Compounds* **632**, 165–171 (2015).

135. Ievskaya, Y., Hoye, R. L. Z., Sadhanala, A., Musselman, K. P. & MacManus-Driscoll, J. L. Fabrication of ZnO/Cu2O heterojunctions in atmospheric conditions: Improved interface quality and solar cell performance. *Solar Energy Materials and Solar Cells* **135**, 43–48 (2015).

136. Jeong, S. S., Mittiga, A., Salza, E., Masci, A. & Passerini, S. Electrodeposited ZnO/Cu2O heterojunction solar cells. *Electrochimica Acta* **53**, 2226–2231 (2008).

137. Eom, K., Lee, D., Kim, S. & Seo, H. Modified band alignment effect in ZnO/Cu2O heterojunction solar cells via Cs2O buffer insertion. *Journal of Physics D: Applied Physics* **51**, 055101 (2018).

138. Minami, T., Nishi, Y., Miyata, T. & Nomoto, J. High-Efficiency Oxide Solar Cells with ZnO/Cu2O Heterojunction Fabricated on Thermally Oxidized Cu2O Sheets. *Applied Physics Express - APPL PHYS EXPRESS* **4**, (2011).

139. Zhu, L. *et al.* Synthesis of the 0D/3D CuO/ZnO Heterojunction with Enhanced Photocatalytic Activity. *The Journal of Physical Chemistry C* **122**, 9531–9539 (2018).

140. Liu, C. *et al.* CuO/ZnO heterojunction nanoarrays for enhanced photoelectrochemical water oxidation. *Applied Surface Science* **469**, 276–282 (2019).

141. Schein, F.-L., von Wenckstern, H. & Grundmann, M. *Transparent p-CuI/n-ZnO heterojunction diodes*. **102**, (2013).

142. Feng, H.-J. *et al.* The origin of enhanced optical absorption of the BiFeO3/ZnO heterojunction in the visible and terahertz regions. *Phys. Chem. Chem. Phys.* **17**, 26930–26936 (2015).

143. Guo, D. Y. *et al.* Fabrication of Ga_2O_3/ZnO heterojunction for solar-blind deep ultraviolet photodetection. *Semiconductor Science and Technology* **32**, 03LT01 (2017).

144. Khim, D. *et al. Modulation-Doped In_2O_3/ZnO Heterojunction Transistors Processed from Solution*. (Wiley-Blackwell, 2017). doi:10.1002/adma.201605837

145. Jeong, S. & Kim, H. Enhanced performance characteristics of n-ZnO/p-GaN heterojunction light-emitting diodes by forming excellent Ohmic contact to p-GaN. *Materials Science in Semiconductor Processing* **39**, 771–774 (2015).

146. Rödl, C. & Schleife, A. Photoemission spectra and effective masses of n- and p-type oxide semiconductors from first principles: ZnO, CdO, SnO2, MnO, and NiO. *physica status solidi (a)* **211**, 74–81 (2014).

147. Choi, S. C., Koumoto, K. & Yanagida, H. Electrical conduction and effective mass of a hole in single-crystal NiO. *Journal of Materials Science* **21**, 1947–1950 (1986).

148. Anderson Janotti and Chris G Van de Walle. Fundamentals of zinc oxide as a semiconductor. *Reports on Progress in Physics* **72**, 126501 (2009).

149. General Properties of ZnO. in *Zinc Oxide* 1–76 (John Wiley & Sons, Ltd, 2009). doi:10.1002/9783527623945.ch1

150. Opoku, F., Govender, K., van Sittert, C. & Govender, P. Understanding the mechanism of enhanced charge separation and visible light photocatalytic activity of modified wurtzite ZnO with nanoclusters of ZnS and graphene oxide: From a hybrid density functional study. *New J. Chem.* **41**, (2017).

151. Paufler, P. Landolt-Börnstein. Numerical data and functional relationships in science and technology. New Series, Editor in Chief: K. H. Hellwege. Group III, Crystal and Solid State Physics, Vol. 7, Crystal Structure Data of Inorganic Compounds, W. Pies, A. Weiss, Part b, Key Elements O, S, Se, Te, b3: Key Elements S, Se, Te, Editors: K. H. Hellwege, A. M. Hellwege, Springer-Verlag Berlin 1982, XXVII, 435 Seiten. Leinen, Preis: DM 740, –. *Crystal Research and Technology* **18**, 1318–1318 (1983).

152. Dinges, R., Fröhlich, D., Staginnus, B. & Staude, W. Two-Photon Magnetoabsorption in ZnO. *Phys. Rev. Lett.* **25**, 922–924 (1970).

153. Oshikiri, M., Imanaka, Y., Aryasetiawan, F. & Kido, G. *Comparison of the electron effective mass of the n-type ZnO in the wurtzite structure measured by cyclotron resonance and calculated from first principle theory*. **298**, (2001).

154. Baer, W. S. Faraday Rotation in ZnO: Determination of the Electron Effective Mass. *Phys. Rev.* **154**, 785–789 (1967).

155. Ramesh, J., Pasupathi, G., Mariappan, R., Kumar, V. S. & Ponnuswamy, V. Structural and optical properties of Ni doped ZnO thin films using sol–gel dip coating technique. *Optik* **124**, 2023–2027 (2013).

156. RAJEH, S. *et al.* Structural, morphological, optical and opto-thermal properties of Ni-doped ZnO thin films using spray pyrolysis chemical technique. *Bulletin of Materials Science* **39**, 177–186 (2016).

157. Singh, S. & Rao, M. S. R. Optical and electrical resistivity studies of isovalent and aliovalent $3d$ transition metal ion doped ZnO. *Phys. Rev. B* **80**, 045210 (2009).

158. Katayama-Yoshida, H. & Sato, K. Materials design for semiconductor spintronics by ab initio electronic-structure calculation. *Physica B: Condensed Matter* **327**, 337–343 (2003).

159. Fan, W., Zhang, Q. & Wang, Y. Semiconductor-based nanocomposites for photocatalytic H2 production and CO2 conversion. *Phys. Chem. Chem. Phys.* **15**, 2632–2649 (2013).

160. Stevanović, V., Lany, S., Ginley, D. S., Tumas, W. & Zunger, A. Assessing capability of semiconductors to split water using ionization potentials and electron affinities only. *Phys. Chem. Chem. Phys.* **16**, 3706–3714 (2014).

161. Zhang, C. *et al.* Strain distributions and their influence on electronic structures of WSe2–MoS2 laterally strained heterojunctions. *Nature Nanotechnology* **13**, 152–158 (2018).

162. Arent, D. J., Deneffe, K., Van Hoof, C., De Boeck, J. & Borghs, G. Strain effects and band offsets in GaAs/InGaAs strained layered quantum structures. *Journal of Applied Physics* **66**, 1739–1747 (1989).

163. Ohta, H., Kamiya, M., Kamiya, T., Hirano, M. & Hosono, H. UV-detector based on pn-heterojunction diode composed of transparent oxide semiconductors, p-NiO/n-ZnO. *Thin Solid Films* **445**, 317–321 (2003).

9.Appendix

Strained NiO-Interface

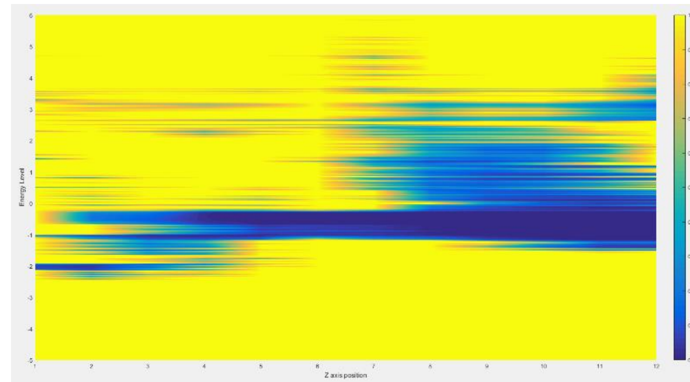

Figure 9-1 Spatial DOS structure of the $\langle 110 \rangle$ - $\langle 11\bar{2}0 \rangle$ interface. NiO structure to the left, ZnO structure to the right.

ZnO Conduction Band Interface States

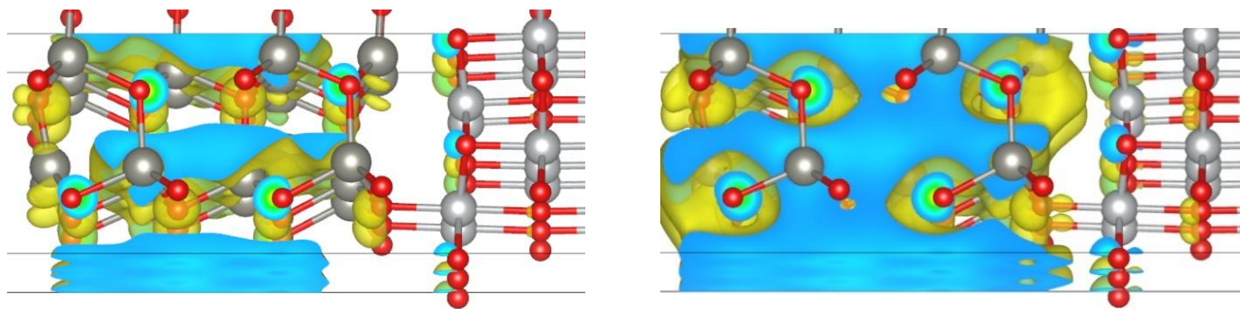

Figure 9-2 Conduction band charge density of the $\langle 100 \rangle$ - $\langle 10\bar{1}0 \rangle$ interface, calculated with hybrid functional utilizing standard fraction of exact exchange. The image to the left has isosurface level 0.001, while the image to the right has isosurface level 0.0004, demonstrating the extension of the conduction band orbitals towards the NiO structure. The energy level corresponds to the ZnO surface state level.

Hydrogenated Surfaces Comparison

The effect of hydrogenating oxygen termination surfaces on the structural and electronic properties has been investigated.

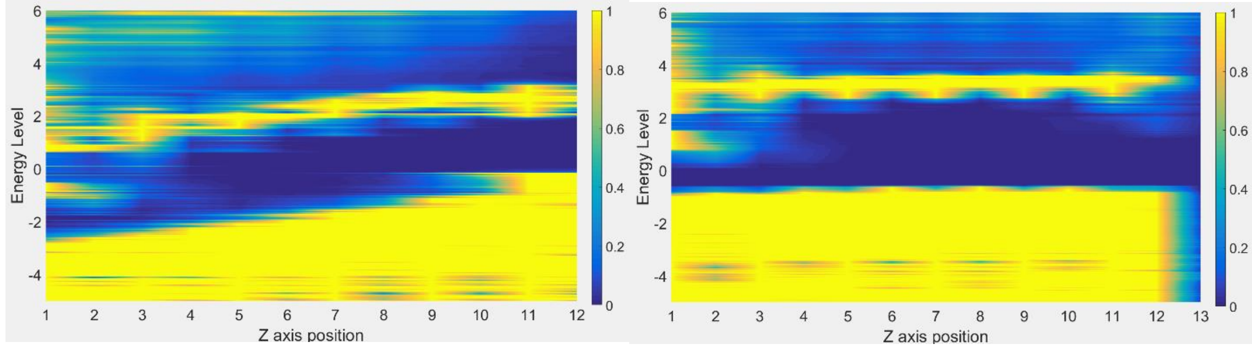

Figure 9-3 Left image: NiO-$\langle 111 \rangle$ Clean oxygen termination. Right image: NiO-$\langle 111 \rangle$ Hydrogenated oxygen termination.

As may be seen from figure Figure 9-3, the application of hydrogen to the NiO-$\langle 111 \rangle$ oxygen termination (right side of images) reduces the total dipole, by acting as a positively charged monolayer, and completely inhibits the formation of valence band states, by allowing the oxygen ions to retain the close-to bulk structure. The hydrogen layer forms conduction band states instead, however. The polar ZnO surface forms a lesser extent of valence band states, so hydrogenating the oxygen termination causes little effect.

Hydrogenating non-polar ZnO surfaces has greatly disruptive effects on the DOS structure:

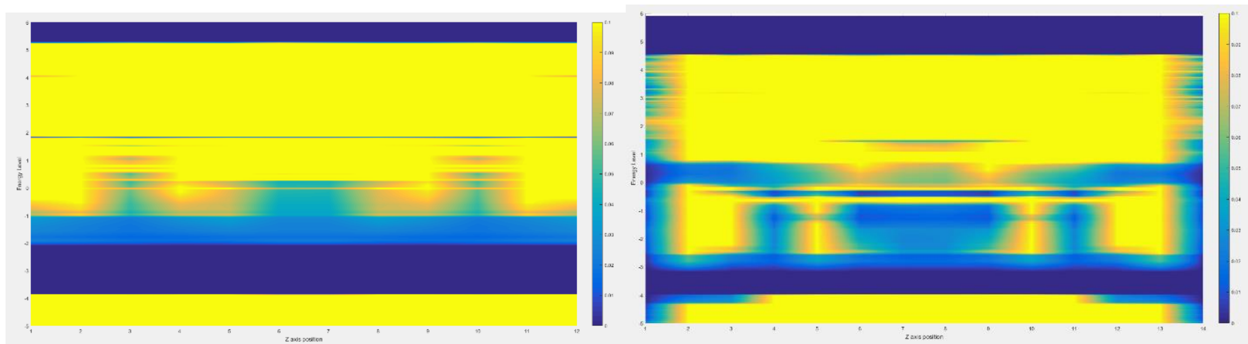

Figure 9-4 Left image: Zn$\langle 11\bar{2}0 \rangle$ Clean termination. Right image: ZnO-$\langle 11\bar{2}0 \rangle$ Hydrogenated termination.

In this case, the band gap is considerably reduced, and significant surface states occur. Similar effects occur for the $\langle 10\bar{1}0 \rangle$ surface. While the effect on the nonpolar NiO-$\langle 110 \rangle$ surface is to a lesser extent, hydrogen still acts disruptively to the electronic structure of all surfaces except NiO-$\langle 111 \rangle$, greatly increasing the energy shift and mid-gap states.